Advances in Gamma-Ray Imaging with Intensified Quantum-Imaging Detectors

ADVANCES IN GAMMA-RAY IMAGING WITH INTENSIFIED QUANTUM-IMAGING DETECTORS

by

Ling Han

A Dissertation Submitted to the Faculty of the

COLLEGE OF OPTICAL SCIENCES

In Partial Fulfillment of the Requirements

For the Degree of

DOCTOR OF PHILOSOPHY

In the Graduate College

THE UNIVERSITY OF ARIZONA

2017

THE UNIVERSITY OF ARIZONA
GRADUATE COLLEGE

As members of the Dissertation Committee, we certify that we have read the dissertation prepared by Ling Han, titled Advances in Gamma-Ray Imaging with Intensified Quantum-Imaging Detectors and recommend that it be accepted as fulfilling the dissertation requirement for the Degree of Doctor of Philosophy.

Date: (11/20/17)
Name: Lars Furenlid

Date: (11/20/17)
Name: Arthur Gmitro

Date: (11/20/17)
Name: Matthew Kupinski

Date: (11/20/17)
Name: H. Bradford Barber

Final approval and acceptance of this dissertation is contingent upon the candidate's submission of the final copies of the dissertation to the Graduate College.

I hereby certify that I have read this dissertation prepared under my direction and recommend that it be accepted as fulfilling the dissertation requirement.

Date: (11/27/17)
Dissertation Director: Lars Furenlid

STATEMENT BY AUTHOR

This dissertation has been submitted in partial fulfillment of the requirements for an advanced degree at the University of Arizona and is deposited in the University Library to be made available to borrowers under rules of the Library.

SIGNED: Ling Han

ACKNOWLEDGMENTS

First of all, I am indebted to my parents, Baoquan Han and Xiujie Xu, for their selfless efforts supporting my over twenty years' domestic and overseas education. I am grateful to them for their encouragements to pursue a PhD degree. I owe special thanks to my wife, Yajuan, and am grateful for her patience, accompany, help, and encouragement during my PhD study.

I am indebted to my advisor, Lars Furenlid, for his continual support and guidance during the course of this research. Many achievements in this research would not be possible without his brilliant ideas and advices. He is not only a respectable professor with a lot of experience and knowledge, but also a great person to be around with. I am also grateful to Harrison Barrett for his guidance and encouragement in learning about mathematical foundations of my work. I would like to thank Brad Barber for his help with many experiments, for tutoring me fundamental knowledge when I first joined the group, and for serving in my dissertation committee. I am indebted to Christy Barber for her help with so many small animal experiments. I would like to thank Zhonglin Liu and James Woolfenden for their help with interpreting animal images. I am also indebted to Luca Caucci for offering help with image reconstruction that is an important aspect of this work. I would like to thank Brian Miller for his assistance with troubleshooting software problems of FastSPECT III system. I also would like to thank Matthew Kupinski and Art Gmitro for serving in my dissertation committee and proving valuable feedbacks and guidance to this dissertation.

I would like to thank all of my colleagues at the Center for Gamma-Ray Imaging, Vaibhav Bora, Helen Fan, Esen Salcin, Joseph Ortiz, Cecile Chaix, Ryeojin Park, Yijun Ding, Xin Li, Maria Ruiz, Alex Lin, Neil Momsen, and Pier Ingram for sharing their ideas and being a tremendous support group, who are not only great co-workers, but are also great friends in life. Finally I would like to thank Merry Warner and Liz Hague for helping me purchase all kinds of lab supplies and equipment.

This work was supported by NIH/NIBIB grant P41-EB002035 "The Center for Gamma-Ray Imaging", and Department of Medical Imaging "TIPPS" grant, lymphoscintigraphy.

TABLE OF CONTENTS

LIST OF FIGURES

LIST OF TABLES

ABSTRACT

Nuclear medicine, an important branch of modern medical imaging, is an essential tool for both diagnosis and treatment of disease. As the fundamental element of nuclear medicine imaging, the gamma camera is able to detect gamma-ray photons emitted by radiotracers injected into a patient and form an image of the radiotracer distribution, reflecting biological functions of organs or tissues. Recently, an intensified CCD/CMOS-based quantum detector, called iQID, was developed in the Center for Gamma-Ray Imaging. Originally designed as a novel type of gamma camera, iQID demonstrated ultra-high spatial resolution (<100 micron) and many other advantages over traditional gamma cameras. This work focuses on advancing this conceptually-proven gamma-ray imaging technology to make it ready for both preclinical and clinical applications. To start with, a Monte Carlo simulation of the key light-intensification device, i.e. the image intensifier, was developed, which revealed the dominating factor(s) that limit energy resolution performance of the iQID cameras.

For preclinical imaging applications, a previously-developed iQID-based single-photon-emission computed-tomography (SPECT) system, called FastSPECT III, was fully advanced in terms of data acquisition software, system sensitivity and effective FOV by developing and adopting a new photon-counting algorithm, thicker columnar scintillation detectors, and system calibration method. Originally designed for mouse brain imaging, the system is now able to provide full-body mouse imaging with sub-350-micron spatial resolution.

To further advance the iQID technology to include clinical imaging applications, a novel large-area iQID gamma camera, called LA-iQID, was developed from concept to prototype. Sub-mm system resolution in an effective FOV of 188 mm × 188 mm has been achieved. The camera architecture, system components, design and integration, data acquisition, camera calibration, and performance evaluation are presented in this work. Mounted on a castered counter-weighted clinical cart, the camera also features portable and mobile capabilities for easy handling and on-site applications at remote locations where hospital facilities are not available.

CHAPTER 1

INTRODUCTION

In recent years, medical imaging has become more and more important as an effective way for screening and diagnosis of many kinds of disease and conditions. A key advantage of a majority of modern medical-imaging techniques is that the process is non-invasive, which means no instrument is introduced into the patient's body. As an important branch of medical imaging, nuclear medicine can assist with both diagnosis and treatment of disease. Nuclear imaging provides *in vivo* function-based imaging, which enables visualization and assessment of physiological processes by detecting regions of biological/biochemical activity associated with conditions such as unregulated metabolism, inflammation, rapid cell division, hypoxia, expression of cell surface receptors, etc. Scintigraphy, Single-Photon Emission Computed Tomography (SPECT) and Positron-Emission Tomography (PET) are three nuclear imaging techniques currently used in clinical and preclinical imaging applications. This chapter starts from the origin of radioactivity, provides an overview of radioactivity detectors, and from there introduces scintigraphy, SPECT and PET systems. Finally, the goals of this work are presented: advancing a high-resolution intensified quantum-imaging detector approach to gamma-ray imaging applications.

1.1 Radioactivity

The underlying principle of nuclear imaging is the detection of minute, trace, amounts of radioactivity. Strictly speaking, radioactivity, also known as radioactive decay, refers to the physical process through which an unstable atom emits radiation when losing energy, capturing electrons or going through internal conversion. The emitted radiation can be alpha particle, beta particle, electron or gamma-ray. Energetic fission fragments can also be made by some heavy isotopes, but are generally not useful for imaging or therapy.

The discovery of radioactivity can be traced to the discovery of high-energy photons, which was honored in the very first Nobel Prize in physics, awarded to Whilhelm Conrad Röntgen in 1901. Röntgen's discovery led to widespread experimentation among scientists and physicians, and he is today considered the "father" of diagnostic radiology.

In 1895, Röntgen was experimenting with different kinds of vacuum tubes by passing electrical discharge through them. One tube had a thin aluminum window to allow any effects of the electrical discharge to exit the tube. After the aluminum window was a protective cardboard piece that was opaque to light, meaning no light would pass through the cardboard. However, another cardboard painted with barium platinocyanide, when place close to the aluminum window, surprisingly showed a fluorescent effect. The same effect happened with another tube with a glass wall. After some other experiments that repeated the same results Röntgen speculated that a new kind of ray, which he names "X-rays", caused the fluorescent effect. X-rays are also known as "Röntgen rays" in many languages. When he was testing different materials to stop the rays, he saw the very first radiographic image of his own skeleton by putting his hand into the path of rays. About two weeks later, he took the very first picture of his wife's hand using X-rays as shown in Figure 1.1, which was also the first application of X-rays for medical imaging. Three papers were then published in 1895, 1896, and 1897 by Röntgen about his investigation of X-rays [Röntgen 1895, 1896, 1897].

Figure 1.1: The first x-ray image of the hand of Whilhelm Röntgen's wife.

It was Röntgen's discovery of X-rays that led to a widespread experimentation with high-energy photons across the world. And in 1896, just less than one year after Röntgen's discovery of X-rays, natural radioactivity was discovered by the French scientist Henri Becquerel. With the suspicion that the glow caused by X-rays might actually be related to phosphorescence, Becquerel performed some experiments by wrapping photographic plates with black paper and placing different phosphorescent salts on the outside. If his speculation

was correct, he expected to see the blackening of the photographic plate. However, none of the phosphorescence salts showed positive results. Surprisingly when he placed uranium salts that are not phosphorescent on the plate, he observed a blackening effect. These experiments proved that X-rays were not produced by the phosphorescent materials, and that uranium can also generate invisible rays that can cause blackening of photographic plates. Although it seemed the invisible rays produced by uranium were similar as X-rays, further research by Becquerel and other researchers, including his students Pierre Curie and Marie Curie, showed that the invisible rays were more complicated than X-rays. These invisible rays or radiations were given the name of "Becquerel Rays". Becquerel, Pierre and Marie Curie also shared the third Nobel Prize in Physics for the discovery of natural radioactivity in 1903.

Ernest Rutherford, a British physicist, started exploring the radioactivity of uranium after learning about Becquerel's experience. He discovered two types of radiations that have different penetration properties than X-rays, which he named "alpha ray" and "beta ray" in 1899. Alpha rays have the weakest penetration power, and were later renamed as alpha particles, which consists of two protons and two neutrons bound together. Beta rays have stronger penetration power, and were later reclassified as beta particles, which are high-energy electrons or positrons. Both particles are produced in the process of nucleus decay. Paul Ulrich Villard, a French chemist and physicist, discovered a third type of ray when he was investigating the radiation from radium salts. He used thin layer of lead to block alpha rays while two other kinds of rays still made it through. One of these two rays can be bent by a magnetic field and was recognized as beta rays and the other had never been identified at that time and could not be bent by a magnetic field. Because of their higher penetration power than alpha rays and beta rays, in 1903 Ernest Rutherford proposed calling the third type of rays "gamma rays".

1.2 X-Rays vs Gamma-Rays

Although alpha rays, beta rays and gamma rays were discovered in the same time period and even emerging from the same radioisotope, alpha rays and beta rays are in fact charged particles and they are easily separated from gamma-rays, which are actually electromagnetic waves. However, X-rays and gamma-rays are not distinguishable as they differ only in where they originate.

X-rays used for medical imaging applications are typically produced when accelerated electrons of sufficient energy collide with a metal target or anode. This often happens in a tube where high voltage is applied and the electrons are released by a hot cathode and accelerated by an applied electric field. The anode can be made from different materials. In imaging applications, the anode is usually made of tungsten but sometimes molybdenum is used for generating lower-energy X-rays. Two physical processes can occur when X-rays are generated. The first process is called characteristic X-ray emission. In this case, the accelerated electron has enough energy to knock one electron out of an inner shell of an anode atom. When the vacancy is filled by another electron in higher energy level, an X-ray photon is emitted. Since the X-ray photons emitted in this way have exactly the same energy and wavelength, distinct peaks will show up in the X-ray emission spectrum, called spectral lines of the anode material. The second process is called bremsstrahlung emission. In this case, the X-rays are emitted when the accelerated electrons are scattered and decelerated by the strong electric fields of the nuclei. Because the scattering angle can be in any direction and involve any energy loss, the emitted X-ray photons' energies are continuously varying, yielding a continuous spectrum. The largest energy of X-ray photons possible therefore depends on the kinetic energy of the accelerated bombarding electrons and thus the voltage setting (kVp) of the X-ray tube. Typically X-ray photon energies can vary between 100eV and 100keV corresponding to wavelength varying between 10nm and 0.01nm. X-rays with greater than 10keV energy or shorter than 0.1nm wavelength are often called hard X-rays, while those of longer wavelength are often called soft X-rays. Generally, the total X-ray emission spectrum consists of both the continuous bremsstrahlung energy distribution and the characteristic spectral lines as shown in Figure 1.2.

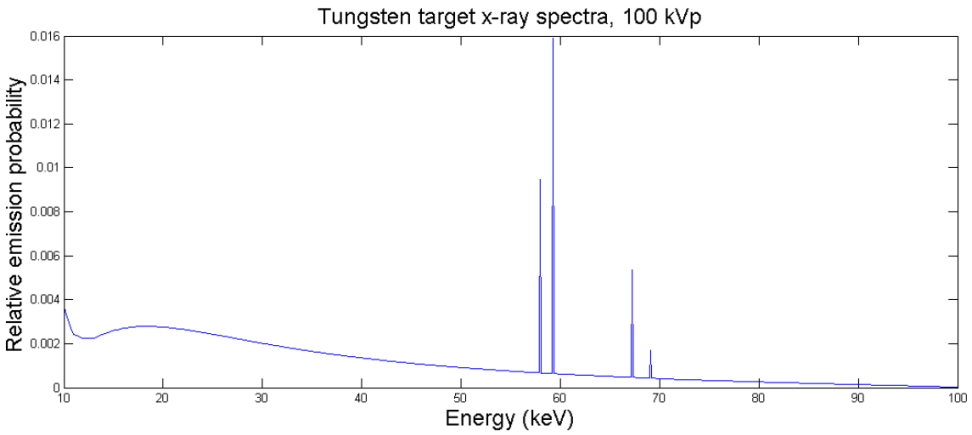

Figure 1.2 [Durko 2014]: Simulated X-ray spectrum by accelerating electrons across 100kV voltage and bombarding a tungsten target. Both characteristic spectral lines of the tungsten and the continuous bremsstrahlung energies are shown in the figure.

Unlike X-rays, gamma-rays are produced in a process involving the nucleus. For example, an excited or unstable nucleus may first go through alpha decay or beta decay by emitting an alpha or beta particle, leaving the remaining nucleus still in an excited state. When the excited daughter nucleus decays to a lower energy state through so-called gamma decay, a gamma-ray photon is emitted. Another source of gamma-rays is the annihilation of a positron and an electron. Positrons are produced in beta plus decay of a nucleus. Normally beta decay refers to beta minus decay when a neutron converts into a proton by emitting an electron. Beta plus decay refers to the process when a proton convers into a neutron by emitting a positron. When a positron, the anti-matter equivalent of the electron, combines with an electron, they annihilate each other and release two antiparallel gamma-ray photons, each with energy of 511 keV (or in a rare process, release three or more gamma rays). This source of gamma-rays is used in positron-emission-tomography (PET) systems that will be introduced later.

Half-life is a term describing how fast radioisotopes undergo radioactive decay. The definition of half-life is the time required for the amount of radioactivity in a sample to decay to half of its initial value. The energies of gamma rays typically vary between tens of keVs to well above 1 MeV.

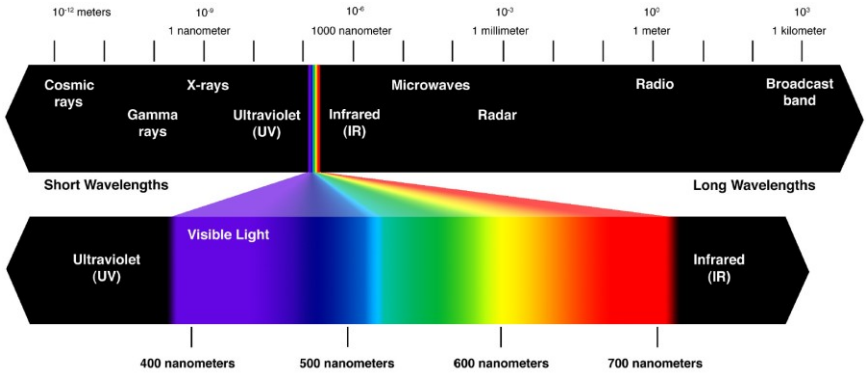

Figure 1.3 [Widen 2008]: The electromagnetic spectrum with gamma-rays and X-rays on the shorter wavelength end. Large energy overlap can be seen for gamma-rays and X-rays.

As shown in Figure 1.3, X-rays and gamma-rays have largely overlapping energy ranges and both are electromagnetic waves, making them indistinguishable by detectors. However, due to their method of generation, X-rays are more commonly used in transmission tomography such as the well-known computed tomography (CT) systems, as well as planar scanning systems like the radiography and fluoroscopy systems in hospitals and cargo inspection systems in airports. In these systems, X-rays partially penetrate through the targets and generate image contrast based on the spatial attenuation distributions. Gamma-rays are typically used in scintigraphy, SPECT and PET systems. Instead of placing the source away from the target and shining its rays upon the target, gamma-ray sources in the form of radiolabeled carrier molecules are introduced into the target and allowed to concentrate in the region of interest. This technology is the so called radiotracer technique.

1.3 Radiotracer Technique

The discovery of the radiotracer technique traced back to early 1900s. A Hungarian chemist named George Charles de Hevesy joined Ernest Rutherford's group and started a task to isolate radium D from a large amount of lead. However, after two years of work, de Hevesy found there was no way to distinguish or separate the radium D from the lead chemically. He changed his way of thinking and decided to use radium D as surrogate for lead. [Hevesy 1962] Later on, in a study of metabolic processes of plants and animals, de Hevesy replaced a portion of stable isotopes with radioactive isotopes, which allowed him to trace the distribution of the chemicals in plant and animal bodies. The first paper was published in

1923 regarding the use of natural radiotracer ^{212}Pb to study the absorption and translocation of metals in roots, stems and leaves. [Hevesy 1923, Myers 1979] In 1943, George de Hevesy was awarded the Nobel Prize in Chemistry for his work on the use of isotopes as tracers in the study of chemical processes.

Technically, a radiotracer, also called a radioactive tracer or radioactive label, is a chemical compound where one or more atoms have been replaced by unstable isotopes or radioisotopes, so that chemical reactions can be traced by detecting the radioactive decay of the radioisotope. There are many important applications of the radiotracer technique. Beyond tracing chemical reactions, the distribution of substances in tissues and the flow of certain fluids can be tracked after a radioactive compound is introduced into the tissue or fluid. Radioactive tracers are also the starting point of modern nuclear-imaging technologies such as PET scans, SPECT scans, and all kinds of scintigraphy scans. They provide a non-invasive way to measure the distribution of radiolabeled compounds in the body.

With the development of modern isotope-production and chemical-synthesis technologies, many different kinds of radiotracers can be produced to target a specific region or process in the body. For example, technetium-99m, with the symbol of ^{99m}Tc, is a radioisotope of technetium and is widely used in medical diagnostic procedures. ^{99m}Tc emits gamma-rays with a main photon energy of 140keV about 88% of the time and decays to ^{99}Tc. The half-life of ^{99m}Tc is about 6 hours, which allows enough time for a medical study while keeping total radiation dose to the patient low. An example is ^{99m}Tc-labeled methylene diphosphonate, also called MDP, a pharmaceutical product widely used in bone scans. Because the uptake of MDP mainly occurs at cites of the bone reformation, it is used to locate bone metastases of multiple cancer types. [Subramanian et al. 1975]

The ability to target specific cells or processes with radiotracers or radiopharmaceuticals makes nuclear imaging a functional imaging technology, meaning that its utility is in detecting or measuring changes in metabolism, blood flow, absorption and so on. In comparison, X-ray imaging techniques like the CT scan or non-radiation methods like magnetic resonance imaging (MRI) are for structural imaging, meaning that they mainly provide anatomical information about the body.

1.3.1 Common Radioisotopes and Ligands

Although natural radionuclides exist, most radionuclides used in nuclear imaging applications are synthesized deliberately. There are three typical ways to synthesize radionuclides. Nuclear reactors can generate radioisotopes from fission products or neutron bombardment of suitable targets. Particle accelerators such as cyclotrons can produce radionuclides by bombarding accelerated charged particles onto a target. Radionuclide generators generate radioisotopes through the decay of a longer half-life parent radionuclide. For example, the most commonly used ^{99m}Tc is the decay product of molybdenum-99 (^{99}Mo) produced in nuclear reactors. Table 1.1 lists the most commonly used radioisotopes in nuclear imaging with their half-life.

Nuclear Medicine	Radioisotope	Peak Energies (keV)	Half life
Scintigraphy SPECT	^{99m}Tc	142.68 (89%)	6.01 hours
	^{111}In	172.28 (90.7%) 245.35 (94.1%)	2.80 days
	^{123}I	158.97 (83.3%)	13.22 hours
	^{125}I	27.202 (39.6%) 27.472 (73.1%)	59.4 days
PET	^{18}F	511 × 2	109.8 minutes
	^{11}C		20.33 minutes
	^{13}N		9.97 minutes
	^{15}O		122.24 seconds

Table 1.1: Common radioisotopes used in nuclear medicine imaging with their peak energies and half-life.

Besides radioisotopes, properly selected ligands are the key biochemical substances that carry the radioisotopes to the tissue of interest. The affinity of the radiolabeled ligands or radioligands to the target tissue relative to non-specific background uptake determines the image quality that can be measured in the tissue of interest. So it's preferred to choose radioligands that can be transported to the tissue, have high affinity for the tissue, but clear from the rest of the body quickly. [Alford et al. 2009, Müller and Schibli 2013]

1.4 Nuclear-Medicine Imaging

While the radiotracer technique dates back nearly 100 years, nuclear medicine imaging, also called nuclear medicine though that technically also includes therapeutic use of radioisotopes, developed over the last half-century as detector and electronics technology advanced. As a major branch of modern medical imaging, nuclear medicine has been widely used for early detection, treatment and screening of many medical conditions. Some examples include brain tumors, breast cancer, heart disease, loss of kidney function, thyroid cancer, lymphoma, etc. Nuclear medicine demonstrates many advantages over other types of imaging techniques for certain applications. By introducing radioisotope-labeled pharmaceuticals or radiotracers into the body through intravenous injection, inhalation or ingestion, no instruments need to be inside the body for imaging purposes, making nuclear medicine imaging a non-invasive imaging tool. The radiation dose is typically lower than that of conventional X-ray imaging. There are also very rare side effects during nuclear imaging. Because the radiotracer distribution varies with the functionality of an organ, nuclear medicine can often diagnose certain conditions much earlier than other types of imaging techniques. As an example, methylene-diphosphonate (MDP) is a pharmaceutical primarily taken up by regenerating bone matrix. By attaching technetium-99m radioisotope to MDP and delivering to human body, all bone will absorb some radiotracer and show up in the image. If there is a fracture or other insult to the bone, the physiological function at the insult location will be increased, absorbing more radiotracer and resulting in a “hot spot” in the image.

Unlike diagnostic X-ray or CT scans, where the X-ray source is produced outside of the body and X-rays are passing though the body to form an image of attenuation as indication of anatomical structure, nuclear medicine generally employs external detectors or cameras, often called gamma cameras, to capture the gamma rays emitted by the radiopharmaceuticals attached to specific organs inside the body, and relate the image to the radiotracer distribution. So an image from a gamma camera is representing or can be related to the physiological function of organs instead of the anatomical structure of the body. As shown in Figure 1.4, a PET scan, a nuclear-medicine technique, of the same body shows a substantially different image than a CT scan.

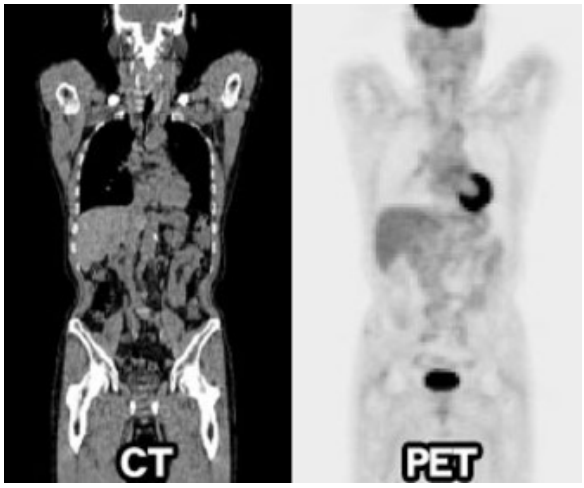

Figure 1.4: Comparison of CT and PET scans of the same patient body. Notice the different image contents and contrasts between a CT scan and a nuclear medicine scan.

There are three major techniques in nuclear medicine imaging, namely, scintigraphy, single-photon-emission computed-tomography (SPECT) and positron-emission tomography (PET). Although each of them has its own principles, features, advantages and disadvantages, the key fundamental element of all three is the gamma camera (scintigraphy & SPECT) or closely related block detector (PET).

1.4.1 Gamma Camera

A gamma camera is a device used to form an image of radioisotopes distributions. The most commonly used gamma camera was invented by Hal Anger in 1952, which is called Anger camera or Anger scintillation camera and is also the basis of modern gamma cameras. [Anger 1952, Anger 1958, Anger 1964] Figure 1.5 shows a schematic view of the cross section of an Anger camera outfitted with a pinhole collimator.

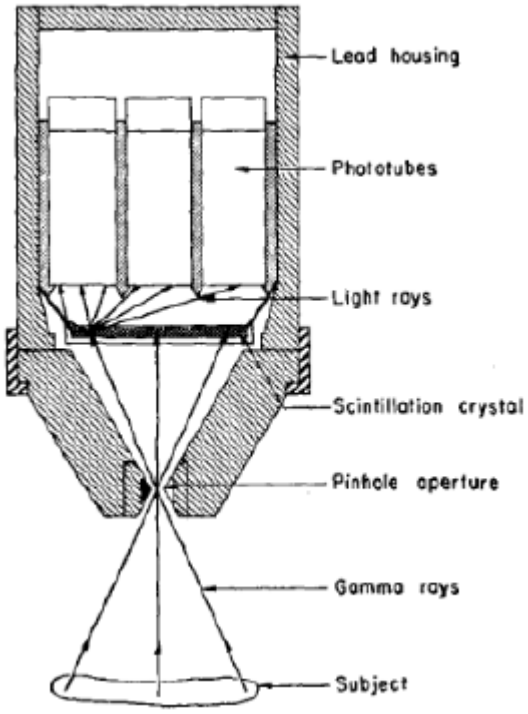

Figure 1.5 [Anger 1958]: A schematic view demonstrating the configuration and imaging principle of an Anger camera.

Basically four components are required for a gamma camera to form an image of the radiotracers. The first component is the gamma-ray image-formation optics, which creates correspondence between points in the object and points in the image. The pinhole aperture and the parallel-hole collimator are two typical elements used for gamma-ray image formation. Pinhole apertures form an inverted image of the object with different magnifications along the depth of the object, whereas parallel-hole collimators form erect images with 1:1 magnification. Figure 1.6 shows both a pinhole aperture and a parallel-hole collimator for gamma-ray imaging. The second component after the gamma-ray optics is the gamma-ray detector, which detects each gamma-ray photon by physical interaction and transfers its energy into other forms of energy that can be conveniently transported and recorded. Scintillation detectors and semiconductor detectors are two major types of gamma-ray detectors developed and used in gamma cameras. Gamma-ray photons interact with scintillation detector materials and transfer their energy into visible light, whereas the interaction in semiconductor detector generates electron-hole pairs that form current under

an applied bias voltage. The third component in a gamma camera is the readout system, which processes the raw signals from gamma-ray detectors, either scintillation light or current, and transfers them into digital electrical signals. Section 1.7 presents a survey of most commonly used scintillation detectors and semiconductor detectors, along with different readout systems. The final component in the gamma-ray imaging chain is signal processing and estimation. This is currently realized in a computer by applying algorithms to the digital signals produced by the readout system. For example, maximum-likelihood (ML) estimation has been frequently used in gamma-ray imaging to estimate interaction position, energy, and other parameters of detected gamma-ray photons. [Barrett et al. 2009] More insights about scintillation-gamma-camera physics will be presented in chapter 2.

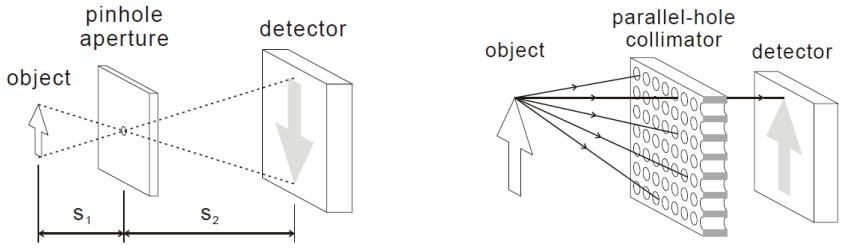

Figure 1.6 [Chen 2006]: The imaging principle of a pinhole aperture (left) and a parallel-hole collimator (right)

1.4.2 Scintigraphy

Scintigraphy refers to the nuclear-medicine imaging technique that detects gamma-rays emitted by the radiotracers with a gamma camera and forms a two-dimensional image. It's the most straightforward application of gamma cameras. Since it's a 2D planar imaging technique, very little depth information can be acquired in scintigraphy. However, when depth information is not very important, scintigraphy can be very convenient and easy to interpret. Because only one gamma camera is required, the system is usually portable and can be applied to many different organs or locations of the body, such as lung scintigraphy, mammoscintigraphy, bone scintigraphy, and lymphoscintigraphy. Dedicated gamma cameras designed specifically for certain type of scintigraphy can have optimal performance compared to other general-purpose gamma cameras. [Weinmann et al. 2009]

As a planar imaging technique, scintigraphy is the direct application of gamma cameras with minimal post-processing. Other techniques exist that are based on both gamma cameras

and complicated post-processing techniques such as limited angle tomography or tomosynthesis. True 3D information of radiotracer distribution is provided by SPECT and PET.

1.4.3 SPECT

SPECT stands for single-photon-emission computed tomography and is a tomographic imaging technique based on radiopharmaceuticals emitting gamma rays one at a time. A SPECT system consists of one or multiple gamma cameras similar to the ones used in scintigraphy applications. When the radiotracers or radiopharmaceuticals are produced and introduced to the body, they emit gamma-rays into all directions during their decay processes. A SPECT imaging system then rotates the gamma cameras around a human body and captures 2D projection images of radiotracer distribution from many different orientations with the equipped gamma cameras. After acquisition of the data, a tomographic reconstruction algorithm is then applied to the set of acquired projection images, generating a 3D-tomographic estimate of the radiotracer distribution in the body. Finally the tomographic image will be displayed and analyzed. [Wernick and Aarsvold 2004] Figure 1.7 shows a schematic diagram of a SPECT system with three parallel-hole-collimator-equipped gamma cameras.

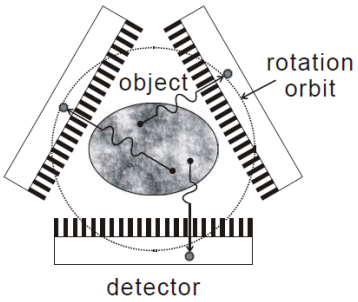

Figure 1.7 [Chen 2006]: Schematic diagram of SPECT system with three gamma cameras detecting single photons emitted from the radiotracers.

Because SPECT is based on the same gamma-camera architecture used in scintigraphy applications, both techniques may share the same types of radiotracers, which, as mentioned above, emit a single gamma-ray photon during each gamma decay. This is also the reason for the name of “single-photon-emission” computed tomography. For SPECT imaging, projection images from a range of angles of view are required to reconstruct the 3D

distribution of radiotracer. In clinical applications, usually there are two or three gamma cameras rotating around the body with 3-6 degrees step. For optimal reconstruction results, 360-degrees of acquisition are virtually always used. The more gamma cameras, the faster the scan will be. Another alternative configuration that has emerged recently in preclinical applications is to use multiple fixed gamma cameras arrayed in angle increments to acquire multiple projection images simultaneously. This type of SPECT system is called stationary SPECT or FastSPECT [Kastis et al. 1998, Furenlid et al. 2004, Miller et al. 2010]. Since no rotation of the gamma cameras is required, acquisition time can be very fast depending on the sensitivity of the system and the dynamics of the radiotracer activity in the object. Also no error will be caused by imprecise movement of the gamma cameras. Because of the dynamic nature of nuclear medicine imaging including the natural decay of radioisotopes and change of biological distribution of the radiotracers, simultaneous acquisition in stationary SPECT guarantees the same radiotracer distribution for all of the projection images, which reduces reconstruction error and provides most accurate and quantitative data. Another type of SPECT system recently emerging is adaptive SPECT, which can vary different configurations, pinhole diameters and distances for example, to adapt the system to different applications, providing the optimal performance [Chaix2015]. Section 1.7 presents a survey of state-of-the-art SPECT systems with relevant configurations and performances metrics.

Besides the projection images acquired from the gamma cameras in different orientations, information about the system imaging matrix is required before a 3D image of the radiotracer distribution can be reconstructed. System calibration is the process of characterizing the system response for all points in the field of view (FOV) across all orientations of image acquisition. Typically, a small point source made from radioisotopes is scanned across the 3D space of the FOV and projection data is acquired for each position of the point source. [Chen et al. 2005] In most rotational SPECT systems, only rotation parameters are measured. Other calibration data in the system matrix is modeled. In stationary SPECT system, calibration data for all necessary directions can be simultaneously acquired from all of the gamma cameras, which incurs no estimation error. All of the data

acquired in the system-calibration process will be arranged in a matrix format for future image reconstructions, called the imaging or system matrix.

With an imaging matrix describing the system response and projection data of the object, a 3D image can be reconstructed via a tomographic reconstruction algorithm. Reconstruction methods were developed nearly two decades after the invention of Anger camera, however, most of them suffered from limitations in computational hardware. [Budinger and Gullberg 1974] Shepp and Vardi [1982] introduced the maximum-likelihood expectation maximization (MLEM) reconstruction method in 1982; that is an iterative reconstruction technique based on photon-counting statistics. With the ability to incorporate accurate system models, MLEM is widely used in emission tomography reconstruction. With the development of parallel-processing architectures such as graphical processing units (GPUs), MLEM can be very fast to compute. [Miller et al. 2012c]

1.4.4 PET

PET is the abbreviation for positron-emission tomography. PET is another type of tomographic imaging system based on radiotracer techniques. However, the system configuration and imaging principle of PET are different from SPECT.

First, the radiotracers used in PET imaging do not usually produce gamma-rays upon decay. Instead, a positron (β^+) is produced that travels a short distance and then annihilates with an electron in surrounding matter. Upon annihilation, two 511-keV gamma-ray photons traveling in almost exactly opposite directions are generated as shown in Figure 1.8 (upon rare occasion, three or more photons may be produced). So the two gamma-ray photons are indirectly generated by the radioisotope's decay. Because positron-emission radioisotopes generally have short half-lives, a nearby facility that generates these radioisotopes is required, causing a higher cost of the radiotracers. Also, because the location of annihilation is different than the location of the radiotracer decay, caused by the non-zero range of the positron's travel, the spatial resolution of PET system has some physical limitations.

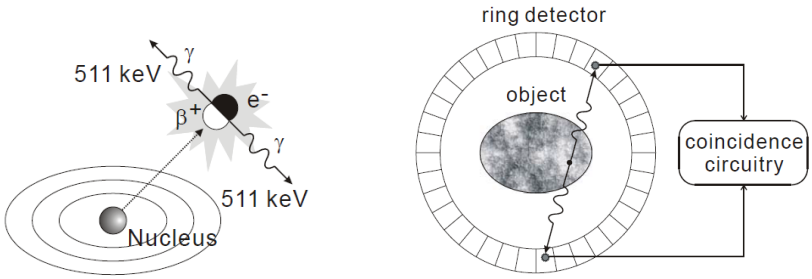

Figure 1.8 [Chen 2006]: Left: Demonstration of positron emission and its annihilation with an electron; Right: Schematic diagram of a PET system.

Unlike SPECT systems or gamma cameras, PET doesn't depend on pinhole or parallel-hole collimators for creating correspondences between points in the object and points in the image. Instead, PET takes advantage of the antiparallel characteristics of the two emitted gamma-ray photons and depends on coincidence detection (ACD) to determine the line position of the radioisotope. Figure 1.8 shows a typical geometry of a PET system, where small detectors are arranged in a ring. By detecting both gamma-ray photons with two detectors during a preset short time interval, the line of response along which the annihilation occurred can be determined. The total number of events collected by a pair of detectors thus corresponds to a line integral of the 3D radiotracer distribution similar to what pinholes and parallel-hole collimators provide.

Because no pinhole or parallel-hole collimator are required in PET system, many more gamma-ray photons compared to SPECT system will make their way to the detectors, thus requiring the detectors to have ultra-fast response or ultra-high timing resolution to separate incoming photons in the temporal domain. A large number of high-timing-resolution detectors increase the cost of PET systems relative to SPECT systems. However, because of the high gamma-ray energy which gives large detector signals, and the high collection efficiency, both resolution and system sensitivity are typically better than SPECT systems.

The major focus of this work is on gamma cameras and SPECT systems.

1.5 Performance Metrics

When a nuclear imaging system, either a gamma camera or SPECT system, is developed, a number of conventional metrics are used to evaluate the performances and characterize the imaging system, including spatial resolution, detection area or FOV, energy resolution, count-rate capability and sensitivity. Recently pioneered by the Center for Gamma-Ray Imaging, task-based evaluation should be used to estimate the performances of an imaging system. Signal-detection theory is a well-established rigorous method for measuring imaging system performances where an observer is typically employed for assessing the detectability of a signal in a background. [Sain and Barrett 2003] This section only focuses on the conventional performance metrics, however, it's recommended to read chapter 16 of the book by Barrett and Myers [2004] for an explanation of task-based performance evaluation.

Spatial resolution is a measure of the ability to resolve small objects in the FOV. The overall system spatial resolution of a gamma camera is typically assessed by the full width at half maximum (FWHM) of the image profile of a point-like or line-like radiation source with smaller FWHM value indicating better spatial resolution. The system spatial resolution is mainly affected by both the collimation resolution of the gamma-ray optics and the intrinsic resolution of the detection system. Collimation resolution arises from different designs of the gamma-ray optics such as pinhole and parallel-hole collimators, and in general constitutes the major part of the system resolution. Detector intrinsic resolution is contributed by gamma-ray detector and associated readout electronics. Statistical variations in scintillation photons production after gamma-ray interaction with the detector or photoelectrons emission by the photocathode of PMTs or image intensifiers all affect the intrinsic resolution. Spatial resolution directly affects lesion detection and various estimation tasks. It has also been shown that small improvements in spatial resolution contribute to large improvements in lesion detection and estimation tasks and improved resolution also reduces the number of necessary detected photons to produce visually similar images. [Muehllehner 1985, Rolland 1990, Rolland and Barrett 1992, Müller et al. 1986]

Detection area or FOV is another key parameter of an imaging system. When equipped with a parallel-hole collimator, the FOV is just the physical area of the detector. When pinhole apertures are used, the physical area of the detector divided by the magnification of

the pinhole aperture defines the FOV. FOV determines how large an object can be imaged by a gamma camera or a SPECT system without axial scanning. For example, 20mm spherical FOV may be enough for rodent brain imaging whereas a 200mmx200mm FOV is typically required for dedicated mammoscintigraphy. Another more important parameter affected by both detection area and spatial resolution is the space-bandwidth (Sp-BW) product, which determines the effective number of resolvable elements and is defined as the area of detector divided by the area of the effective PSF. [Barrett and Hunter 2005, Kupinski 2005] Large-Sp-BW detectors can provide improved overall efficiency than small-Sp-BW detectors. In SPECT imaging, the same image resolution can be achieved using minifying pinholes and small-area high-Sp-BW detectors as can be achieved using magnifying pinholes and large-area low-Sp-BW detectors. [Rogulski et at. 1993] However, since more small-area detectors and minifying pinholes can be placed around the object, higher system efficiency can be achieved.

Energy resolution is a measure of the ability of a detector to accurately determine the energy of incoming radiation and is typically expressed as a percentage of the incoming photon energy as (FWHM / photo energy peak) × 100, where the FWHM and photo peak are measured from the detected spectrum of incoming radiation. This ability is affected by both the detector material and the readout system of a gamma camera. The importance of energy resolution performance lies in two applications. The first application is to separate two radioisotopes and provide two separate images for each radioisotope distribution, so that two radiotracers targeting different processes can be used at the same time. The second application is to discriminate against scattered gamma-rays that are usually assumed to carry little spatial information and tend to degrade image quality. (The physics of Compton scattering is presented in chapter 2)

The count-rate capability is the ability of a detector to separately record incoming photons with certain count rate. When the count rate of incoming photons exceeds the count-rate capability of a detector, pileup occurs, resulting in degradation of spatial resolution, energy resolution, sensitivity, and linear response to activity. To provide higher count-rate capability, more gamma cameras with smaller pinholes can be used, as in a stationary SPECT system. Also photon-counting detectors are preferred compared with integrating

detectors. One advantage of using photon-counting detectors is that all detected rays including primary gamma-rays, and Compton scattered rays are analyzed individually, so the resulting image follows Poisson statistics. [ch.11 in Barrett and Myers, 2004] However, it's not impossible to use an integrating detector to identify individual gamma-ray photons if they are read out sufficiently fast. Furenlid et al. [2004] determined the maximum allowable count rate based on statistical analysis for using integrating detectors as a function of frame rate, detector PSF, and the degree of permitted overlap or multiplexing.

Finally, sensitivity is one of the most important performance metrics of a gamma camera or SPECT system. It's defined as the ratio between counted photons and the total number of photons emitted by the radiotracers. For a single gamma camera, sensitivity is mainly affected by the gamma-ray optics and gamma-ray detector thickness, but can also be affected by the energy window or threshold applied in the readout system and signal-estimation process. For example, a scintillation gamma camera with pinhole aperture typically has $<10^{-4}$ sensitivity level. For a SPECT system, the number of pinholes is a very important factor affecting the system sensitivity. Another definition usually used for sensitivity is based on the unit of cps/MBq, which is the counts per second recorded by the detectors per mega Becquerel of radioisotope activity in the object. The sensitivity of a system or gamma camera directly affects the data acquisition time, and may further affect the dosage required to be administered in the body. Because the dosage and acquisition time are usually physically limited based on specific tasks, enough sensitivity is the primary requirement to acquire a useful image. Figure of merit for a gamma-ray imaging detector that combines spatial resolution and sensitivity is the space-bandwidth-efficiency product that is defined as FOM = Sp-BW × Efficiency. [Barrett and Hunter 2005]

In SPECT system design, spatial resolution, FOV and sensitivity are often inversely related. The improvement of two metrics usually causes the degradation of the remaining one. So a proper balance or tradeoff between these three metrics needs to be determined for a particular task. Table 1.2 lists the variations of the three metrics when some system configurations or designs of a pinhole SPECT system have changed to demonstrate the tradeoff relationships.

Configuration change	Resolution (FWHM)	Sensitivity	Field of view
Object to pinhole distance ↑	↓	↓	↑
Pinhole diameter ↑	↑	↑	–
Detector to pinhole distance ↑	↑	–	↓

Table 1.2: Demonstration of design tradeoff of a pinhole SPECT system. (Here an increase in resolution means poorer resolution)

1.6 Preclinical vs. Clinical Imaging

Nuclear-medicine imaging techniques can be used for both clinical and preclinical applications, with importance in both fields. The importance of nuclear medicine in clinical applications has been presented in section 1.4. Here we discuss the importance of nuclear medicine in preclinical or small-animal imaging applications.

Small animals are widely used in biomedical research. With the capability to provide models of human disease, mice are ideal subjects and frequently used in fundamental studies of human conditions. Nuclear-medicine imaging can play a key role in these studies. It can not only trace the flow of new drugs to see whether they are delivered to the right organ or tissue, but also quantify the biodistribution of new diagnostic compounds to assess their utility. Over the years, nuclear-medicine imaging techniques have been successfully transferred to preclinical imaging systems and applied to many preclinical imaging applications, including cardiovascular imaging [Constantinesco et al. 2005, Golestani et al. 2010, Liu et al. 2007, Khaw et al. 1997], oncology [Gambini et al. 2011, Deutscher et al. 2009], gene expression [Zinn et al. 2002, Auricchio et al. 2003], etc.

Although both preclinical imaging systems and clinical imaging systems are based on the same imaging principles, they have many different detector requirements and characteristics for their specific applications. Here we present the different detector requirements for preclinical and clinical SPECT systems, which also apply to preclinical and clinical scintigraphy detectors.

The most obvious differences between clinical and preclinical detectors are the FOV and spatial resolution. Because the human body has much larger physical dimension than small animals like mice, the required FOV for clinical SPECT is much larger than for preclinical SPECT. Thus the 1D-linear spatial resolution of a preclinical SPECT image needs to be

much higher than a clinical SPECT image to perform the same tasks. Also because of the different dimensions, gamma-ray photons undergo more Compton scattering in the human body, creating more partial-energy events that demand high-energy-resolution detectors in clinical systems, whereas the path length through the tissue is short enough in a mouse that Compton scattering rarely happens. This weakens the requirement of high energy-resolution for preclinical systems. Other differences between preclinical and clinical nuclear imaging involve different radioisotopes and dosages. For human applications, in order to reduce the damage caused by radiation and increase the penetration capability, radioisotopes with a few hours half-life and >100 keV gamma-ray emissions are preferred, such as ^{99m}Tc (6-hour half-life and 140keV energy photon), whereas for small-animal imaging, longer half-life and lower-energy-emission radioisotopes can be used, such as ^{125}I(60-day half-life and ~30keV energy photon), which enables the use of additional biologically important ligands and longer study periods. Finally, because of the requirements to correct for scattering, attenuation and other effects, clinical systems usually lose quantization accuracy and are not easily employed in quantitative studies, while quantitative biodistribution studies are routinely performed with preclinical systems.

1.7 Brief Survey of Gamma Detectors and SPECT Systems

In this section, a brief survey of existing gamma-ray detectors and SPECT systems will be presented. As introduced above, gamma-ray cameras are mainly based on scintillation detectors or semiconductor detectors. Although many different scintillation materials can be used in gamma-ray detection, NaI(Tl) and CsI(Tl) are the two most commonly used scintillation materials. Variants of scintillation detector designs include continuous-scintillator-crystal [Anger 1958, Milster et al. 1984, 1990] , array-of-small-crystal [Truman et al. 1994, Weisenberger et al. 1998, 2001], micro-columnar-crystal [Nagarkar et al. 1998, Tornai et al. 2001], annular-crystal [Genna and Smith 1988], and concave-crystal [Korevaar et al. 2009]. Readout systems for scintillation gamma detectors include different configurations of photomultiplier tubes (PMT, PS-PMT, MA-PMT) [Kapusta et al. 2007, Kume et al. 1986, Kyushima et al. 2000], photodiode (and SDD) [Choong et al. 2002, Fiorini et al. 2000], avalanche photodiodes (APD and PSAPD) [Shah et al. 2001, 2002],

charge-coupled devices (CCD/CMOS, EMCCD) [Jerram et al. 2001] and silicon photomultiplier (SiPM) [Herbert et al. 2006]. The most common semiconductor materials for gamma-ray imaging include CdTe or CdZnTe (CZT) [Kim et al. 2006], Silicon (Si) [Peterson et al. 2003], High-purity Germanium (HPGe) [Luke et al. 2000], and Mercuric iodide (HgI_2) [Levi et al. 1982]. Because a large number of electronics channels are required for signal readout of semiconductor detectors, application-specific integrated circuits (ASIC) are generally used. Advanced scintillation cameras may also use ASIC-based readouts because of the use of semiconductor-based photodetectors. There are three basic ASIC architectures; gated integrators [Marks et al. 1996], self-trigging [Pettersen et al. 2005], and binary counters [Llopart et al. 2002]. Comprehensive reviews with more details about scintillation and semiconductor detectors and readout systems can be found in [Barrett and Hunter 2005] and [Peterson and Furenlid 2011]. This work is conducted on the basis of a novel gamma camera, i.e. iQID camera, which utilizes micro-columnar scintillator as the gamma-ray detector and intensified CCD/CMOS as the readout system.

To present a general summary of the state of art in SPECT technologies in the literature, a list is compiled in Table 1.3 for preclinical SPECT systems developed over the last two decades. Major configuration choices with gamma-ray optics and detectors are presented, along with performance metrics of spatial resolution, sensitivity and FOV. Many of the systems are stationary SPECT, which can provide much higher system sensitivity than rotational SPECT and are feasible in preclinical applications because smaller area detectors can be used. One of the systems is adaptive SPECT, which can vary pinhole diameters, the number of pinholes, object-to-pinhole distance and pinhole-to-detector distance. Adaptive SPECT systems offer versatility for different applications, providing choices of tradeoffs between resolution, sensitivity and FOV. Part of this work is to advance the FastSPECT III system shown in the list. At the time of this dissertation, the sensitivity of FastSPECT III has been greatly improved to ~50cps/MBq with the same 15mm FOV and ~350mm linear spatial resolution.

References	System Configuration	Resolution (mm)	Sensitivity (cps/MBq)	FOV (mm)
Kastis et al. 1998	FastSPECT I 24 1.5mm pinholes 24 ModCams (NaI(Tl)+PMT)	2.0	359	20
Furenlid et al. 2004	FastSPECT II 16 1.0mm pinholes 16 ModCams (NaI(Tl)+PMT)	2.2	243	40
Miller et al. 2010	FastSPECT III 20 0.25mm pinholes 20 iQIDs (Columnar CsI(Tl)+CCD)	0.33	16	15
Kim et al. 2006	SemiSPECT 8 0.5mm pinholes 8 CZT detectors	1.45	50	32
Mediso	NanoSPECT/CT 9 or 11 0.6-2.5mm pinholes 1, 2 or 4 detectors (NaI(Tl)+PSPMTs)	0.4-2	-	22-62
Chaix 2015	AdaptiSPECT 1-5 0.6-1.4mm pinholes 16 ModCams (NaI(Tl)+PMT)	0.6-3.2	220-340	10-84
Beekman et al. 2005	U-SPECT I 74 0.6mm pinholes 3 clinical detectors	0.5	2200	10.5
Van der Have et al. 2009	U-SPECT II 75 pinholes 0.35 mm 0.6 mm 1 mm	0.35 0.45 0.8	700 1800 900	12 12 27

Table 1.3 [Chaix 2015]: Survey of state-of-art preclinical SPECT systems developed over the last two decades.

1.8 This Work

This dissertation describes recent advances in a novel photon-counting gamma-ray detector called iQID, which is based on columnar scintillators, image intensifiers and fast frame CCD/CMOS sensors. Originally called BazookaSPECT and designed for planar gamma-ray imaging, iQID has been expanded to include applications in preclinical scintigraphy and SPECT, charged particle (alpha and beta) imaging and auto radiography. To investigate and advance the capabilities of iQID cameras for better imaging performance and broader applications, this work focused on improving many aspects of iQID cameras, including scintillation materials, the readout system, signal processing algorithms, system calibrations and 3D reconstructions of the FastSPECT III system. A novel high-resolution large-area iQID (LA-iQID) camera was also developed for dedicated clinical lymphatic imaging. This is the first step of translating iQID technology towards clinical nuclear medicine applications, involving state of art additive manufacturing, a novel system architecture, new calibration methods, and a high-standard of system assembly with safety considerations.

Chapter 2 provides an overview of scintillation gamma camera physics including gamma-ray optics, scintillation detectors and readout systems, and introduces the imaging principles behind iQID cameras. Sources of noise in iQID cameras have been analyzed and an advanced photon-counting algorithm that has noise-discrimination capability for suppressing certain image intensifier background signals is presented. Chapter 3 investigates the origins of poor energy resolution in iQID cameras, which is a weakness of iQID cameras that still needs to be addressed. The physics of the image intensifier will be introduced in detail. A Monte Carlo simulation of the image intensifier's micro-channel plate (MCP) gain stage will be reported. Finally experimental validation and solutions for improving the energy resolution of iQID cameras are proposed. Chapter 4 presents recent advances in the FastSPECT III system that is an ultra-high-resolution SPECT system incorporating 20 iQID cameras. Work described includes scintillator upgrades, new system calibration method, helical bed scanning and whole-body mouse imaging. Chapter 5 introduces the novel design and development of the Large-Area iQID (LA-iQID), including a high-resolution parallel-hole collimator design, novel system architecture and assembly, data acquisition system, camera calibration, performance evaluation, portability and mobility for easy handling and

on-site applications at remote locations where hospital facilities are not available. Chapter 6 summarizes the achievements of this work and suggests future directions of iQID technology development.

CHAPTER 2

DETECTORS

Since its development in 1958, the Anger camera has been widely used in clinical nuclear medicine applications and it is the basis of the modern gamma cameras employed in commercial dual-headed & triple-headed SPECT systems. Also called the Anger scintillation camera, the Anger camera used a NaI(Tl) scintillation crystal for gamma-ray detection, a light guide to allow scintillation light to spread out, and photomultiplier tubes (PMTs) for signal readout. Although configurations similar to Anger cameras are still widely used in clinical applications, many other different types of scintillation gamma cameras have emerged over the last few decades, especially in preclinical applications where small area detectors can be used. [Peterson and Furenlid 2011, Barrett and Hunter 2005] For example, the iQID camera is a novel scintillation gamma camera developed at the Center for Gamma-Ray Imaging that utilizes structured scintillators for detecting gamma-ray photons, image intensifiers for optical gain and fast-frame-rate CCD/CMOS sensors for signal readout. [Miller et al. 2006, 2008, 2009, 2012, 2014]

This chapter presents the physical processes involved in scintillation gamma cameras, including interactions between gamma-ray photons and scintillator materials, and alternatives for scintillation-signal readout. Finally the iQID camera will be introduced with its unique properties, and highlight the features that distinguish it from other gamma cameras with similar configurations. Different configurations of iQID cameras and event-estimation methods will also be presented.

All gamma cameras are equipped with gamma-ray optics in front of the detectors in order to form images of the object or radiotracer distribution, except for the ones used in PET systems, which depend on annihilation gamma-ray coincidence detection to create correspondences between object and image. Since this dissertation mainly focuses on advancing the iQID technology for scintigraphy and SPECT applications, the discussion of imaging principles of scintillation gamma cameras will not be complete without introducing the principles of gamma-ray image formation.

2.1 Gamma Image Formation

In theory, images can be formed by bending, blocking or constraining propagating electromagnetic waves. Lenses, mirrors and pinholes are all basic optical elements that utilize either bending or blocking of visible light to form an image. As introduced in the first chapter, gamma rays are also electromagnetic waves in nature like visible light. However, because of the ultra-short wavelength of gamma-rays (<<1Å, 1Å=0.1nm), most optical elements working in the visible range cannot be directly applied to gamma rays, and specially designed and manufactured elements are required for gamma-ray image formation.

For visible light, there are typically four different physical processes that can be used to form an image, i.e. refraction, reflection, diffraction and absorption. For gamma-rays, however, the real part of the index of refraction for common materials is so close to 1 that the refraction angle is too small to be useful, and the reflection and diffraction angles are too glancing, to be practical. Although it sounds unsophisticated, absorption is currently the most effective optical principle that is commonly used in modern nuclear-imaging systems. It's also the imaging principle used on the first camera invented, the *camera obscura* or pinhole camera. By absorbing rays from all unwanted directions and only keeping those connecting the pinhole and points on the detector plane, an image can be formed. For visible light, because the photon energy is small and penetration power is weak, a piece of paper with a small hole on it may be used for imaging. For high-energy and strongly-penetrating gamma rays, the absorption material needs to have very high stopping power if the pinhole is to work effectively.

The absorption of light basically follows an exponential relationship in a material of constant composition and density and is described by Beer's Law:

$$\frac{I(E)}{I_0(E)} = \exp[-\mu_Z(\mathrm{E})\mathrm{d}] \tag{2.1}$$

where I_0 and I are the intensity of light before and after passing through the material, d is the length of propagation inside the material, $\mu_Z(\mathrm{E})$ is the attenuation coefficient as a function of the photon energy E and the atomic number Z of a specific material. From this equation we can see that effective absorption can be achieved by either increasing thickness or adopting high-attenuation-coefficient materials (typically meaning high atomic number). However,

using highly attenuating materials is always more effective and the preferred approach. [McMaster et al. 1969]

Many different types of gamma-ray imaging elements have been developed based on the absorption principle. The most common two, however, are the pinhole aperture and the parallel-hole collimator.

2.1.1 Pinhole Aperture

Image-forming elements in a gamma camera or SPECT system are of vital importance for overall system performance, including a tradeoff between resolution, sensitivity and field of view. [Barrett and Swindell 1981] Optimization is usually required in the design of such elements to balance the tradeoff and offer best performance within a fabrication budget.

Pinhole apertures are manufactured by creating a small opening in a disk or cylinder made from effective gamma-ray stopping materials, such as tungsten, lead, gold and platinum. A "keel-edge" pinhole aperture with typical shape is shown in Figure 2.1. The diameter, acceptance angle, material, and thickness are some design parameters of the pinhole aperture. [Metzler et al. 2001, Furenlid et al. 2005] Others include the distances from the pinhole to the object and to the image, which are also critical factors affecting system performance. [Jaszczak et al. 1994]

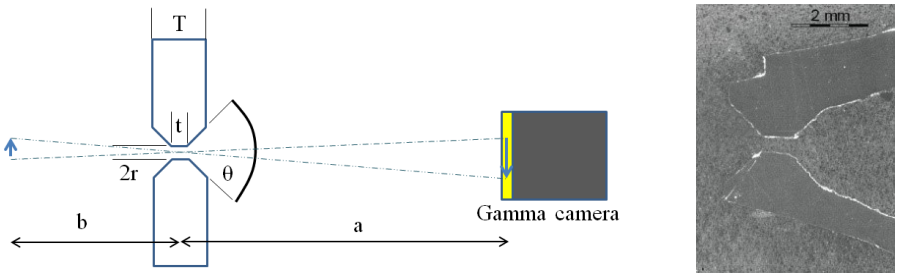

Figure 2.1: Pinhole aperture. Left: geometry of a typical pinhole aperture and imaging relationship. Right [Miller 2012b]: central slice of a pinhole aperture casted by Rapid Toolmaker [RTM].

The system sensitivity is determined by the geometric efficiency of gamma-ray imaging elements in combination with the detector stopping power and quantum efficiency. In a system with a pinhole aperture, the diameter of the pinhole and the pinhole-to-object distance determine the geometric efficiency as represented in equation 2.2, which is

approximately the ratio of the area of the pinhole and the area of the surface of a sphere centered at the object,

$$S = \frac{r^2}{4b^2}, \tag{2.2}$$

where r is the radius of the pinhole opening and b is the distance from the pinhole to the center of FOV.

The system resolution is a function of both detector resolution and imaging-element resolution. In preclinical systems, detector resolution is sometimes much better than the imaging element, making the latter the dominant factor. For a pinhole aperture, the introduced blur or "geometric" resolution can be calculated by

$$R = \frac{2r(a+b)}{b}, \tag{2.3}$$

where a is the normal distance from the pinhole to the gamma detector. For scintigraphy applications, the final image resolution is affected by both detector resolution and pinhole resolution in an approximately quadratic fashion (exactly true for Gaussian blur functions). For SPECT systems, however, the use of a reconstruction algorithm based on system calibration may partially compensate for pinhole and detector blur.

Finally, another important parameter of a pinhole aperture is magnification, which is simply described by

$$M = -a/b \tag{2.4}$$

The primary design consideration for a pinhole aperture is to provide enough FOV based on the available detector area, which is accomplished by choosing the proper magnification. In planar imaging systems, the FOV is defined by projecting the detector area through the pinhole into the object volume. In SPECT systems, however, the FOV is defined by the intersection volume of detector projections from either multiple gamma cameras (stationary SPECT) or by rotating a single gamma camera (rotation SPECT) through its angular-sampling steps. The volume so defined is called the common FOV. The total FOV defined by the union of all detector back projections also needs to be considered. When there is radioactivity outside of the common FOV but inside the total FOV, artifacts will result in the

final reconstructed image unless countermeasures are taken. Chapter 4 presents a novel method for system calibration in such situations.

In pinhole aperture design, other considerations must also be taken into account. The object is usually 3D, so portions of the object at different depths will have significantly different magnifications, sensitivities and field of view. When the object size is large relative to the center-of-object-to-pinhole distance, vignetting can occur at the edges of the FOV, causing significant sensitivity loss and irregular pinhole projections.

There is a tradeoff between resolution, sensitivity and FOV. As can be seen from equations (2.2)-(2.4), decreasing the object-to-pinhole distance may increase the system sensitivity, but only at the expense of resolution; using smaller diameter pinholes may improve the system resolution, but sensitivity will be compromised. It may seem that increasing the acceptance angle of a pinhole helps to increase the FOV at no cost to resolution and/or sensitivity; however, thinner material caused by enlarged acceptance angle leads to more penetration through the material around the edge of the pinhole that can severely affect system resolution and image contrast.

2.1.2 Parallel-Hole Collimator

Parallel-hole collimators are the other widely used gamma-ray imaging elements, especially in scintigraphy applications and clinical systems. With parallel-bore structures in hexagonal, circular or rectangular patterns of gamma-ray stopping materials, parallel-hole collimators are able to form an image of the object. Figure 2.2 shows the imaging principle of parallel-hole collimation along with examples of real devices. Each bore of the collimator corresponds to a conical region through the object. The magnification provided by a parallel-hole collimator is 1:1 for any object-to-collimator distance, leading to a nearly fixed FOV equal to the area of the collimator. This is advantageous over pinhole apertures in scintigraphy applications because other radioactivity outside the FOV will not be sensed by the detector and affect the image quality. 1:1 magnification also provides distortion-free 2D image of the object. There are also many variations of the standard parallel-hole collimator such as fan-beam collimators, the bores of which are made to converge or diverge in one or two directions, providing for magnification or minification.

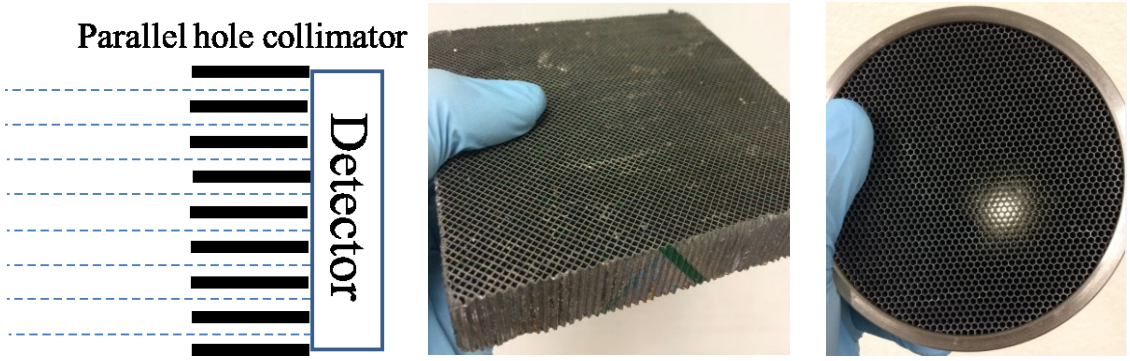

Figure 2.2: Parallel-hole collimators. Left: The imaging principle of parallel-hole collimator. Middle: A square pattern parallel-hole collimator. Right: Hexagonal pattern. The bright spot illustrates the acceptance angle of the collimator.

The geometric efficiency of parallel-hole collimator is determined by the aspect ratio (the ratio of bore length and bore diameter) and packing factor as

$$S = \left(\frac{A_b}{4\pi L_b^2}\right) F, \tag{2.5}$$

where A_b is the area of each bore, L_b is the length of each bore, F is the packing factor defined by the ratio of bore area and unit cell area. [Gunter 1996] We can see that geometric efficiency of parallel-hole collimator can be improved by decreasing the aspect ratio or increasing the packing factor. The object-to-collimator distance, however, has no effect on the geometric efficiency.

The geometric blur caused by parallel-hole collimator is proportional to the object-to-collimator distance and bore diameter. Increasing bore length can reduce the blur but eventually it will be limited by the bore diameter. Equation (2.6) shows the proportionality between blur or resolution and geometric parameters of parallel-hole collimator.

$$R \propto D_b \frac{(L_0 + L_b)}{L_b} \tag{2.6}$$

When designing a parallel-hole collimator, an important factor beyond sensitivity and resolution is penetration, which is mainly determined by the material and the septal distance or wall thickness between two adjacent bores. Penetration can greatly affect collimator resolution, causing deviations from the expected geometric blur. Typically 5% or less penetration probability for a gamma-ray photon passing through the wall is required to provide acceptable image contrast. There is also a tradeoff between penetration, sensitivity

and resolution. When septal distance is increased, penetration can be reduced whereas sensitivity is compromised by the reduction in open bore size. When penetration is fixed, increasing bore diameter improves sensitivity, but only at the cost of reduced resolution performance.

For preclinical applications, high-resolution performance is required, posing great challenge for designing and manufacturing parallel-hole collimators. With requirements for a few-hundred-microns bore diameter with high aspect ratio and acceptable penetration, designs cannot be realized using the traditional manufacturing methods (1-2mm diameter bores minimum). Fortunately a new method based on photolithographic etching has been developed by [Tecomet, Inc] for manufacturing parallel-hole collimator with ultra-fine structures, although the cost needs to be balanced with the performance. Figure 2.3 shows a custom high-resolution parallel-hole collimator designed by Brian Miller and Brad Barber for low-energy gamma-ray imaging (~30keV) and manufactured with the photolithographic etching and layer lamination technique. Chapter 5 presents the design and testing of a customized high-resolution parallel-hole collimator based on this new method but for higher-energy gamma-ray imaging (~140keV).

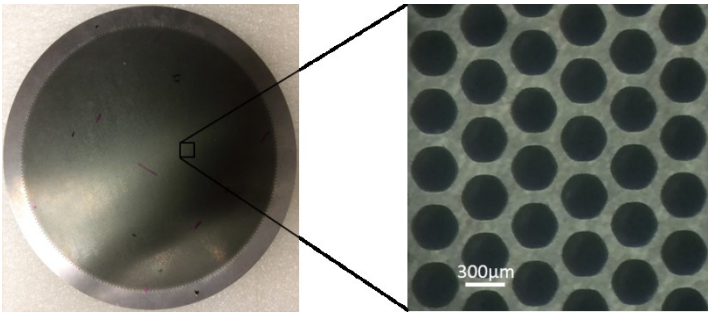

Figure 2.3: A low-energy high-resolution parallel-hole collimator manufactured with photolithographic etching.

2.2 Interaction of Gamma Rays with Matter

The detection of gamma rays is based on their interactions with matter. Upon initial interactions with matter, three physical energy-absorbing processes can occur: photoelectric absorption, Compton scattering, and pair production. In the field of nuclear imaging, gamma-ray energies typically vary between 30-511keV, at which range photoelectric absorption and Compton scattering are the main physical processes. Pair production occurs

with significant probability only for gamma-ray energies of 1.022 MeV or more, so it will not be considered in this dissertation.

2.2.1 Photoelectric Absorption

In the photoelectric absorption process, a gamma-ray photon interacts with a material atom, loses all of its energy, and excites a high-energy photoelectron out of its shell as shown in Figure 2.4. Because of the high energy of the gamma-ray photon, the photoelectron is usually excited from the most tightly bound shell or K shell of an atom. The process can be described by

$$E^{-} = h\nu - E_b \,, \tag{2.7}$$

where E_b is the binding energy of the photoelectron, E^{-} is the energy of the excited photoelectron.

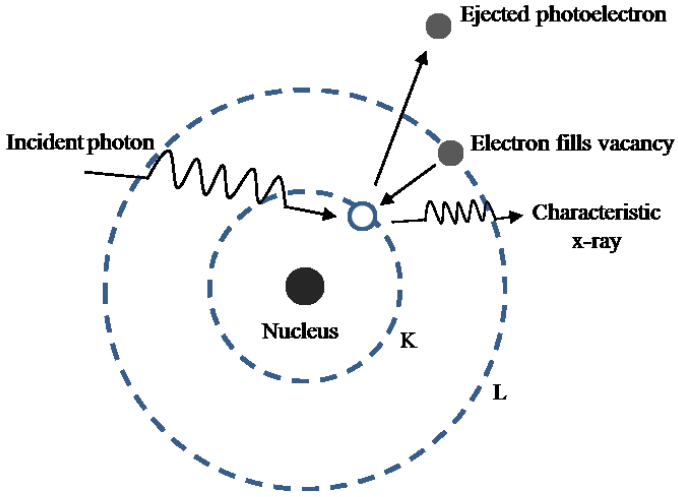

Figure 2.4: Schematic demo of the photoelectric effect.

Because the binding energy is smaller than the energy of the gamma-ray photon, the excited photoelectron carries much of the energy of the original gamma-ray photon. For example, in a CZT detector, a 140keV gamma-ray photon at initial interaction can produce a photoelectron with energy of around 100-120keV. In addition to the high-energy photoelectron, one or more characteristic X-ray fluorescence photons or alternatively Auger electrons (lower probability) can be generated during filling of the vacancy left by the photoelectron by electrons from higher shells, which can interact via another photoelectric

effect (higher probability because of its short range of about 100μm) or escape from the material (lower probability).

For lower-energy gamma-ray photons, such as in the 30-140keV typically used in scintigraphy and SPECT applications, photoelectric absorption dominates in high-atomic-number materials and Compton scattering dominates in low-atomic-number materials or tissues. Higher-atomic-number materials increase the probability of photoelectric absorption relative to Compton scattering.

2.2.2 Compton Scattering

Besides the photoelectric effect, Compton scattering is the other primary physical process that can happen as an initial or secondary interaction. When Compton scattering occurs, the incident gamma-ray photon transfers part of its energy to an electron known as the recoil electron, and is then deflected or scattered at an angle relative to its incoming direction as shown in Figure 2.5. Depending on the scattering angle, the energy transferred can vary between a very small to a very large portion of the gamma-ray photon energy. Based on the conservation of energy and momentum in a relativistic framework, the scattered gamma-ray photon energy is given by

$$h\nu' = \frac{h\nu}{1+\frac{h\nu}{m_0c^2}(1-cos\theta)} \ , \tag{2.8}$$

where m_0c^2 (=511keV) is the rest energy of the electron. The larger the scattering angle is, the more energy is transferred to the electron. A small scattering angle with high secondary gamma-ray energy is strongly favored in a Compton scattering process.

A Compton scattered gamma-ray photon can once again interact through either photoelectric absorption to generate signal in the detector or Compton scattering to generate yet another lower-energy gamma-ray photon, in a process sometimes called a cascade.

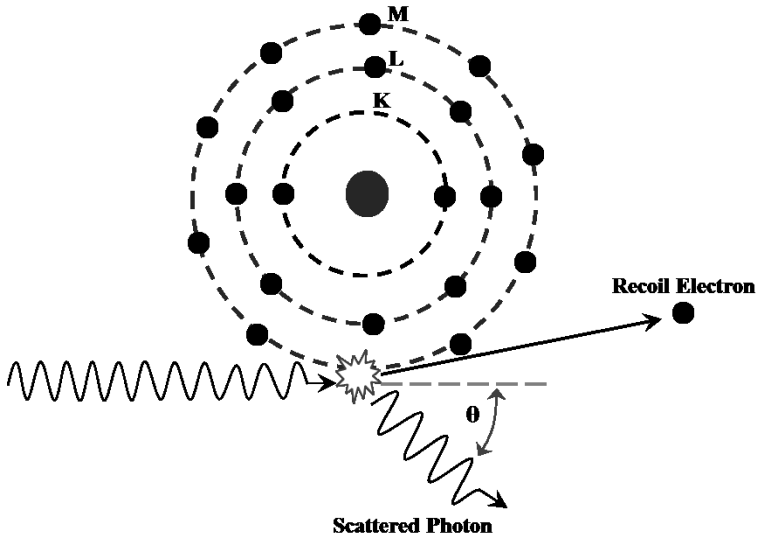

Figure 2.5: Schematic demo of the Compton scattering effect.

2.3 Scintillation Detector

After the initial interaction of a gamma-ray photon with matter, whether photoelectric absorption or Compton scattering occurs, one or more high-energy electrons are generated in the material, which through a secondary ionization process result in the creation of many electron-hole pairs, photons, or heat in proportions depending on the detector material used. [Barrett and Hunter 2005] For example, semiconductor materials can transfer the energy of the excited high-energy into a large number of electron-hole pairs, which under electric field induce electrode currents as signals. This section discusses how the high-energy electrons' energy is transferred to optical photons by scintillation materials or scintillators.

2.3.1 Physics of Scintillation Process

Generally there are two types of scintillators that can interact with x-rays or gamma-rays and emit visible light, that is, organic scintillators and inorganic scintillators. Most are solid-state crystals. Organic scintillators, however, absorb gamma-ray photons and transfer their energy into excited valence electrons, and are generally used in low-energy beta detection. Since most scintillators used in nuclear imaging are inorganic scintillators, including the ones used in this work, we only discuss the scintillation process of inorganic scintillators.

Solid State Optics

As in any solid-state crystal, an inorganic scintillator has different energy states determined by the crystal lattice (in contrast, energy states in organic scintillator are determined by molecules). Electrons have discrete energy bands, such as the valence band where electrons are bound to the lattice, the conduction band where electrons can move freely throughout the crystal, and forbidden bands where electrons cannot stay in pure crystal. After absorbing energy from a rapidly moving photoelectron, electrons can move from the valence band to the conduction band, leaving a hole in valence band and thus forming an electron-hole pair. When the electron returns to the valence band and recombines with the hole, which is called the recombination process, energy is released by emission of a photon. However, in a pure crystal, the recombination process is very inefficient partly due to reabsorption. To improve the efficiency, small amount of impurities called activators are usually introduced into pure crystals, which creates energy states in the forbidden band. The electrons can jump from the conduction band to these "luminescent" states, and then recombine with holes from there very efficiently, greatly enhancing the light emission probability. For example, the designation CsI(Tl) means the cesium iodide crystal has been doped with thallium activators. Figure 2.6 demonstrates the electron-hole pair generation process and the subsequent luminescence process through recombination at the activator locations.

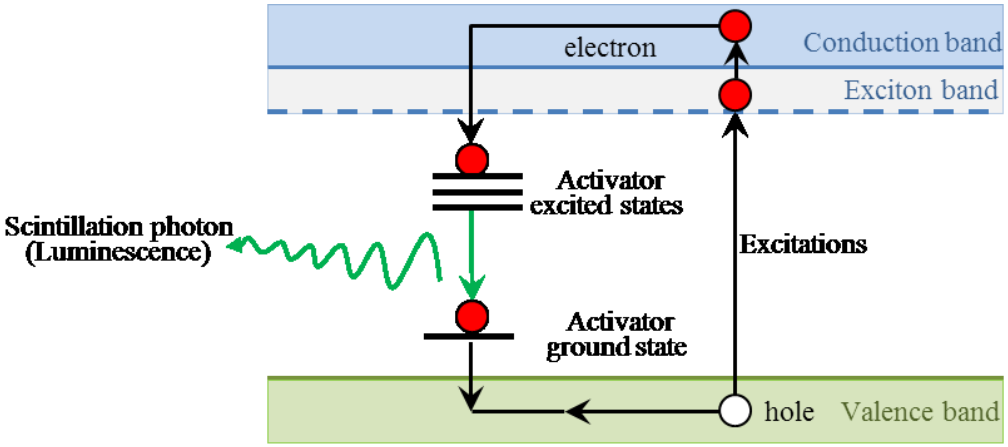

Figure 2.6: Formation of electron-hole pair and luminescence through recombination

Scintillation (Luminescence)

When a gamma-ray photon (which can be the primary photon or a secondary Compton-scattered photon) interacts with a scintillator, a high-energy electron is excited through the photoelectric absorption, which further excites a cascade of secondary electrons from valence band to conduction band, generating a large number of electron-hole pairs. The holes quickly migrate to the activators and ionize the activators. The electrons also migrate through the crystal until they meet with the ionized activators, where they lose some energy and jump into the excited energy states of the activators. Quickly and efficiently, the de-excitation or recombination process occurs and since there are many electron-hole pairs, a large number of photons are emitted with energies corresponding to the energy difference between the excited energy states and ground energy states of the activators. Another alternative is that the electron-hole pairs move to the activator together in a loosely associated state called exciton, where they excite the activator and emit photons by de-excitation. [Knoll 1999] Figure 2.7 summarizes the main physical processes occurring in a scintillator when gamma-ray photons are incident.

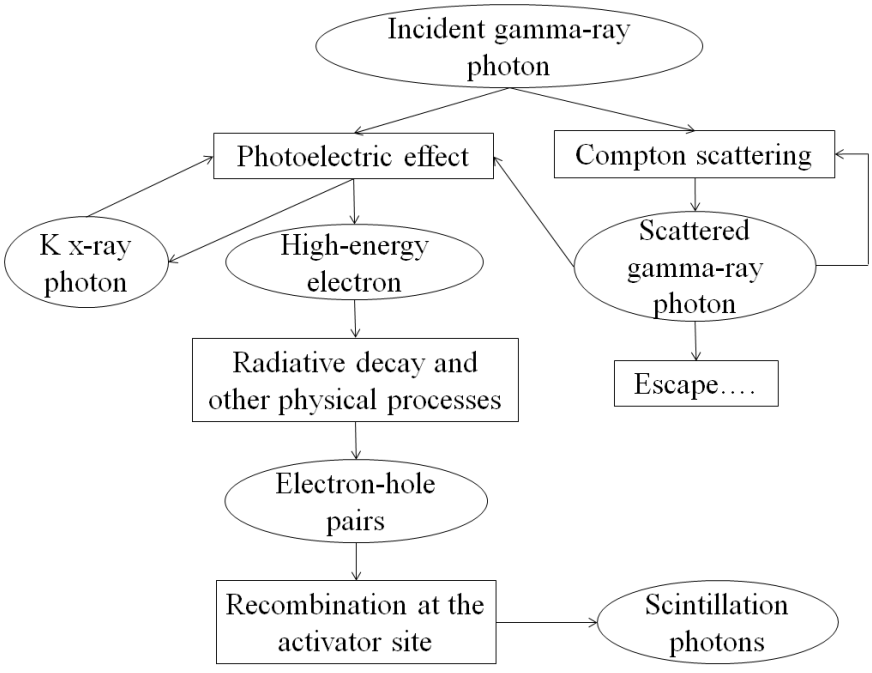

Figure 2.7: Major physical processes involved in a scintillator upon interaction with incident gamma-ray photons.

The distribution of electron-hole pairs is determined by the range of the primary photoelectron. Scintillation light generated by doped activators will never be reabsorbed by the crystal because their energies are lower than the band-gap energy. The doped crystal is therefore transparent to its scintillation light.

Besides emitting scintillation light as described above, the excited activators may go through other physical processes such as quenching and phosphorescence. Quenching is a non-radiative process that happens to some transitions between excited states and ground states of the activators, decreasing the conversion efficiency to scintillation light. Phosphorescence occurs when electrons jump to an excited state where the transition to the ground state is forbidden. More energy is then required to excite the electrons back to higher states where recombination is allowed. This process leads to slow light emission, often called after-glow. [Knoll 1999] Phosphorescence has been observed in CsI(Tl) scintillators. In the first few hours after a CsI scintillator is exposed to room light, background events are observed uniformly across the scintillator face. The background event rate then decreases slowly to a steady state.

Efficiency

Although scintillation efficiency can be greatly improved by doping, most of the energy of a gamma-ray photon is still lost by non-radiative processes and thermal emission. As an example, a NaI(Tl) scintillator has a conversion efficiency of about 12%, which means a 100keV gamma-ray photon can generate 1.2×10^4 eV scintillation light photons or 4000 photons with average energy of about 3eV. The likelihood of the radiative and non-radiative processes often varies for different deposited energies, resulting in non-linear response or light yield, called nonproportionality, which can affect the energy resolution of the scintillator. [Dorenbos et al. 1995, Valentine et al. 1998] Assuming the scintillator responds linearly to the deposited gamma-ray energy, the mean number of photons a scintillator produces upon interaction with a gamma-ray photon of energy $\mathcal{E}$ can be denoted as

$$\bar{N} = A\mathcal{E} \ , \tag{2.9}$$

where A is the net conversion efficiency and includes the efficiency of electron-hole pair production, transport efficiency, and activator luminescent efficiency. The real number of scintillation photons is often assumed to follow Poisson statistics with the variance equal the mean. However, Bora et al. [2015] have shown that the scintillation photons could follow sub-Poisson, Poisson, or super-Poisson statistics.

The gamma-ray absorption or detection efficiency of a scintillator can be calculated with equation (2.1). Basically a thicker scintillator is desired to provide higher stopping power, and therefore higher detection efficiency. Table 2.1 lists the commonly used scintillators along with their physical properties.

Scintillator	Light yield (ph/keV)	Density (g/cm^3)	Peak wavelength (nm)	Refractive index	Decay time (ns)
NaI(Tl)	38	3.67	415	1.85	230
CsI(Tl)	65	4.51	540	1.8	1000
LaBr3	61	5.3	358	1.88	35
GOS	78	7.3	547	2.2	>4000

Table 2.1: Common scintillators with their physical properties.

Ideally a good scintillator should provide high stopping power to provide a high gamma-ray detection efficiency, have a high conversion efficiency to provide a strong scintillation signal for easy detection, have an emission spectrum that matches the spectral sensitivity of the readout device, have a linear response to gamma-ray photon energy to provide high energy resolution, have short decay time to allow high count rates, have good malleability so it will not break easily, and have low hygroscopicity to be able to be used in a room environment. Based on these desirable properties, CsI(Tl) scintillators are used in this work.

2.3.2 Micro-Columnar Scintillator

Micro-columnar scintillators, also called columnar scintillators or structural scintillators, are a specially developed scintillator. [Nagarkar et al. 1995] The scintillation material is grown on a substrate via vapor-deposition techniques, resulting in many needle-like columns

perpendicular to the substrate. Each micro-column has diameter as small as 5μm. Figure 2.8 shows two cross-sections of the micro-structures of typical columnar CsI(Tl) scintillators.

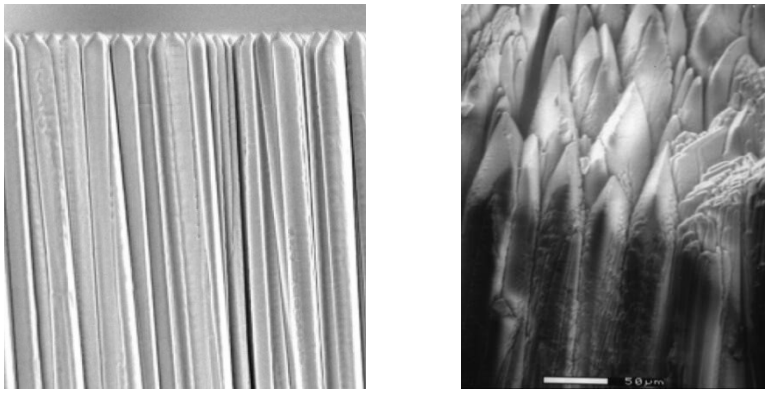

Figure 2.8: Two photographs of the micro structures of columnar CsI(Tl) scintillator manufactured by [Hamamastu] (Left) and RMD [Nagarkar et al. 1997] (Right).

The gaps between the micro-columns can be filled with air. Air's low index of refraction can create conditions for total internal reflections (TIR) inside each column for generated scintillation light. Because of TIR, the lateral spread of scintillation light can be at least partially constrained during propagation inside the scintillator, thus providing a high spatial resolution of up to ~15 lp/mm in digital radiography applications. For columnar CsI(Tl), the thickness can be fabricated to over 2000 μm, offering high x-ray and respectable gamma-ray detection efficiency. [Nagarkar et al. 1997] The area can be manufactured up to 44×44cm^2 with 1mm thickness, making it suitable for clinical applications. [Hamamatsu] Different substrates can be used for growing columnar CsI(Tl) scintillator, such as aluminum, amorphous carbon and fiber-optic plate.

With a high light yield of ~65photons/keV, high resolution of ~15 lp/mm, good sensitivity, large area, low hygroscopicity and excellent malleability, columnar CsI(Tl) scintillator has been widely used in both preclinical and clinical x-ray applications. It's also the gamma-ray converter used in iQID cameras. Because of the columnar structure and TIR effect, the light output properties are affected by the column geometry, such as the length and diameter of each column. We have found a nonproportional relationship between lateral spread of scintillation output and depth of interaction. Chapter 4 presents the effect of columnar CsI(Tl) scintillator thickness on system sensitivity and resolution with both simulated and experimental data.

2.4 Scintillation Readout

After scintillation light is produced through the luminescence process described above, it's isotropically emitted inside the scintillator. Devices that are able to sense the scintillation light and transfer its energy into electrical signals for processing are required. Depending on the type of scintillator used in gamma-ray detection, different readout systems are used.

Photomultiplier tubes (PMT), for example, were the very first scintillation readout devices used in gamma cameras and are still widely used in modern nuclear-imaging systems. When coupled to a scintillator (usually a monolithic crystal), a photocathode layer inside the front entrance window of the PMT can absorb the scintillation light photons and produce primary photoelectrons (via photoelectric absorption) into the PMT vacuum. These electrons accelerate under an applied electric field and generate a cascade of secondary electrons though a fixed number of amplification stages. The amplified secondary electrons are then collected by one or more anode structures, generating current output signals for further processing in external electronic circuits. Figure 2.9 shows a schematic view of the detection and amplification processes in a PMT.

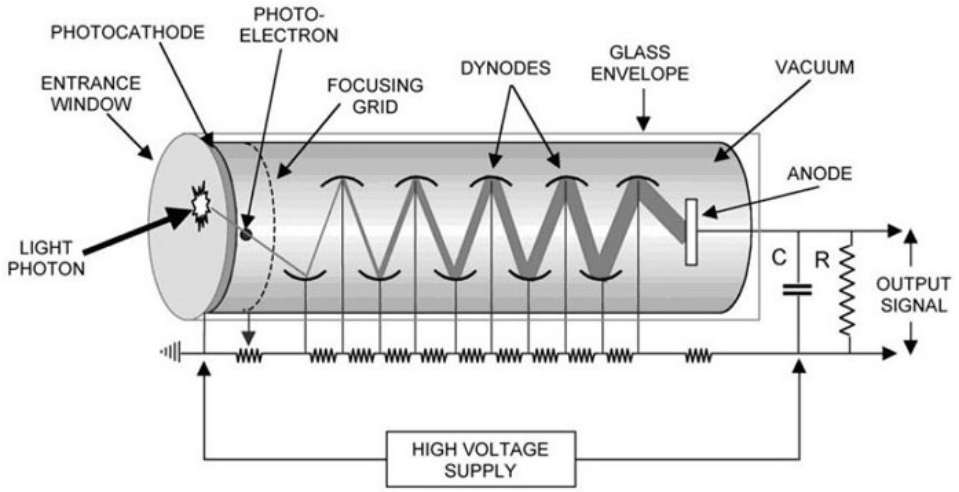

Figure 2.9 [PMT]: The photon detection and electron amplification process in a typical PMT.

Other scintillation readout systems have been developed over the years, some examples including position-sensitive PMTs (PS-PMTs), multi-anode PMTs (MA-PMTs), photodiodes, avalanche photodiodes (APDs), silicon photomultipliers (SiPMs) and CCD/CMOS sensors. Because of low conversion efficiency (<13% typically), low transport

efficiency (~10-20%) and other light-loss mechanisms, only a few thousand or fewer scintillation-light photons can make it to the readout devices. Considering also the low quantum efficiency (~10-20%) of most photosensitive detectors, it is very challenging for the readout devices to generate strong signals. As a consequence, scintillation readout systems almost always have a signal amplification process after the first generation of photoelectrons from the scintillation photons.

In the iQID cameras, a novel scintillation readout is used, namely optical amplification followed by fast frame-rate CCD/CMOS. Unlike EMCCDs, where an internal gain is used for electron multiplication before the charge-to-voltage conversion [Denvir and Conroy 2002, Hynecek 2001, Robbins and Hadwen 2003], iQID's intensified CCD/CMOS strategy employs an image intensifier to provide high-resolution high-gain optical amplification of the weak scintillation light before relaying an irradiance pattern onto a consumer-grade CCD/CMOS sensor via an optical lens system.

2.4.1 Image Intensifier

An image intensifier is a vacuum-tube electro-optical device used for amplification of light. Unlike a PMT, an image intensifier provides direct visualization of the amplified light signal with its exit-face phosphor screen. By appropriate electron optics principles during the electron-amplification process, an image intensifier can preserve the image irradiance received at the entrance face and display an intensified version at the output face, with high-resolution performance. Among the very first applications of image intensifiers was military night-vision devices used in World War II. [WIKIPEDIA Image Intensifier]

Principles

Modern image intensifiers usually start with a fiber-optic faceplate to relay the light distribution from the entrance face to a photocathode layer, where photoelectric effect occurs and primary photoelectrons are released. Under an applied voltage of a few hundred volts photoelectrons are accelerated and bombard a continuous electron amplifier called a micro-channel plate (MCP), which is a lead-glass wafer with electrodes on both sides, with up to 1000 volts potential between them, and millions of microscopic hollow bores. A primary photoelectron excites a few secondary electrons upon initial collision with the walls

of an amplifier channel of the MCP, which then pick up kinetic energy under the electric field and excite more secondary electrons upon their collisions with the wall material of the channel further down the bore. Because the dynode material is uniformly distributed in the wall material, many electron collisions, or amplification processes, may occur, resulting in a cascade of secondary electrons, known as an electron cloud. Finally a few thousands volts applied between the output of the MCP and an exit face phosphor screen collimate and accelerate the electron cloud. When the electrons cloud collides with the phosphor screen, their energy is converted back to visible light through a luminescence process for visualization or imaging purposes. Figure 2.10 shows the detection and amplification processes involved in an image intensifier.

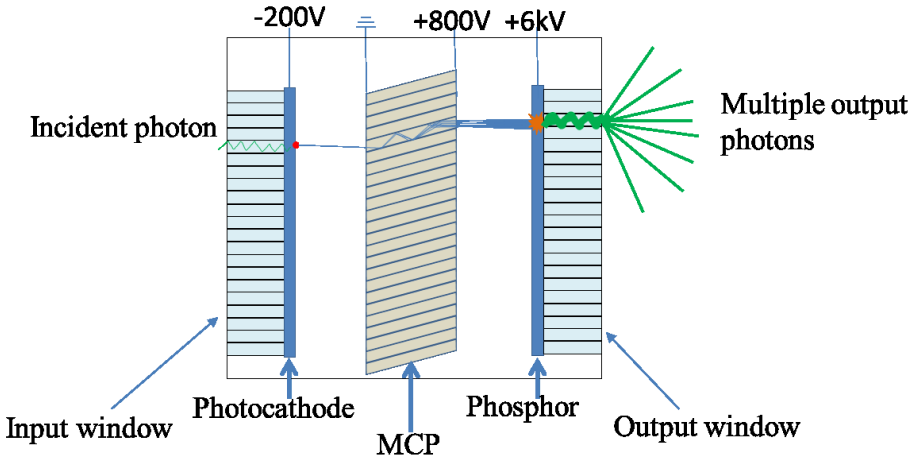

Figure 2.10: The image intensification process of an image intensifier.

Resolution

A key feature of image intensifiers is their ability to preserve high-resolution image patterns from the entrance face to the output face. Because of the use of high voltage before and after the MCP, randomly emitted electrons are quickly collimated. Each micro-bore in the MCP is a miniature electron amplifier with a diameter of ~5-15μm, which guarantees that high-resolution is maintained during amplification. Finally the fiber-optic faceplate can be used both in front of the photocathode layer and after the phosphor screen to provide high-resolution optical relay. The applied voltage, MCP bore diameter and pitch, and entrance and output windows are thus factors affecting image-intensifier resolution. Up to 80lp/mm

resolution performance has been reported by a state-of-art image-intensifier manufacturer (ProxiVision) and 50lp/mm can be easily achieved for a 1-MCP image intensifier with 25 mm diameter.

Gain

The overall gain of an image intensifier depends on the quantum efficiency of the photocathode layer, the MCP gain, and the efficiency of the phosphor screen under applied voltage conditions. Different photocathode materials have different spectral sensitivities S (mA/W), where S is defined as the ratio of photoelectron current (mA) to radiant flux (W) for a particular wavelength. Figure 2.11 shows the spectral sensitivity of different photocathode materials. The quantum efficiency of a photocathode material, defined as the ratio of emitted number of photoelectrons to incident number of photons, can then be calculated by

$$\eta_{QE} = \frac{hc}{\lambda e} S = \frac{1.24}{\lambda} S \,, \tag{2.10}$$

where h is Planck's constant, λ is the wavelength of incident light in units of nanometer, c is the speed of light in vacuum and e is the electron charge. When coupled to a scintillator, the mean number of photoelectrons generated from region m of the photocathode can be calculated as

$$\bar{n}_m(x, y, z, \mathcal{E}) = A\mathcal{E}\eta_{QE}\eta_m(x, y, z) + \bar{n}_m^{dark} \tag{2.11}$$

where x, y, z are the 3D coordinate of gamma-ray interaction, η_m is the fraction of scintillation photons received in region m of the photocathode, $\bar{n}_m^{dark}$ is the number of photoelectrons from dark emission by thermal excitation, A and Ɛ are the net conversion efficiency of the scintillator and the gamma-ray photon energy, respectively, as used in equation (2.9).

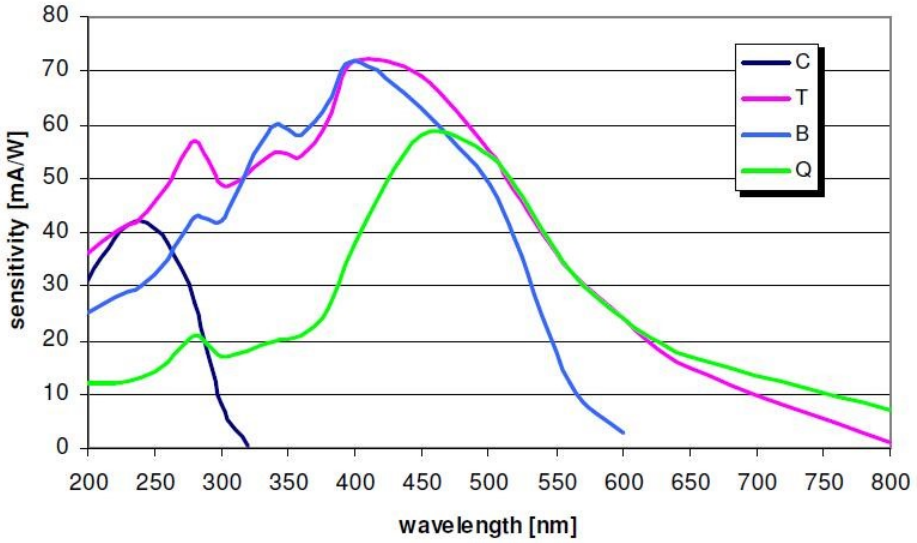

Figure 2.11 [Proxivision]: The spectral sensitivity of different photocathode materials. C: Advanced Solar Blind. T: Bialkali. B: UV Enhanced S 20. Q: S 20.

The efficiency of the phosphor screen also varies for different materials under different voltages. The higher the voltage applied between the MCP output and the phosphor screen, the higher the efficiency that can be achieved as the electron energy is increased. Table 2.2 lists the light emission properties and efficiencies for different phosphor materials.

Type	Composition	Max emission wavelength (nm)	Efficiency (W/mA)			
			6kV	10kV	12kV	15kV
P43	Gd2O2S:Tb	545	0.43	0.77	0.97	1.28
P46	Y3Al5O12:Ce	530	0.22	0.39	0.49	0.65
P47	Y2SiO5:Ce,Tb	400	0.62	1.35	1.71	2.24

Table 2.2 [Proxivision]: The maximum emission wavelengths and efficiency under different voltages for different phosphor materials.

Finally, the gain of an MCP depends on the geometry of the MCP bores, the applied voltage and current, the material used, and the number of consecutive MCPs, so there is no simple equation or relation to define the MCP gain. A typical electron gain for 1 MCP working at 800 volts is about ~350 electrons/electrons, and for 2 back to back MCPs working at 1800 volts, the gain is up to ~10^6 electrons/electrons. If we denote the phosphor screen efficiency as F and average MCP electron gain as $\bar{G}$, the total average optical gain of the image intensifier can be represented as

$$G_{tot} = \eta_{QE} \times \bar{G} \times F \tag{2.12}$$

For example, if an image intensifier uses a Bialkali photocathode on a quartz input window, 1 MCP with 800 volts applied, and a P43 phosphor screen with 6kV final acceleration stage, the average optical gain for amplifying 540nm wavelength light photons is

$$20\text{mA/W} \times 0.43\text{W/mA} \times 350 = 3010\ \text{W/W}$$

Although the image intensifier can provide ultra-high gain with high-resolution performance, a large variation of the gain between different photoelectrons has also been observed, severely affecting energy resolution of the image intensified detector. Chapter 3 introduces details of electron amplification processes of MCP along with Monte Carlo simulations to investigate the origin of the gain variation and whether its effects on the energy resolution of iQID can be addressed.

2.4.2 CCD and CMOS Sensors

CCD and CMOS sensors are well known devices used in modern imaging cameras. In recent developments of novel scintillation gamma cameras, CCD and CMOS sensors have also been demonstrated as useful scintillation readout devices with some advantages over other types of scintillation-readout systems. [Taylor 2004, Miller et al. 2007] In iQID cameras, the use of image intensifiers for optical amplification allows a consumer-grade CCD/CMOS to be used as the readout since the signal amplitude easily dominates over read-out noise sources. This greatly lowers the cost and expands the available options for building customized cameras. To understand the detection physics of CCD/CMOS detectors, a basic understanding of the p-n junction is required.

P-N Junction

A p-n junction is formed at the interface between a p-type semiconductor material and n-type semiconductor material. The p-type semiconductor is an intrinsic semiconductor doped with acceptor impurities such as boron, aluminum or gallium, which creates free holes that become the majority carriers. N-type semiconductor is instead doped with donor impurities such as phosphorus, which creates free electrons such that electrons are the majority carriers. Where p-type material and n-type material meet, the free electrons in n-type material will

combine with the free holes in p-type material near the boundary, leaving bound positive atoms on the n-side and negative atoms on the p-side, which induces an electric field across a volume surrounding the boundary called the depletion region. The motion of the free carriers is then balanced with the electric field until an equilibrium state is reached, forming a potential barrier. When a photoelectric effect occurs in the depletion region to generate electron-hole pairs, electrons will move to the n-side and holes will move to the p-side under the electric field before recombination can occur. This induces a current on contact electrodes that can be measured with charge-sensitive electronics. Figure 2.12 demonstrates the p-n junction and the potential barrier at the depletion region.

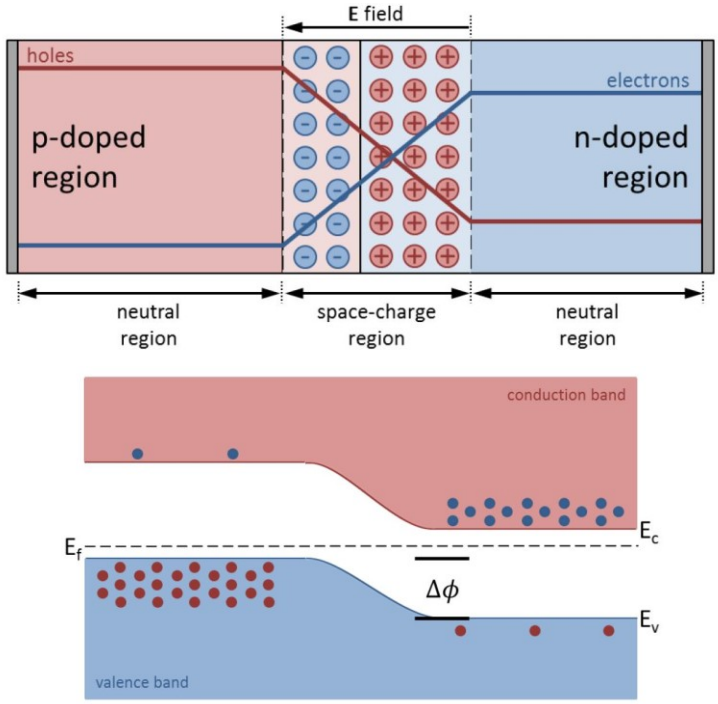

Figure 2.12 [Durko 2014]: Demonstration of P-N junction (Top) and the resulting potential barrier (Bottom).

No external electric field is required to create the above p-n junction. If an external positive voltage is applied from the p-side to the n-side, a forward bias configuration is formed. The applied electric field will reduce the strength of the internal electric field, causing the depletion region to shrink and lower the potential barrier. However, when an voltage is applied from n-side to p-side, a reverse bias configuration is formed that enhances the internal electric field, expands the depletion region and increases the potential barrier.

Figure 2.13 depicts the potential barriers for forward bias and reverse biased p-n junction configurations.

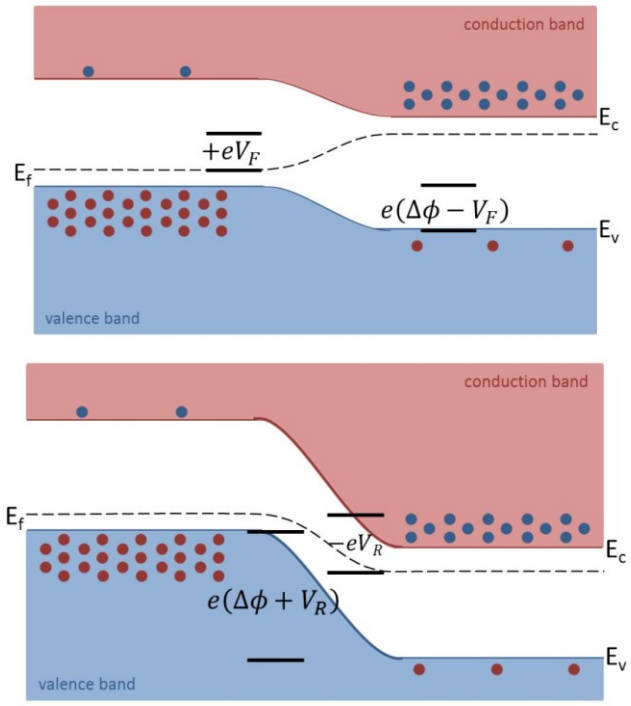

Figure 2.13 [Durko 2014]: Demonstration of smaller potential barrier in a forward bias p-n junction (Top) and larger potential barrier in a reverse bias p-n junction (Bottom).

CCD

In a CCD (Charge-Coupled Device) sensor, a buried-channel metal-oxide-semiconductor (MOS) structure is typically used. As shown in Figure 2.14, a thin layer of n-type semiconductor is sandwiched between a silicon dioxide insulator layer and a p-type semiconductor substrate. On top of the insulator layer are placed electrodes, also known as gates. An external electric field is provided by the electrodes such that the p-n junction structure forms an reverse biased configuration, which results in a potential well at the location of the n-type semiconductor layer. This potential well is the so-called “buried channel” and will be used to store electrons during exposure and shift electrons during readout.

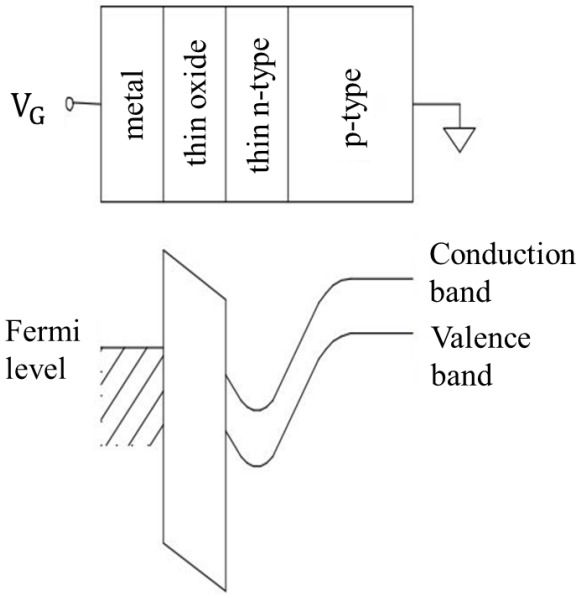

Figure 2.14 [Felber 2002]: MOS configuration of a CCD pixel along with the resulting potential well.

When light is absorbed in the depletion layer through the photoelectric effect, electron-hole pairs are generated and before they can recombine the electrons are collected in a potential well under an electrode. The electric charge accumulated during a frame period will be transferred to its neighboring capacitor by clocking of electrode voltages controlled by a circuit as shown in Figure 2.15. The transferring process is performed by a vertical register followed by a horizontal register until the charge is transferred to the last well, where a charge amplifier will be used to convert the electric charge into a voltage for sampling and digitizing via analog-to-digital (A/D) electronics. The same process is repeated for all rows and columns until the content of the whole image is converted into a voltage sequence.

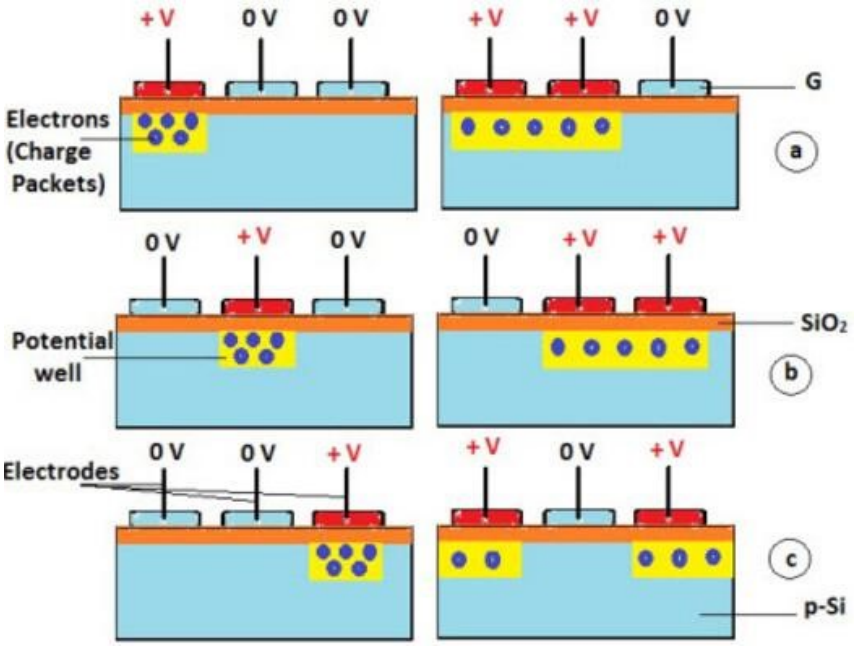

Figure 2.15 [Agarwal]: Demonstration of charge transportation by shift register in CCD sensor.

Because the number of the electrons is proportional to the fluence of incident light, the light distribution in the image is represented by the distribution of collected electrons across all pixels of the CCD sensor. The quantum efficiency for CCDs is relatively high compared with other light-detection techniques, ranging from .25 to .95. There are, however, two main noise sources in a CCD sensor, i.e. dark current and readout noise. Dark current is caused by thermally excited electrons that collect in the pixel, which cannot be distinguished from electrons generated by light absorption, but their rate of production can be significantly reduced by cooling. Readout noise is the limiting factor of CCDs and is generated during charge-to-voltage conversion by high bandwidth amplification. The bit depth of a CCD sensor is affected by the maximum electron capacity of the potential wells, which mainly depends on the pixel size (larger pixel size tends to have a larger maximum capacity).

CMOS

The CMOS (Complementary Metal-Oxide Semiconductor) sensor is also manufactured based on MOS technology and depends on similar physical processes for light detection. The readout electronics architecture of CMOS sensors, however, is different from CCD sensors. Each pixel in a CMOS has its own charge-to-voltage (transimpedance) amplifier,

and sample and hold capacitor circuits so that integrated photoelectron signals in pixels can be readout via multiple buses, which greatly boosts the readout speed. The frame rate of a CMOS sensor, therefore, can be one or two orders higher than CCD sensor, providing higher count-rate capability in photon-counting applications.

Table 2.3 compares relevant performances of PMT, CCD and CMOS as scintillation readout devices used in gamma cameras.

	PMT	CCD	CMOS
Spectral Sensitivity (nm)	300-900	300-1100	400-1100
Quantum Efficiency (%)	5-20	25-95	15-35
Number Channels	Small	Large	Large
Detection Speed	Fastest	Slow	Fast

Table 2.3: Scintillation-readout-related performances comparison between PMT, CCD and CMOS.

2.5 The iQID Scintillation Camera

The iQID CCD/CMOS-based gamma camera was developed in recent years. [Miller et al. 2009, 2014] Their high-resolution capabilities and large space-bandwidth products have made them an interesting option for gamma-ray imaging, especially for preclinical SPECT. Different configurations have been used in these gamma cameras. Non-amplifying, low-noise high-quantum-efficiency CCD sensors have been coupled through a fiber-optic taper or lenses to a scintillator to directly capture the scintillation light produced by each gamma-ray interaction without amplification. [Miller et al. 2007, Taylor 2004] However, this configuration cannot provide high enough S/N ratio for individual low or medium-energy gamma-ray photon detection. The count-rate capability is also limited by the long readout time of these low-noise sensors. Electron-multiplying CCDs (EMCCDs) as an alternative to non-amplifying CCDs have internal charge amplification before readout and have been used in gamma cameras by several groups. Because of the signal amplification, EMCCD can be operated at moderate frame rates, for example, 512×512 pixel resolution at ~30fps, which is not high enough for photon count. Spatial resolution of about 100μm has been reported. [Miller et al. 2006a, Nagarkar et al. 2007, Teo et al. 2005] Both fiber-optic tapers and de-magnifier (DM) tubes have been used between the scintillator and EMCCD to increase the

detection area. [Meng 2006] However, in addition to the moderate frame rates, EMCCDs have some other disadvantages that are limiting their applications, including the need for complicated cooling systems, high costs and only moderate gains to amplify signals above noise level.

iQID stands for intensified Quantum-Imaging Detector and was developed in the Center for Gamma-Ray Imaging at the University of Arizona. Originally called BazookaSPECT and designed for small-animal gamma-ray imaging, iQID has all of the advantages of CCD/CMOS-based gamma cameras while not suffering from many disadvantages. Later, iQID was also demonstrated to have the capabilities of particle imaging such as alpha-particles, beta-particles, neutrons and fission fragments, which gave it the new name of iQID. [Miller et al. 2014] In this dissertation, however, the iQID camera will be introduced and advanced only in the context of gamma-ray imaging.

2.5.1 Camera Configurations

Principles

As a novel gamma camera, an iQID camera is equipped with pinhole or parallel-hole collimator, columnar scintillator, image intensifier, lens and CCD/CMOS sensor. As shown in Figure 2.16, a parallel-hole collimator is used to image the radiotracer distribution onto a columnar scintillator. The scintillation light generated by a gamma-ray-photon interaction is transported in the micro-channels through TIR to the exit face of the scintillator. An image intensifier interacts with the scintillation light using a photocathode layer deposited on a fiber-optic faceplate, where photoelectrons are generated. An MCP amplifies the photoelectrons and produces a cascade of secondary electrons, which are accelerated and transfer their energy back to visible light via a phosphor screen. Finally the amplified scintillation light is imaged onto a consumer-grade CCD/CMOS sensor through a lens system.

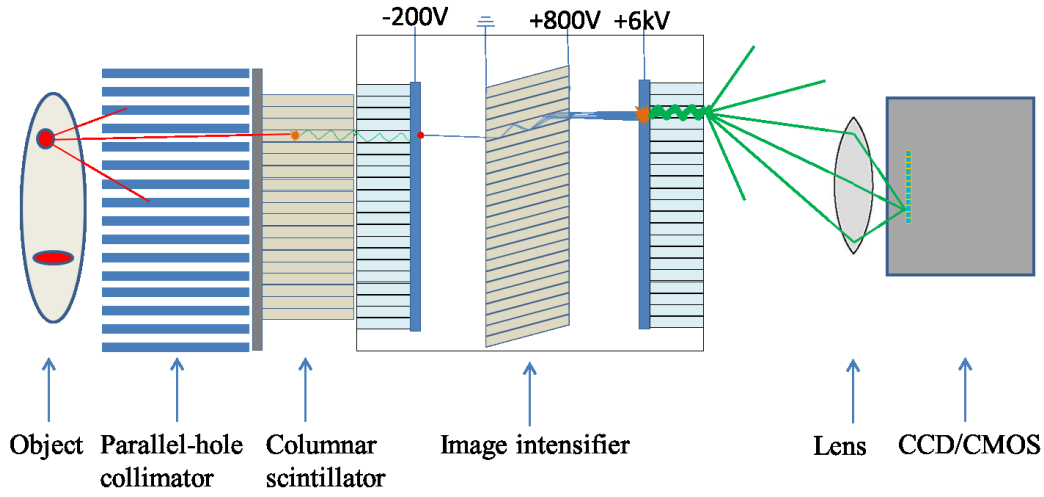

Figure 2.16: The configurations and imaging principle of a typical iQID camera.

Advantages

iQID scintillation cameras have many advantages over other gamma cameras. Because the scintillation light propagation is constrained by the micro-columnar structures and the electron amplification is constrained by the micro-channel structures, the whole detection and readout process maintains high spatial resolution (<100μm). The active area of image intensifiers is typically 25mm (diameter) or 40mm, however, a fiber-optic taper can be used to couple the scintillator to the image intensifier, which greatly increases the detection area to 100mm or larger. Because of the use of consumer-grade CCD/CMOS sensors, no cooling system is required and the sensor can operate in room temperature with high frame rates (up to 10^5 fps or more) [Photron], which makes iQID a photon-counting gamma camera with high count-rate capability. The digital frames can be captured by a simple frame-grabber card via IEEE 1394 FireWire or USB cables, for convenient interfacing between the camera and a PC. List-mode data can be acquired in real-time and gamma-ray images can be visualized in real-time. Also, the iQID camera can be assembled in a compact and portable form. Finally, because there are many off-the-shelf configurations for the columnar scintillator, image intensifier and CCD/CMOS sensor, the iQID can be easily customized with different components to meet specific performance and/or cost requirements. Figure 2.17 shows different configurations of iQID cameras, where different image intensifiers and CCD/CMOS sensors, as well as fiber-optic tapers, have been used.

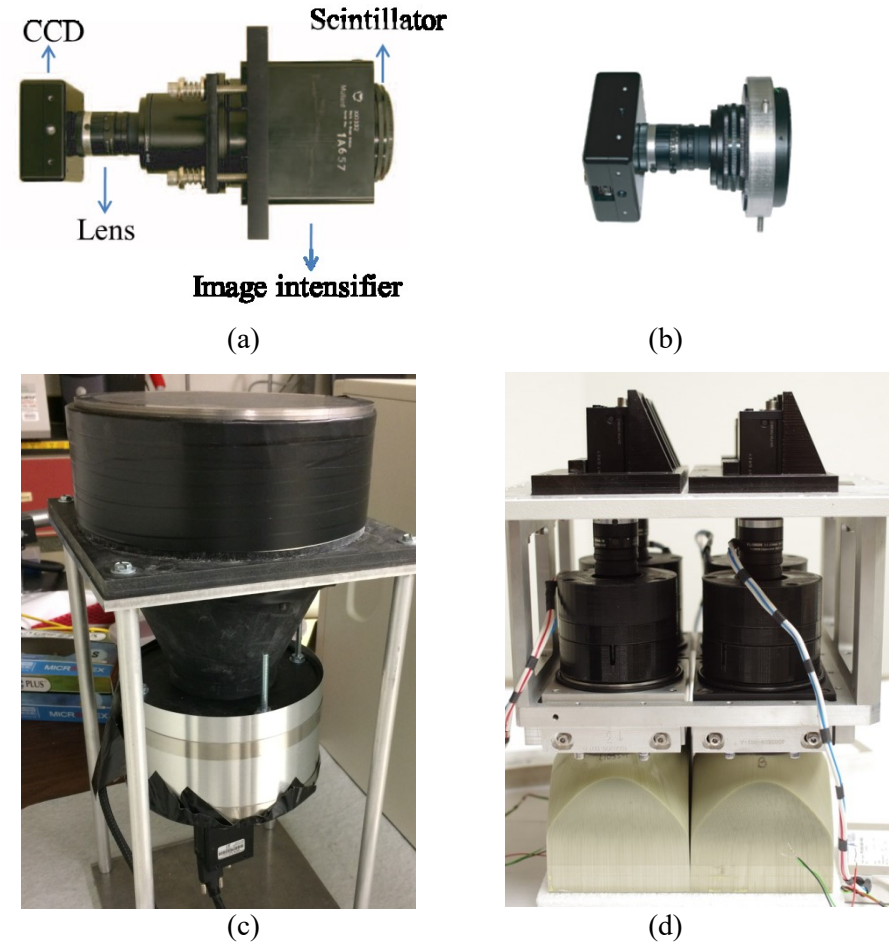

Figure 2.17: Different configurations of iQID camera. (a) Second generation image intensifier with 50mm diameter input and 640×480 CCD sensor. (b) Third generation image intensifier with 25mm diameter input and 640×480 CCD sensor. (c) Fiber-optic taper, third generation image intensifier with 25mm diameter input and 640×480 CCD sensor. (d) Fiber-optic taper, third generation image intensifier with 25mm diameter input and 1024×1024 CCD sensor.

2.5.2 Sources of Noise

In nuclear medicine, the quality of a gamma-ray image is important in both detection tasks and estimation tasks. Many factors can degrade the image quality, including inherent properties of the imaging system such as spatial resolution, energy resolution, sensitivity and distortion, and external properties of the object or patient such as the patient distance and organ movements. Noise in the imaging system can come from different sources and mix together in the final image, reducing image quality, image contrast and S/N ratio, and

leading to artifacts in 3D reconstructed images. This section introduces different sources of noise observed in iQID scintillation cameras.

Upon capture of a single frame of raw data from the CCD/CMOS sensor, the first type of noise that is directly seen is the thermal noise or dark current from the sensor, which usually has low intensity compared with real gamma-ray interaction events and can be easily removed by applying an amplitude threshold in image post processing. Since there are very many pixels as readout channels in a CCD/CMOS sensor, some pixels are inevitably defective and may appear as bright pixels, often called “hot pixels”. Although these hot pixels can have comparable or higher intensity than real gamma-ray events, they usually have very few numbers of connected pixels so they can be easily separated with real events by a median filter or an area threshold (described in chapter 4).

Noise can also be generated in the image intensifier, which can be harder to remove from an image frame. The major source of noise in image intensifiers is the thermal generation of electrons that are emitted from the photocathode layer and amplified through the MCP, resulting in an apparent strong event or a cluster of bright pixels in a frame. These events have similar statistical properties to real gamma-ray events and are therefore hard to discriminate against. However, because the thermally emitted electrons have very limited lateral spread, the noise events may appear to have smaller area than real events, depending on the iQID configuration and the lateral spread of scintillation light. Chapter 4 introduces a new frame-parsing algorithm that is able to effectively eliminate the thermal noise events of a military surplus image intensifier based on the area extent of events as observed in the captured frames.

Another type of noise that is also hard to remove is the background noise originating from interactions between background radiation and the scintillator, which also appears as a cluster of bright pixels in the image frame. Background radiation exists everywhere and comes from different sources, such as cosmic radiation and naturally occurring radioactive materials like radon and radium. Thick, high-atomic-number shielding materials are typically used to surround gamma cameras in SPECT systems to reduce the amount of signal from background radiation. An energy window can also be applied to reduce background events, which, however, requires energy-resolution performance.

Finally, when an object is present in the FOV, Compton scattered gamma-rays in the object do not come from emission locations and do not have useful information, therefore defined as noise in the final image. A larger object means longer propagation paths for gamma-rays and thus a higher probability for Compton scattering. Compton scattered gamma-rays, when absorbed by the scintillation detector, can have very similar energy depositions as real events. High energy-resolution detectors are required to effectively discriminate between Compton scattered events and real events. In small-animal imaging, this type of noise, however, can typically be ignored because of the small path lengths through small animals.

A phosphorescence in scintillators like CsI(Tl) after exposure to room light may generate apparent background events for many hours, which can be misleading sometimes. Radiation sources like ^{57}Co may emit a small percentage of high-energy gamma-rays, which can easily penetrate the imaging aperture designed for lower-energy gamma-ray photons and cause higher background counts as well.

All of the above noise sources can be present in iQID cameras. To eliminate as many noise events as possible while keeping as many real events as possible, thus enhancing the S/N ratio and image contrast, an event estimation algorithm is required that ideally is able to identify real events and estimate their positions and energies with minimum error.

2.5.3 Event Estimation

MLE

For scintillation gamma cameras, Maximum-Likelihood Estimation (MLE) has been broadly used, which can provide asymptotically unbiased estimates of event position, energy and other parameters based on probability models of physical processes. [Barrett et al. 2009, Barrett and Myers 2004] If the parameters to be estimated are known as $\boldsymbol{\theta}$, based on assumptions of probability models of physical processes and noises, the probability density function (for continuous case) or the probability (for discrete case) as a function of the observed data $\mathbf{g}$ can be stated as $\mathrm{pr}(\mathbf{g}|\boldsymbol{\theta})$. However, in event estimation work, the observed data $\mathbf{g}$ is only an individual sample drawn from $\mathrm{pr}(\mathbf{g}|\boldsymbol{\theta})$ and the parameters $\boldsymbol{\theta}$ are unknown and to be estimated. So the likelihood of $\boldsymbol{\theta}$ given observed data $\mathbf{g}$ can be calculated as

$$L(\boldsymbol{\theta}|\mathbf{g}) = pr(\mathbf{g}|\boldsymbol{\theta}) \tag{2.13}$$

The MLE method is to search over all possible $\boldsymbol{\theta}$s and calculate the corresponding likelihood given the observed sample data $\mathbf{g}$ until an estimate $\widehat{\boldsymbol{\theta}}_{ML}$ is found that maximizes the likelihood, mathematically defined by

$$\widehat{\boldsymbol{\theta}}_{ML} \equiv \underset{\boldsymbol{\theta}}{argmax}\, pr(\mathbf{g}|\boldsymbol{\theta}) \tag{2.14}$$

Barrett developed a statistical analysis of CCD/CMOS-based gamma cameras in order to use the MLE method [Miller et al. 2009] and Miller implemented an MLE methodology on an EMCCD-based gamma camera under certain assumptions [Miller 2012b].

Frame Parsing

Although MLE is an asymptotically efficient and unbiased estimator if such an estimator exists, it requires accurate models for the physical processes involved in gamma-ray detection, which may not be easily achievable and accurate in real practice unless carefully calibrated. Moreover, since search is involved in finding the optimal estimated parameters, a large computational time relative to the frame rate can require off-line post-processing of the data, which can limit real-time visualization of the image. To compromise and develop a more practical solution that balances accuracy and speed, an in-line frame-parsing algorithm was developed for iQID cameras to identify gamma-ray events and estimate interaction parameters. [Miller et al. 2012a]

The original frame-parsing algorithm was implemented in GPUs with the following steps:

1. A raw image frame from the CCD/CMOS is acquired.
2. A median filter is applied to remove hot pixels.
3. An amplitude threshold is applied to remove thermal noise of the CCD/CMOS sensor.
4. A fast connected-components-labeling algorithm is used to identify connected clusters of pixels. [Suzuki et al. 2000]
5. Identified clusters of pixels are extracted and saved in a list-mode file.
6. The 2D or 3D interaction location and energy of each event are estimated, optimally with MLE method, but in practice with center-of-gravity estimation and pixel summation.

With the assistance of graphics processing units (GPU), multi-threaded parallel processing can be applied and real-time frame-parsing can be achieved for CCD/CMOS sensors running at high frame rates, for example a 640×480 CCD sensor with 200fps. The CCD noise can be effectively removed via the use of median filters and an amplitude threshold, with code running in the GPU. The image intensifier noise, however, is hard to eliminate with the original frame-parsing algorithm, which is fatal in some situations. For example, the XX1332 military surplus image intensifiers can provide reasonable gain with a large active area of 50mm diameter at low cost, making them good options for gamma cameras. However, some of them were found to generate centrally-located thermal-noise events, which caused artifacts in planar projection images and 3D reconstructed images. Chapter 4 introduces a more advanced frame-parsing algorithm that can effectively eliminate CCD/CMOS noise and image intensifier noise, while maintaining real-time processing speed that keeps up with the impressive incoming data rate of $>10^7$ pixels/second.

CHAPTER 3

ENERGY RESOLUTION OF IQID

Having introduced the advantages of iQID scintillation cameras in gamma-ray imaging, we now focus on solving a major limitation of iQID cameras which is the typically poor energy resolution. Energy resolution in a gamma camera is a very important performance metric as introduced in chapter 1. Good energy resolution can be used to precisely identify real gamma-ray interaction events with full energy deposition as determined by photoelectric absorption, which is important in applications such as multi-isotope imaging and can be also used to eliminate some background noise and Compton scattered noise in the final image as discussed in chapter 2. iQID cameras were found to suffer from poor energy resolution because of the use of MCPs in image intensifiers as the main signal-amplification devices. This chapter presents a study of the energy resolution of iQID that investigated the physics of the MCP as the main electron amplification component of image intensifier, revealing the origin of energy resolution degradation via Monte Carlo simulations. We end by proposing different solutions in the form of alternative gain devices.

3.1 Introduction

Not long after the original iQID gamma camera was developed, its energy resolution performance was evaluated. [Miller 2012b] If the energy resolution is defined by the ratio of FWHM to the mean of the detected photon energy distribution as

$$ER = \frac{FWHM}{Mean} \ , \tag{3.1}$$

the energy resolution of iQID tested with different radioisotopes was shown to be greater than 50%, as shown in Figure 3.1.

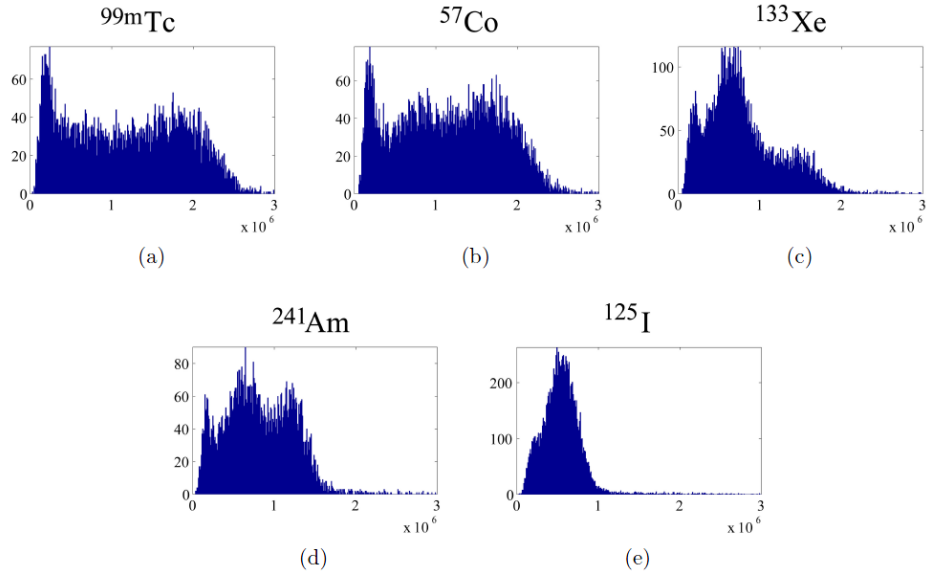

Figure 3.1 [Miller 2012b]: The estimated energy distribution of different radioisotopes using iQID scintillation camera.

The reasons for poor energy resolution may include the depth of interaction (DOI) effect and attenuation (scattering and absorption) inside the scintillator, the Poisson statistics of photo-electric interactions, image intensifier gain variations, and use of a suboptimal photon-energy-estimation algorithm. The DOI effect and the attenuation effect can be improved by using thin scintillators. The effect of Poisson statistics can be improved by using high light-output scintillator materials. The effect of the estimation algorithm can be minimized by implementing the maximum-likelihood estimator [Barrett et al. 2009]. However, the image intensifier gain variation, a dominating factor, still remains an unsolved problem as a result of randomness in the intrinsic physical process.

If we denote the mean number of photoelectrons generated in a small region corresponding to pixel m of the CCD/CMOS sensor as $\bar{n}_m(x, y, z, \mathcal{E})$, which is defined in equation (2.11), and the average gain provided by the combination of image intensifier, relay lens and CCD/CMOS sensor as $\bar{G}$, the average signal in pixel m can be denoted as

$$\bar{g}_m(x, y, z, \mathcal{E}) = \bar{G}\bar{n}_m(x, y, z, \mathcal{E}) \tag{3.2}$$

the variance of which can be derived to be

$$Var(g_m|x,y,z,\mathcal{E}) = \bar{n}_m(x,y,z,\mathcal{E})[Var(G) + \bar{G}^2] + \sigma^2 \,, \tag{3.3}$$

where $Var(G)$ is the variance of G or approximately the variance of the image intensifier gain, and σ^2 is the variance of CCD/CMOS readout noise that is negligible when an image intensifier is present. [Appendix by Barrett in Miller et al. 2009] The energy resolution (ER), based on the previous definition, can be denoted as

$$ER \propto \frac{\sqrt{Var(g_m)}}{\bar{g}_m} = \sqrt{\frac{1}{\bar{n}_m(x,y,z,\mathcal{E})}\left[\frac{Var(G)}{\bar{G}^2} + 1\right] + \frac{\sigma^2}{\bar{G}^2 \bar{n}_m{}^2}} \tag{3.4}$$

We can see that mathematically the energy resolution of iQID cameras is also affected by the gain variation of image intensifier.

As introduced in chapter 2, the micro-channel plate (MCP) is the key component in image intensifiers that is responsible for electron amplification, meaning that the MCP might be the factor limiting the energy resolution performance of iQID cameras. To study the origins and effects of MCP gain variations, we investigated the physics of MCPs.

3.2 Physics of the Micro-Channel Plate

A micro-channel plate is composed of many miniature electron multipliers parallel to each other as shown in Figure 3.2. It's made by etching away fiber cores from a fiber-optic faceplate in which the rod is made from leaded glass. There are about one million separate channels in one square centimeter. Each channel works as a continuous dynode and has a diameter of 5-15 um and length-to-diameter ratios between 40 and 80. Typical channel center-to-center spacing is 15um. Channel orientation is typically 8 degrees (bias angle) relative to the entrance-surface normal to facilitate interactions between incident photoelectrons (PEs) and channel walls. A potential difference, also called the bias voltage, of several-hundred to one-thousand volts is placed across the channels, which have tota1 resistance about 100-1000MΩ. When a single photoelectron gets into the channel and penetrates into the channel wall, it deposits its energy along the way and produces several secondary electrons (SEs). These SEs get accelerated by the electric field produced by the bias voltage and again hit the wall to produce even more SEs. This process repeats resulting in a cascade of SE emissions. Finally, a SE cloud exits the channel with a gain of 10^3-10^7 (the upper part of this range is reached by stacking two MCPs). In addition to high gain,

micro-channel plates also have ultra-high timing resolution (<100ps) and high spatial resolution, mainly determined by channel diameter and center-to-center spacing.

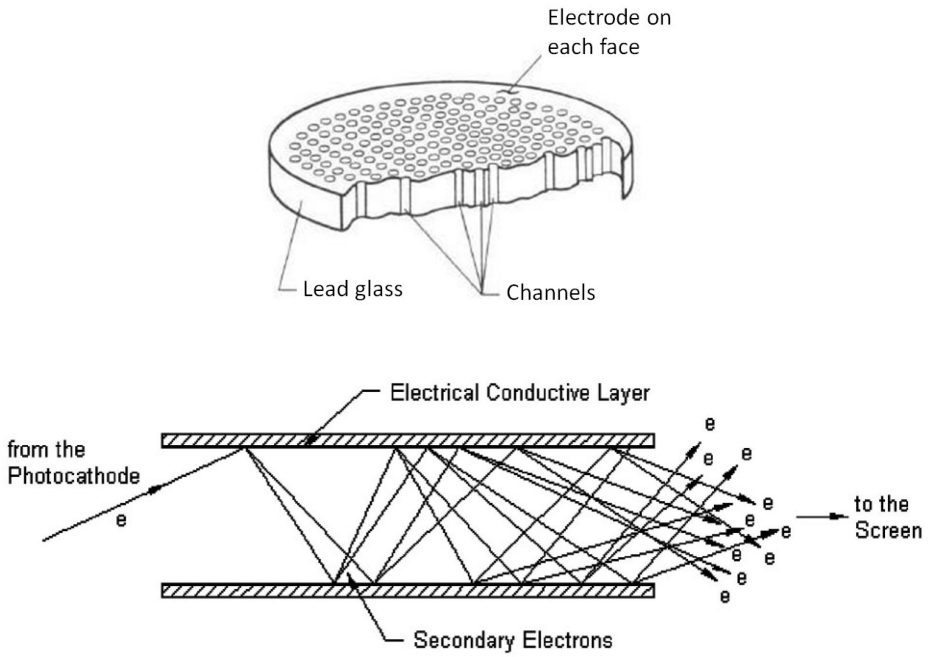

Figure 3.2: The micro-channel plate (Top) [Wiza 1979] and electron amplification process in a single channel (Bottom) [Proxivision].

To understand the whole electron-multiplication process, we need to first understand the physics involved in secondary-electron emission, including the yield, energy distribution, and emission-angle distribution of SEs, electron reflections and other physical processes.

3.2.1 Secondary Electron Yield

The SE yield directly depends on the primary-photoelectron (PE) energy and incident angle. When a primary PE strikes the channel wall in the surface normal direction, as the primary energy increases, initially the yield also increases because more energy is deposited in the wall material, and since the primary electron doesn't penetrate too deep inside, most of SEs are within the escape depth and can exit the wall into the channel. As the primary energy keeps increasing, however, the yield decreases because the primary electron penetrates too deep inside the wall so that most SEs lose all of their energy in diffusing to the surface, and fewer SEs make it into the channel.

If the primary energy is fixed, as the primary incident angle increases relative to the wall surface normal, the distance between the location of generation and the surface is decreased so that more SEs will have enough energy to make it to the channel and thus the yield increases. As a result of this balance between depth and energy deposition, larger energy PEs tend to generate more SEs as incident angle increases. Experiments have been performed that demonstrate the dependence of SE yield on PE energy and angle. [Hill 1976] Figure 3.3 demonstrates the effects of interaction depth and incident angle on SE yield. Figure 3.4 shows the experimental results demonstrating the relationships between SE yield and PE energy and angle of incidence.

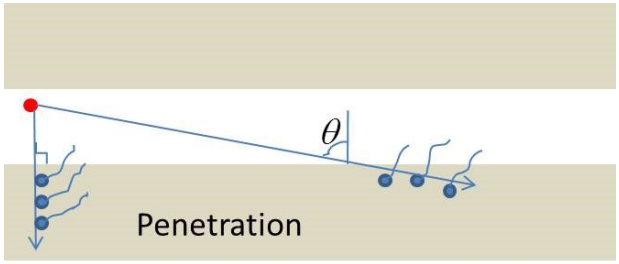

Figure 3.3: Demonstration of the effects of penetration angle and depth on SE yield.

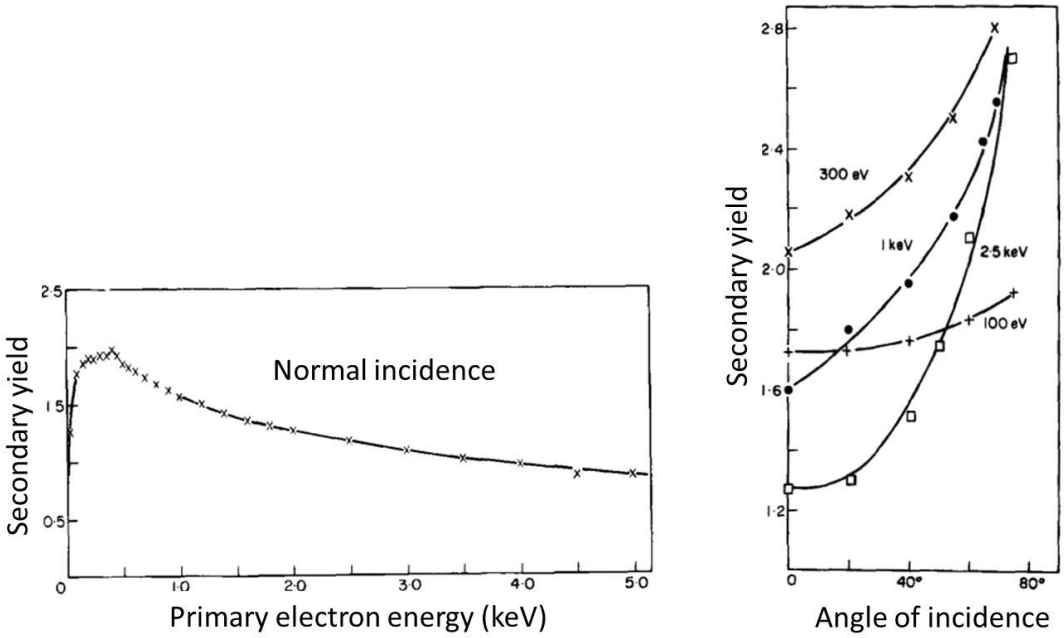

Figure 3.4 [Hill 1976]: Relationships between SE yield and PE energy (Left) and angle of incidence (Right).

To be able to predict SE yield with a mathematical formula, a semi-empirical model of SE yield based on the elementary theory of secondary-electron emission [Salow 1940, Bruining 1954] has been developed [Hill 1976], which has been applied to the study of MCPs [Price and Fraser 2001]. Although this model describes SE-yield physics, it requires many parameters to be experimentally determined that are not convenient for simulation purpose. So in this work, a model proposed by [Furman and Pivi, 2002] and applied by [Wu et al. 2008] is used that also predicts the SE-yield performance but does not require many parameters to be measured. According to the model, SE yield as a function of PE energy and incident angle is given by

$$\delta(E,\theta) = \delta_{\max}(\theta)\frac{s\dfrac{E}{E_{\max}(\theta)}}{s-1+\left(\dfrac{E}{E_{\max}(\theta)}\right)^{s}} \ , \tag{3.5}$$

where δ is the mean SE yield, E is the PE energy, θ is the primary incident angle, s is an adjustable material-dependent parameter (a typical value of 1.3 was used here [Wu et al. 2008]), $\delta_{\max}$ is the maximum possible yield for a given angle θ and is given by (3.6).

$$\delta_{\max}(\theta) = \delta_{\max}(0)\exp[\alpha(1-\cos\theta)] \ , \tag{3.6}$$

where $\delta_{\max}(0)$ is the maximum yield for normal incident PE which basically ranges from ~3.0 to 4.0 and a value of 4.0 is used in this work. α is a material-dependent parameter whose value ranges from 0.4 to 0.6 that determines the variation of the maximum yield with incident angle [Authinarayanan and Dudding, 1976], and a value of 0.5 was used. $E_{\max}$ is the corresponding primary energy that gives the maximum yield for angle θ and is given by (3.7).

$$E_{\max}(\theta) = \frac{E_{\max}(0)}{\sqrt{\cos\theta}} \ , \tag{3.7}$$

where $E_{\max}(0)$ is the primary energy that gives maximum yield at normal incidence whose typical value varies between 200-300eV [Authinarayanan and Dudding, 1976]. A value of 260eV was chosen for this work, which was reported to be a good fit with experimental data. [Wu et al. 2008]

After we calculate the mean number of SE yield, assuming Poisson statistics, the actual number of SE yield is randomly sampled from a Poisson distribution with the calculated mean.

3.2.2 Secondary Electron Emission Energy

Since most SEs lose lots of energy in the process of diffusing to the channel-wall surface and overcoming the surface potential, they usually have low kinetic energies when they are emitted into the channel. Hill [1976] proposed an energy distribution for SEs and the most probable energy is about 3.0 eV. Price and Fraser [2001] used an empirical formula given by Petrovna and Flegontov [1988] to describe the SE energy distribution. Wu et al. [2008] utilized the Maxwell-Boltzmann probability distribution for modeling the SE energy distribution that is a similar and simplified version of the empirical formula, and was used in this work as given by

$$p(E_{SE}) = C\frac{E_{SE}}{E_0}\exp(-\frac{E_{SE}}{E_0}), \tag{3.8}$$

where $p(E_{SE})$ is the probability for a SE to have energy of E_{SE}, C is a normalization constant, and E_0 is the most probable energy for SEs, whose value is taken to be 3.0 eV as proposed by Hill [1976].

The real value for the SE energy is randomly sampled from the above distribution. A conservation-of-energy principle also applies to the emission of SEs. That is, the total energy assigned to all SEs generated by one primary electron is smaller than the primary electron's energy. SEs will, of course, be accelerated by the electric field in the channel, thus their energies E_{SE} will increase and work as primary electron energies E for the next step in the collision cascade.

3.2.3 Secondary Electron Emission Angle

The angle of SE emission relative to the wall surface normal follows a normalized cosine probability density distribution as shown in equation (3.9), which is widely used by many other researchers in the study of SE emission and is supported by Monte Carlo simulations of SE emission process performed by Kawata et al. [1992, 1997]:

$$p(\theta) = 0.5\cos(\theta)\,. \tag{3.9}$$

Physically this distribution also makes sense, because to exit at a large angle, an SE needs to travel a longer distance from its generation site to the surface, leading to less probability of occurrence.

3.2.4 Electron Reflection

When the primary energy is very large, the primary electron has a high probability of penetrating into the wall material and creating secondary electron emissions. These SEs will be accelerated by the potential difference across the channel and work as primary electrons for next collisions. However, since these primary electrons have different emission angles and energies, some of them may not acquire enough energy from the electric field before their next collision and will therefore be elastically reflected by the channel wall instead of producing SEs. This process is called the SE reflection or elastic scatting. The probability for this process to happen only depends on primary energy E [Scholtz et al. 1996] and is expressed as

$$p_{ref}(E) = \exp[1.59 + 3.75\ln E - 1.37(\ln E)^2 + 0.12(\ln E)^3]/100\ . \tag{3.10}$$

When reflection happens, the kinetic energy of the SE will not change but the direction of velocity will according to principle of reflection.

3.2.5 Other Physical Effects

The physical effects described and modeled above are dominant when the gain is small and are important for our main purpose which is to study the gain variation under unsaturated channel condition. However, other physical effects can become dominant when the gain is very large, which may cause channel saturation.

In the case of a straight channel, when the gain increases, the probability of producing positive ions by electron collisions with both residual gas molecules and gas molecules desorbed from the channel wall is increased. These ions usually are produced in high space-charge-density regions close to the output of the channel and can drift back to the channel input to produce SEs, resulting in a regenerative feedback effect and gain saturation. This

effect is called ion feedback. Bending or twisting the channels and maintaining a strict vacuum environment can be used to avoid this effect.

As mentioned earlier, channels have ohmic resistances of about 100-1000MΩ which is relatively uniformly distributed down the channel, so the current available to be transformed to SE space current is limited. When the gain is very high, space charge will deplete the wall current, thus reducing the electric field in the channel which in turn reduces SE yield. As a result, gain is saturated. The gain in this steady state has been calculated by Harris [1971].

Finally another possible cause of saturation is called the space-charge effect. According to Wiza [1979], "at high enough gains, the space charge density at the rear of the channel reduces the 'kinetic energy' of electrons as they interact with the channel walls until the secondary electron yield is reduced to unity." Others have also discussed this effect in the past. [Adams and Manley 1966, Schmidt and Hendee 1966, Bryant and Johnstone 1965]

3.3 Monte Carlo Simulation

To simulate the performances of an image intensifier, the MCP is placed between a photocathode (S25) and a phosphor screen (P43). When Poisson-distributed scintillation light is generated by a gamma-ray interaction and detected by the image intensifier, the photocathode will produce a random number of PEs sampled from a Poisson distribution of which the mean corresponds to the average number of scintillation photons times the quantum efficiency of the photocathode. These PEs will start with very low energy and then be accelerated by a potential difference of 200-300V placed between the photocathode and the MCP. With 200-300 eV energy, these PEs enter the MCP channels, strike the channel walls and initiate the electron-cascade process. A Monte Carlo simulation can then be applied to simulate the electron amplification process inside the MCP channels.

This Monte Carlo simulation is based on a 2D model of the MCP channel, assumes nonrelativistic electron motion, and neglects correlation between electrons and any cross-talk effects between adjacent channels, such that each channel works independently. The SE yield, SE energy, emission angle and electron reflection are considered in this simulation. The other physical effects that cause saturated channels are not included. In other words, the simulation assumes unsaturated channels. Also only a single channel is simulated because as

long as the channels are working in unsaturated mode and correlation between electrons are negligible, the difference between PEs entering multiple channels and a single channel is just a problem of initial conditions which is not an intrinsic property of the MCP, but instead dependent on the input light signal.

The default simulation parameters are listed below in Table 3.1, unless later analyses required certain parameters to be changed, which will be clearly stated. The simulation was implemented in LabVIEW as shown in Figure 3.5. Although LabVIEW can be slower than compiled languages in processing speed, it offers a graphic user-friendly interface (GUI) that can be easily used by others for future applications.

PE energy	Bias angle	Channel diameter (D)	Channel length (L)	Bias voltage (U)
200 eV	8^{o}	6 um	300 um	1000 V

Table 3.1: Default parameters used in the simulation.

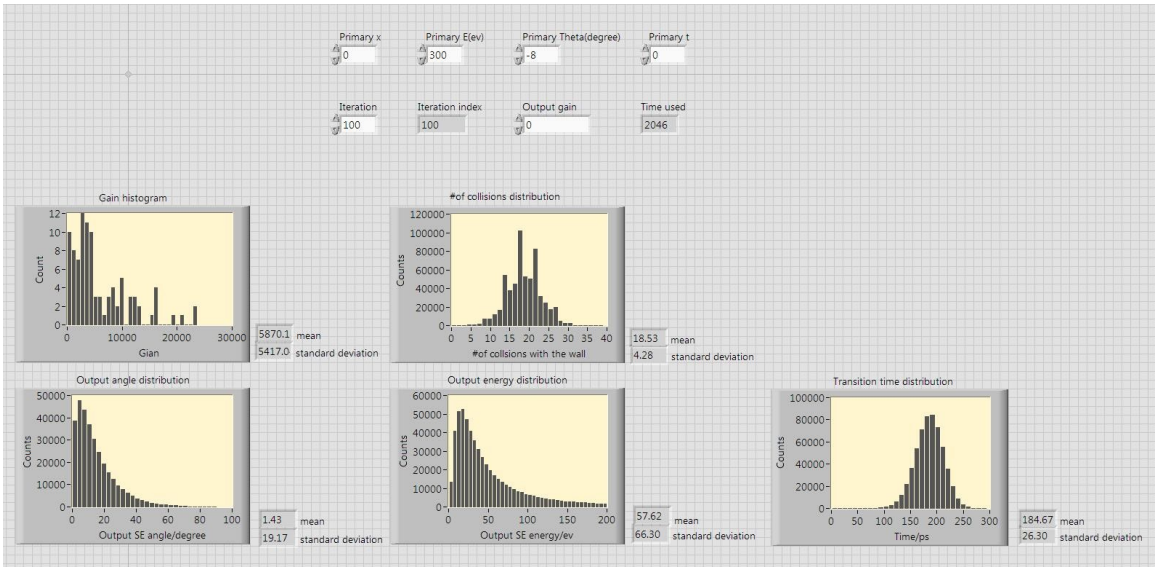

Figure 3.5: LabVIEW interface of the Monte Carlo simulation of MCP gain process.

The simulation started with one PE, calculated how many SEs were generated upon the first collision, assigned energies and emission angles to each SE, traced their paths until their next collisions and finally collected SEs coming out of the channel, including the trajectory information they carried. The number of incident PEs determined how many iterations of the above simulation were performed. Three kinds of simulation-based studies were performed in this work. One study was to analyze timing resolution, output-electron-cloud angular and energy distribution, and number-of-collisions distribution, all of which are basic MCP properties, based on a fixed number of incident PEs. Another study was to analyze MCP gain variations as a function of channel geometry and voltage supply, again based on a fixed number of incident PEs. Finally the effect of gain variations on the energy resolution of the image intensifier was analyzed, based on varying the number of PEs but leaving other system parameters fixed. This was also the main purpose of the simulation.

3.4 Results and Analysis

3.4.1 MCP Basic Properties Study

To study the basic properties of the MCP, a total of 10 PEs were incident into one channel. After the electron cascade process, about 60,000 SEs were produced at the exit face of the channel. All trajectory information including the number of collisions undergone, the transition time used, the energy and emission angle of each SE at the exit face were recorded and the corresponding histograms were generated for statistical analysis as shown in Figure 3.6.

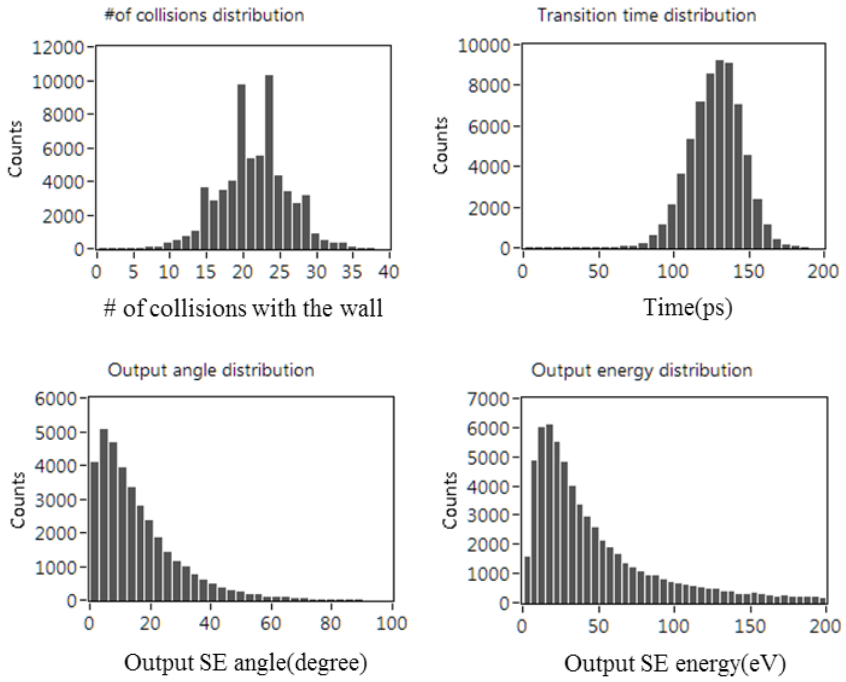

Figure 3.6: Simulation results based on 10 incident PEs. Number of collisions distribution (top left); Transition time distribution (top right); Output SEs energy distribution at the exit face of MCP channel (lower left); Output SEs emission angle (relative to wall surface) distribution also at the exit face (lower right).

From these distributions, we observed that most SEs undergo between 15 to 28 collisions with the channel wall. Broad distributions for the number of collisions will contribute to large gain variation, affecting energy resolution. However, this is not the only factor influencing gain variation, as will be discussed later. The average transition time was about 128ps, which is very fast. Also, the FWHM of the transition-time distribution or timing resolution is about 40ps, which is consistent with commonly known values (<100ps). [Young et al. 1986] This also validates the simulations in some sense. From the output SE energy distribution, we found the peak energy to be about 15-20 eV, and the trend of this distribution is similar to the exponential distribution of SE emission energy as described in the MCP physics section, because output SEs are simply accelerated versions of newly generated SEs. Finally, the angular distribution was generated only for output SEs generated from one side of the channel wall, as the output SEs generated on the other side of wall will have similar distribution but with opposite emission angles. Also, the angle is relative to the wall surface propagation direction instead of the surface normal. Here, a most probable

angle of about 5 degrees was observed and the probability was small for output angles greater than 30 degrees. That means most output SEs are emitted along the channel surface. In the context of an image intensifier, there will be another potential difference placed between exit face of the MCP channel and a phosphor screen used to collect these SEs. As a result, a strong electric field is generated that will further collimate these SEs, so that the angular distribution is greatly compressed, reducing the effect of angular spread of output SEs on final spatial resolution.

These distributions characterize different MCP properties and are sensitive to system parameters like channel diameter and length, and bias voltage. These are useful results produced by this analysis, which can be used to verify the accuracy of the simulation.

3.4.2 Gain Performance Study

To find out how the gain spectrum varies with system parameters, a fixed number of 10 PEs was used and 1000 iterations were performed. By varying the MCP channel diameter D, the channel length L and the bias voltage U, several gain distributions were generated for comparison with a reference distribution (a) as shown in Figure 3.7. Also, average gain and energy resolution were calculated for each distribution.

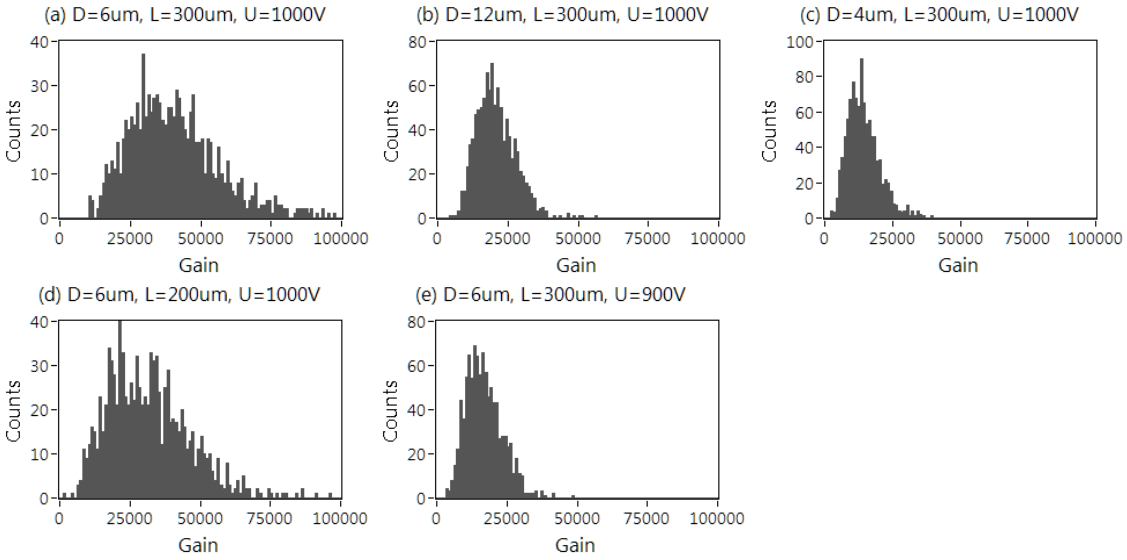

Figure 3.7: Gain spectrum under different system parameters. (a) Reference gain spectrum with channel diameter D=6um, channel length L=300um, bias voltage U=1000V, mean=40507, energy resolution ER=94.1%; (b) Larger diameter D=12um channel with other parameters same as the reference ones, mean=20543, ER=79.0%; (c) Smaller diameter

D=4um channel, mean=14249, ER=97.8%; (d) Shorter channel length L=200um, mean=31548, ER=108.5%; (e) Decreased bias voltage U=900 V, mean=16785, ER=90.6%.

A simple mathematical model used to calculate the gain of MCP was proposed by Eberhardt [1979] under a series of assumptions and approximations. This model simulated the gain mechanism as the product of primary PE effective gain, and a number of gains corresponding to each following collision as

$$G = \delta_{PE}\delta^{n-1} \ , \tag{3.11}$$

where G is the total gain, δ_{PE} is the effective gain of primary PE, δ is the effective gain of subsequent collisions, and n is the total number of collisions or amplification stages. With the help of this equation, we can understand the results shown in Figure 3.7, and reach the following conclusions: both too-large and too-small channel diameters will lead to decreased gain because either the number of amplification stages n is too small due to a large diameter, or the effective yield for each stage is too small due to a short acceleration distance. This may be seen by comparing Figure 3.7 (a) with (b)(c). Thus an optimal channel diameter exists that maximizes gain. Decreasing the channel length directly decreases the number of amplification stages, which results in less gain, a result shown in Figure 3.7 (a) and (d). Gain is also very sensitive to a change of bias voltage, which affects yield of each stage. A small decrease in voltage leads to a large drop of gain comparing Figure 3.7 (a) and (e).

The energy resolution, which describes the gain variation relative to average gain, is almost insensitive to these system parameters, as shown in Figure 3.7. Factors contributing to gain variation include δ and n, both of which are random and have a large range of possible values around some mean, as shown in the MCP's basic properties and Figure 3.6. Unfortunately, the mean and range of δ and n always change together. When system parameters are adjusted to increase δ and n, their ranges also increase; when system parameters are adjusted to decrease δ and n, their ranges decrease accordingly. This is why ER changes little when we change different system parameters.

3.4.3 Energy Resolution Study

Having analyzed gain performance of the MCP alone, we can put the MCP in the structure of the image intensifier and study the effect of the gain variation on the energy resolution of the image intensifier, which is also the key component of iQID cameras. In the image intensifier, PEs are generated by the photocathode and the number of PEs follows Poisson distribution with mean corresponding to the average number of incident scintillation light photons times the quantum efficiency. Because of Poisson statistics added into MCP gain statistics, the energy resolution of the image intensifier will be larger than a single MCP as shown in Figure 3.8.

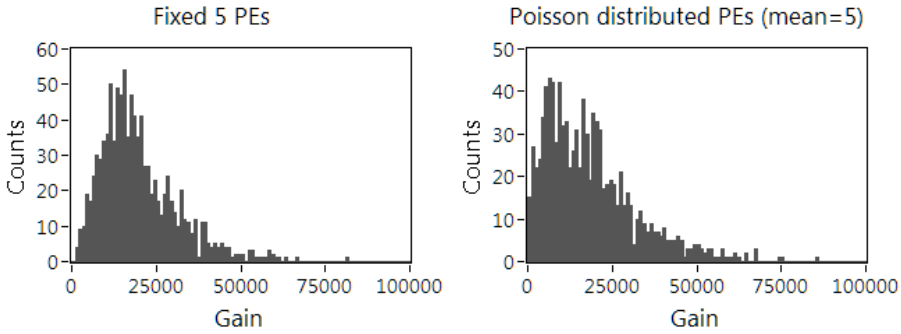

Figure 3.8: Two histograms showing ER difference for a single MCP with 5 PEs (Left, ER=135.8%) and the same MCP in the context of image intensifier with mean number of 5 PEs (Right, ER=181.7%). System parameters are the same as in Table 3.1, which is also a similar configuration as a real image intensifier used in later experiment.

The ER in (a) in Figure 3.7 is better than that of the left spectrum in Figure 3.8, both of which are computed using exactly the same system parameters, only with different number of PEs. The reason is because overall MCP gain statistics can be viewed as the sum of N independent identical distributions each corresponding to a single PE, where N is the number of PEs. As N increases, MCP gain statistics approach a Gaussian distribution according to the central-limit theorem. Thus the ER will also improve as N increases. A similar analysis can be made for a Poisson distributed number of PEs in the image intensifier, which approximate Gaussian distribution as the mean number of PEs M increases. So the energy-resolution performance should be better with more PEs (larger N or M). A simulation was performed to investigate the relation between ER and the mean number of PEs (N and M), with results as shown in Figure 3.9.

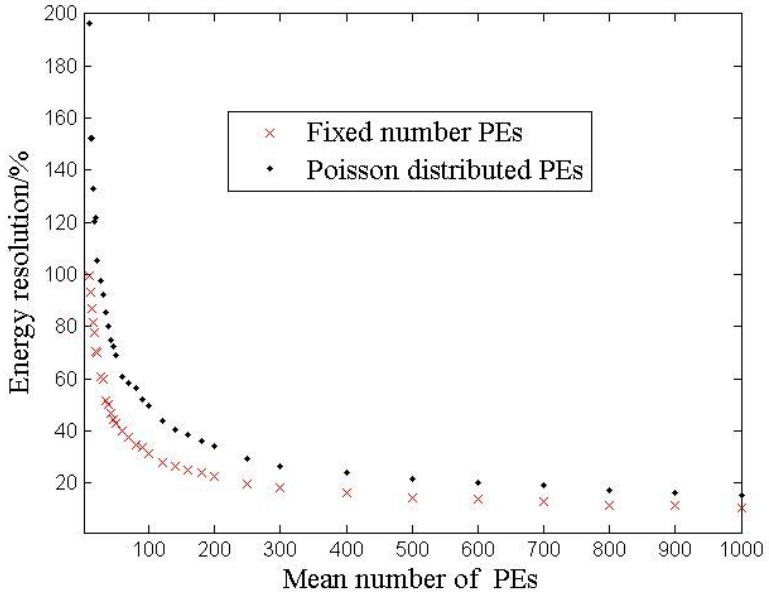

Figure 3.9: Relationship between ER and mean number of PEs. Both the MCP situation with a fixed number of PEs and an image intensifier situation with a Poisson distributed number of PEs are simulated. ER of ~10% can be achieved for a single MCP with 1000 fixed number of PEs and ~15% can be achieved for image intensifier with an average of 1000 PEs.

From Figure 3.9, we see that the energy resolution of an image intensifier can be improved by increasing the incident scintillation light signal or number of PEs. For any given energy resolution, we can estimate the mean number of PEs needed in the photocathode using this curve. Due to the large gain variation of the MCP in combination with the Poisson statistics on the number of PEs, about 800 mean PEs are required to improve ER to below 20%. Since the photocathode quantum efficiency is typically around .25, this would require around 3000 scintillation light photons, which is more than the total number generated by most common single-photon-emitters at gamma-ray energies.

3.5 Experimental Validation

A preliminary experiment aimed to validate and correlate the simulation results was performed using a ^{57}Co (122keV) gamma-ray source and an iQID detector with a 400 um-thick columnar CsI(Tl) scintillator, and a single-MCP image intensifier manufactured by [Proxivision]. An opaque entrance window was applied to the scintillator. The MCP bias voltage was adjustable in the range of 400-900V, controlled by an external DC power supply made by B&K Precision Corporation [BK precision]. The iQID camera was set in photon-

counting mode. By adjusting the distance between the radiation source and the photocathode input surface, zero or very few overlapping events appeared in each frame, which facilitated event identification in post processing. After raw images with events were acquired, a series of processing steps was performed to extract the 122keV event clusters in the image (chapter 4 provides details about the frame-parsing algorithm). Then by simply summing up the pixel values of each event cluster as an estimate of the energy, a spectrum was generated and the energy resolution of the whole system was estimated. Although MLE may be a superior method for estimating event energy when it correlates with depth, when a thin 400um scintillator is used the variation of gamma-ray interaction depth is small such that pixel-summing is reasonably used as an alternative method.

Since the simulation was implemented under the assumption of unsaturated channels, bias voltage in the experiment was adjusted to avoid saturation effects while at the same time keeping the gain as high as possible to maximize the S/N ratio. The event-extracting-algorithm parameters were also adjusted to eliminate most background events while retaining as many real events as possible. Energy spectra for three bias voltages were generated and are shown in Figure 3.10.

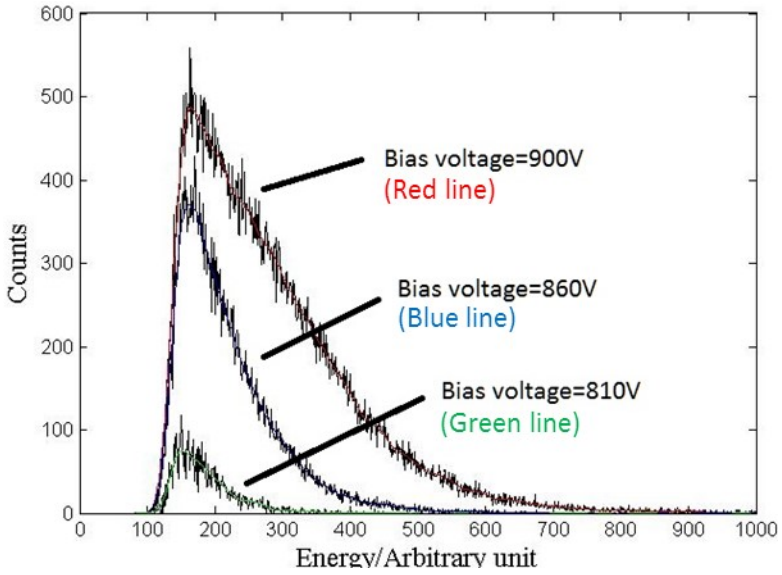

Figure 3.10: Energy spectra of iQID detector for three different bias voltages. Black lines are experimental results; red, blue and green lines are fitted curves used to estimate energy resolution. ER=115.9%, 65.1%, 50.1% for red, blue and green curves.

Because this experiment was performed with low-gain configurations, with a single-MCP image intensifier and a low applied voltage, the SNR appeared to be low. To separate the limited number of real events from an overwhelming background, thresholding introduced truncation effects in the resulting energy spectra as shown in Figure 3.10 and the less gain, the more severe the truncation effects will be. For example, the lowest-bias-voltage curve will suffer from truncation effects the most among the three fitted spectra, and only a small portion of real events are collected. Channel saturation is obvious in the high-bias line from its expanded shape. The reason for saturation to occur is that iQID has very good spatial resolution, which means incident photons stay together, increasing the number of PEs entering each channel, and finally causing channel saturation in some channels. The larger the bias voltage, the more gain there will be and the more saturation effects are likely. In sum, it's hard to satisfy a condition of not saturating while at the same time avoiding truncation based on the iQID gain configuration. The intermediate curve in Figure 3.10 was found to have a good balance between saturation and truncation and yielded the best achievable estimate of the system energy resolution.

Although the scintillator, opaque entrance window, event-energy-estimation algorithm and Compton scattering all affect energy resolution, their effects were found to be secondary to that of the image intensifier, which has great signal amplifying power but dominates total energy resolution of the system as found above. If we assume ~65% as the ER of the image intensifier and refer to Figure 3.9, we deduce that approximately 50 PEs were generated by the photocathode. Considering that the photocathode (S25) has a QE of about 9% at 550nm (peak emission wavelength of CsI:Tl scintillator), the fiber optics faceplate coupled with photocathode has a NA of 0.58 and opaque entrance absorbs half of total photons, we can calculate there are about 6000 photons generated in the scintillator. According to the literature, CsI(Tl) scintillator has light yield of about 54 photons/keV, which means there will be an average of 6588 photons generated for each 122keV gamma-ray photon interaction. The two results agree, which suggests that the simulation results are reliable as long as we work in unsaturated mode. Then Figure 3.9 can be used to calculate approximately how many PEs are generated in the image intensifier for different experiments.

3.6 Proposed Improvements

From the previous simulation results and analysis, we conclude that there is a high variance in the electron-multiplication process. Starting from Poisson distributed PEs, the yield of SEs, the SE energies, and emission angles are all randomly varying following their own distributions. However, comparison with PMTs, which have similar electron multiplying mechanisms with much better energy resolution, reveals that the randomness in the number of collisions of SEs or electron-multiplication stages is playing the key role in the energy resolution performance. Instead of a fixed number of dynode structures that create a fixed number of gain stages in PMTs, each channel in an MCP works as a continuous dynode unit that provides a varying number of gain stages, causing sufficient variability to degrade the energy-resolution performance.

One possible solution to improve energy resolution of iQID cameras is to invent new electro-optical devices for optical amplification. To maintain high-spatial-resolution performance while improving energy resolution, the device ideally should take advantage of both image intensifier and PMT properties. Currently, three out of four combinations based on continuous or discrete dynode for electron amplification and anode or phosphor screen for electron signals readout have been realized in different electro-optical amplification devices (PMTs, image intensifiers and MCP assemblies). For example, MCP assemblies can be manufactured with MCPs and multiple readout anodes that features ultra-high timing resolution for time-of-flight mass spectroscopy applications. The most useful combination has not been demonstrated, which would combine a high-energy-resolution discrete dynode structure such as the mesh-dynode used in MA-PMTs and high-spatial-resolution phosphor screens as used in image intensifiers. This combination, when applied in electro-optical devices, would serve as an alternative photon-amplifier and provide both high spatial resolution and energy resolution performance. Figure 3.11 depicts the four combinations and the potential solution for improving poor energy resolution in iQID cameras.

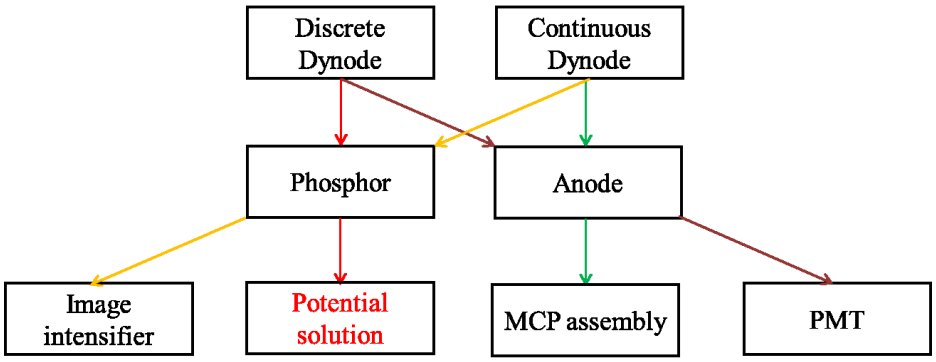

Figure 3.11: Different combinations of dynode and electron readout used in current photon amplifying devices and the potential solution for improving energy resolution of iQID camera.

Another possible solution is to add another high-energy-resolution photodetector to the other side of the scintillator. Columnar CsI(Tl) scintillators fabricated on a fiber-optic substrates are a good option for this purpose. Figure 3.12 shows a demonstration of this concept with SiPM photodetectors. A similar concept has been used by others in exploring a prototype PET system. [Park et al. 2012, 2014] With this configuration, high spatial resolution can be provided by the image intensifier while high energy resolution and timing resolution are provided by the extra photodetectors. High-frame-rate CMOS sensors ideally should be used to create correspondence with other photodetectors in identifying gamma-ray events, but the problem of temporal registration of events between different detector technologies is not trivial.

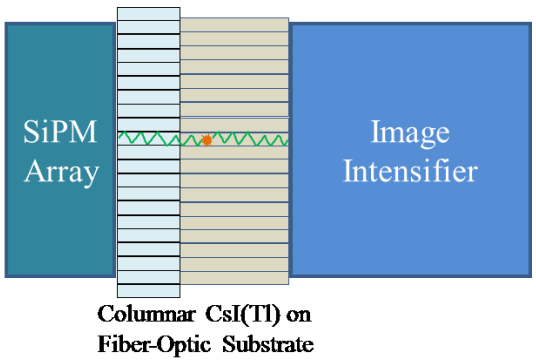

Figure 3.12: Graphic representation of the SiPM-coupled iQID camera to improve energy resolution and timing resolution performance while maintaining high spatial resolution.

Finally, based on the Monte Carlo simulations, we conclude that the energy resolution of image intensifiers can be effectively improved by increasing the mean number of PEs. Therefore, higher gamma-ray energy, high-yield and high-transport-efficiency scintillators,

large-numerical-aperture (NA) fiber-optic faceplates, and high-quantum-efficiency photocathodes can all help improve the energy resolution of iQID cameras.

3.7 Conclusions

In this section, we have introduced the micro-channel plate and the key physical effects occurring in electron multiplication inside each channel. Based on these effects, a 2D Monte Carlo simulation was implemented under non-saturation assumptions with respect to channel properties, gain, and energy-resolution performance. The MCP's basic properties modeled by this simulation match well with observed and published data. Simulation results showed that MCP gain will be affected by system parameters; however the large gain variation or poor energy resolution is almost insensitive to these parameters. It is the large variation in the number of amplifying collisions and yield per stage that dominate the gain statistics. By comparison, a PMT usually has a fixed number of amplifying stages and a smaller range of SE yields per stage, which provides much better energy resolution. Further exploration of gain statistics showed that energy resolution could be improved by increasing the number of photons. A curve was generated that relates image-intensifier-energy resolution to mean number of PEs. From this curve, we see it's possible to improve energy resolution to better than 20% when more than 800 PEs are generated. Large QE photocathodes, high light output scintillators, and large NA fiber optic faceplate will all help increase the number of PEs. However, caution is required because the MCP might become saturated when the number of PEs is too large.

In order to acquire more experimental results to accurately correlate with this simulation, careful revisions to the experimental setup are needed, including the use of appropriate sources, thinner columnar scintillator to reduce depth of interaction, low-noise CCD/CMOS sensors, and optimal MLE methods for more accurate event parameter estimation. Also, channel saturation effects can be further studied if necessary to get a complete picture of MCP behavior. Finally, based on the results from this study, a new design of an MCP structure with discrete dynode stages is needed to achieve better intrinsic energy resolution as well as high gain, excellent spatial and temporal resolution, thus facilitating a next generation iQID camera.

CHAPTER 4

ADVANCES IN FASTSPECT III

iQID cameras, which have an order of magnitude higher spatial resolution than the general PMT-based gamma cameras, have been used to develop a high-resolution preclinical stationary SPECT system known as FastSPECT III. With 20 iQID cameras, FastSPECT III was originally developed for rodent brain imaging and was shown to provide an isotropic linear resolution of ~250 microns. [Miller et al. 2010] Although a micro-resolution phantom was successfully reconstructed in the preliminary evaluation using a GPU-enabled maximum-likelihood expectation-maximization (MLEM) algorithm, several issues were found in both iQID cameras and the FastSPECT III system configuration that limited successful reconstruction of animal images. In this chapter, advances that have addressed the limitations of FastSPECT III will be introduced. Finally, with the advances in the FastSPECT III system, both resolution phantom and mouse images have been successfully reconstructed with better than 350-micron linear spatial resolution, and sample images will be presented at the end of this chapter.

4.1 Introduction

FastSPECT (Four-dimensional Arizona STationary Single-Photon Emission Computed Tomography) is a stationary SPECT imaging approach developed at the University of Arizona and in the Center for Gamma-Ray Imaging (CGRI) that uses rings of modular gamma cameras to acquire 2D planar projection images in parallel with sufficient angular sampling such that a 3D subject can be accurately reconstructed. The first FastSPECT system, FastSPECT I, was designed for human brain imaging [Rowe et al. 1993] and converted later to small-animal imaging [Klein et al. 1995, Kastis 2002] with two rings of 13 and 11 modular PMT-based scintillation cameras, respectively. For each gamma camera, a 10 cm × 10 cm × 0.5 cm NaI(Tl) scintillator is coupled to a 2×2 array of square 2”×2” PMTs via a 1.9 cm-thick light guide. The second FastSPECT system, called FastSPECT II and enabled by the advances in detectors and read-out electronics, was constructed with 16 modular scintillation cameras arranged in two rings (8 in each ring) with 22.5 degrees

orientation difference. [Chen 2006, Furenlid et al. 2004] Each modular camera in FastSPECT II comprises a 11.43 cm × 11.43 cm × 0.5 cm NaI(Tl) scintillator coupled to 3×3 PMT array via a 1.5 cm-thick light guide. List-mode data are acquired using CGRI-designed electronics and MLE is used for event position and energy estimation. [Furenlid et al. 2004]

FastSPECT III is the third FastSPECT system developed in CGRI, and was designed for rodent brain imaging to study neurological pathologies including Alzheimer's and Parkinson's diseases, which both require high-resolution images of uptake of tracers in brain regions. Unlike the the previous two generations, FastSPECT III was constructed with 20 iQID scintillation cameras arranged in three rings, with 10 cameras in the central ring and 5 in each outer ring. An imaging aperture made from tungsten composite and twenty 250μm platinum pinholes (one for each iQID) is used for gamma-ray imaging. [Miller et al. 2009a] The pinhole apertures and iQID cameras are positioned such that a common FOV of 15mm (diameter) sphere is formed. Each iQID camera consists of a 55-mm-diameter 450-μm-thick columnar CsI(Tl) scintillator, a 2nd-generation XX1332 military surplus image intensifier, a Fujinon 6-mm-focal-length F1.2-F16 lens, and a Point Grey Research DragonFly Express CCD sensor with 640×480, 7.4μm ×7.4μm pixels and up to 200fps frame rate. [FLIR] Figure 4.1 shows the FastSPECT III system and the iQID camera configuration used.

Despite the high linear spatial resolution of ~250 μm demonstrated by 3D reconstruction of a micro-resolution phantom [Miller 2012c] and all the other advantages of the iQID cameras, three main issues arose in the application phase of FastSPECT III. First, it was observed that some of the XX1332 military surplus image intensifiers generate random events that tend to concentrate in the center of the output phosphor screen after amplification, called "central spot" background. If not discriminated, these false events will mix with real gamma-ray events and cause artifacts in 3D reconstructed images. Second, the originally-employed columnar CsI scintillators have a thickness of only 450 μm that yields low efficiency for absorbing higher-energy gamma-ray photons, such as the 140keV gamma-rays emitted by the most commonly used radioisotope, ^{99m}Tc. This has greatly limited the system sensitivity of FastSPECT III such that low-dose imaging, such as mouse imaging of brain, often resulted in too-low S/N ratio for 3D image reconstructions. Finally,

FastSPECT III was configured to provide a 15-mm-diameter, spherical common FOV (CFOV) for high-resolution imaging yet has a much larger total FOV (TFOV). High-resolution performance in the FastSPECT systems requires high-precision calibration, but in FastSPECT III, the count-rate when all events occur in a small region on the detector is limited by the frame rate so that only the CFOV can be calibrated within the lifetime of a lab-prepared radioactive point source. In mouse imaging and other imaging tasks, however, the volume of the mouse or the distribution of the radiopharmaceuticals is often much larger than this CFOV. Activity outside of the calibrated CFOV while inside the TFOV generates extra events in some iQID cameras that cause inconsistency with calibration data and artifacts in reconstructed images.

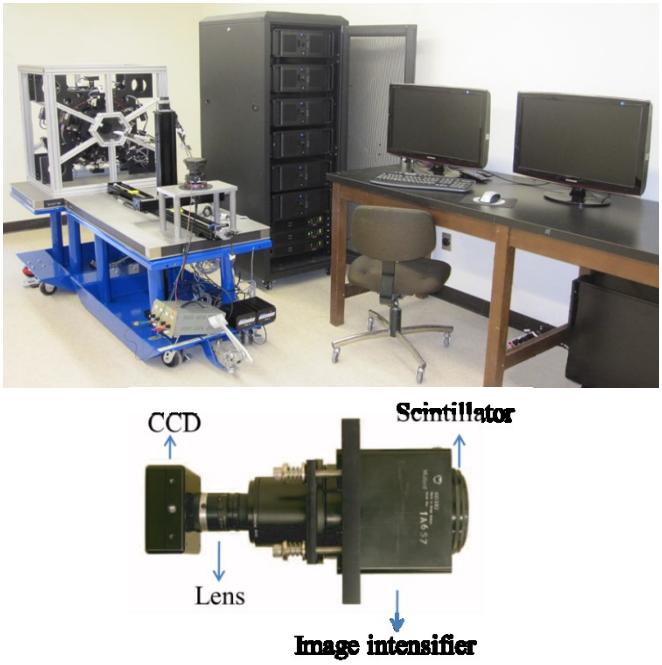

Figure 4.1: The FastSPECT III system (Top) and an iQID camera on the system (Bottom).

In order to advance iQID cameras and solve the above mentioned problems in the FastSPECT III systems, a new frame-parsing algorithm was developed and integrated into FastSPECT III that eliminates the central-spot background of XX1332 image intensifiers in real time based on statistical analysis. A new 1.65-mm-thick columnar CsI(Tl) scintillator was also installed on each iQID camera after evaluation and comparison studies with the original 450-μm columnar CsI(Tl) scintillator in terms of sensitivity and spatial resolution, which greatly improves FastSPECT III's sensitivity. Finally, a new system calibration

method was developed that is able to cover a much larger volume to reduce or eliminate inconsistency between projection image and calibration data, while maintaining high spatial resolution in the CFOV. System performance evaluations with both phantom and mouse were carried out after all of these advances were completed.

4.2 Advanced Frame Parsing Algorithm

4.2.1 Central Spot Noise

The advanced frame-parsing algorithm was developed to perform event estimation and remove the central-spot background generated by the XX1332 image intensifiers employed in the iQID cameras of FastSPECT III. The XX1332 image intensifier is a 2^{nd}-generation image intensifier with a 50-mm-diameter input window and a 40-mm-diameter output window. It has a plano-concave, fiber-optic entrance faceplate with S-25 photocathode deposited on the inside of a curved entrance window, an electro-optical inverse-focusing mechanism to direct photoelectrons to a micro-channel plate (MCP) for electron amplification, and a P20 phosphor exit screen. The total optical gain is approximately 45,000. Figure 4.2 shows a schematic representation of a XX1332 image intensifier. The central-spot background is a special type of noise generated by the XX1332 image intensifier, which has a similar appearance to thermal noise events on an event-by-event basis but tends to concentrate in the center of the output surface. Figure 4.3 shows both an integrated image and a centroid image of the output phosphor screen under visible light and dark illumination. The central-spot is visible in both images. The physical origin of central-spot background events is not clear, but statistical analysis of the event properties has suggested effective solutions.

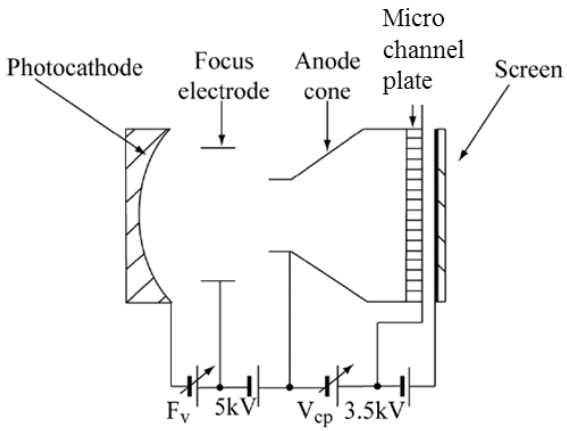

Figure 4.2: Schematic configuration of an XX1332 image intensifier.

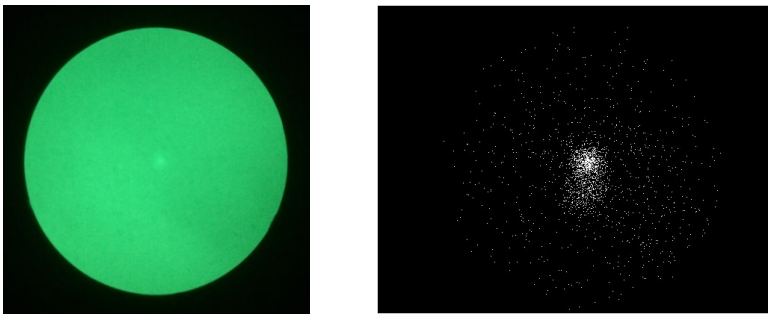

Figure 4.3: Integrated image of the phosphor screen of XX1332 image intensifier under visible light illumination taken with a cellphone camera (Left) and centroid image of the central spot under no light input taken with the iQID camera (Right).

4.2.2 Advanced Frame Parsing Algorithm

A fast frame-parsing algorithm based on GPU parallel-computing was already installed in the data acquisition system of FastSPECT III that is able to identify and process each gamma-ray event in real-time. [Miller et al. 2009] However, it's not capable of effective discrimination of gamma-ray events against central-spot background events in situations such as when the thicker scintillator was used to improve system sensitivity. The new frame-parsing algorithm needed to be integrated into the original data acquisition system while maintaining high-throughput real-time processing speed, along with stronger noise discrimination capability to remove central-spot events. Based on these requirements, the advanced frame-parsing algorithm was proposed with the following steps to identify the events from CCD background noise, extract their associated pixels, record the information in a list-mode file and discriminate against central-spot events:

(1) a frame from the CCD is acquired;

(2) a 3×3 average filter is applied to smooth the event energy distribution and connect isolated but close pixels belonging to the same event;

(3) the smoothed image is amplitude-thresholded above the CCD noise;

(4) individual clusters are identified using a fast connected-components-labeling algorithm and the pixels associated with each event are then extracted;

(5) important information such as total energy, size and interaction position of each event is estimated, and Figure 4.4 shows a step-by-step demonstration of this algorithm;

(6) events with smaller size than a preset size threshold are rejected. List-mode information of the other accepted events is recorded into a file.

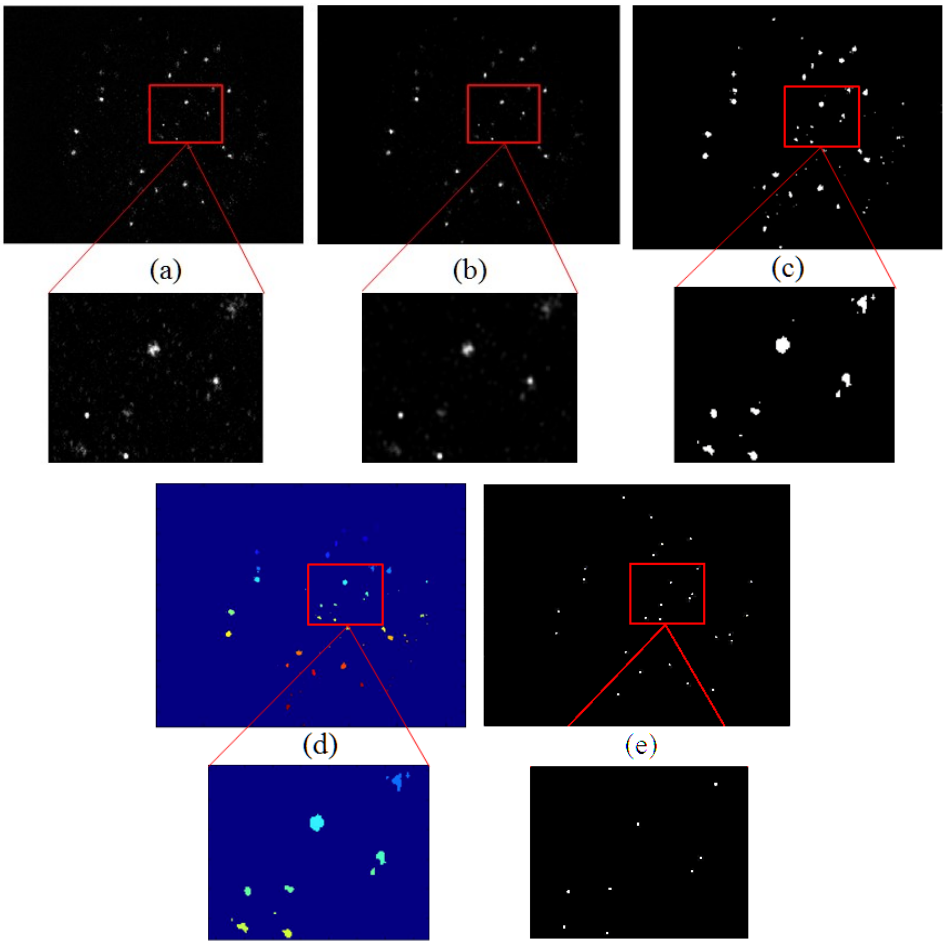

Figure 4.4: Advanced frame-parsing algorithm. (a) CCD frame with raw data. (b) Average-filtered image. (c) Amplitude-thresholded image. (d) Individual-cluster identified image using connected-components-labeling algorithm. (e) Centroid image after applying size threshold.

Compared with the original algorithm, the advanced frame-parsing algorithm can identify some loosely-connected low-intensity clusters, like the one shown in the lower left corner of the magnified image block in Figure 4.4. It's also able to remove many noise events including hot pixels and the central-spot noise using the combination of amplitude threshold and size threshold. Because no median filter, which is computationally expensive, is used, no GPU support is required to achieve real-time high processing speed, which reduces the cost of both hardware and software. To decide which size threshold is optimal for a given source and iQID configuration, a calibration experiment may be required to determine the size distributions of both background noise events and gamma-ray events. Finally, the advanced frame-parsing algorithm was integrated into the original data acquisition system of FastSPECT III with minimal modifications. Currently, the event-size information has been added to the list-mode file and a size threshold parameter control has been integrated into the setup screen for each iQID camera for central-spot-free data acquisition, as shown in Figure 4.5.

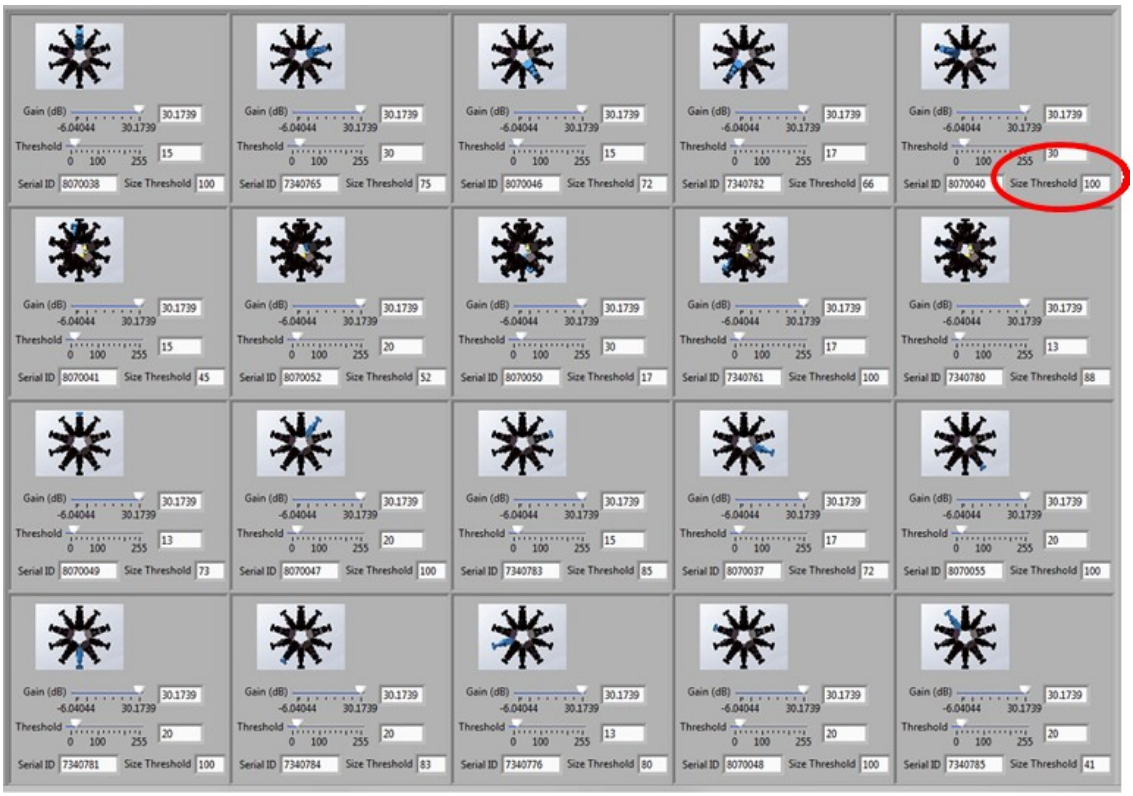

Figure 4.5: LabVIEW GUI of FastSPECT III for setting data acquisition parameters. A size threshold has been integrated for each iQID camera.

4.2.3 Evaluation

To evaluate the effectiveness of the advanced frame-parsing algorithm in central-spot background elimination, an experiment with a 1-mm-diameter ^{57}Co sealed-source (122keV) in front of the iQID camera was set up as shown in Figure 4.6. A circular aperture was placed in between to generate a circular projection of the source away from the central spot. The configuration including source activity, source-to-aperture distance, aperture size, and CCD frame rate were chosen such that no or only minimal multiplexing occured.

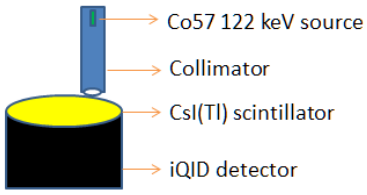

Figure 4.6: Experimental setup for studying the statistics of central-spot events and gamma-ray events using iQID camera.

The experiment was first performed with the 450μm columnar CsI(Tl) scintillator originally installed in the iQID camera. By setting a low amplitude threshold and no size threshold in the advanced frame-parsing algorithm, we could identify both image-intensifier background noise events and gamma-ray events based on their locations. Statistical distributions of different properties could then be generated for both types of events, including peak amplitude, cluster size, and total energy. After comparison of the distributions of different properties, only cluster size and peak amplitude were found to be distinguishable between background events and gamma-ray events. Figure 4.7 demonstrates distributions of event size and peak amplitude for both types of events and the centroid images before and after applying a size threshold.

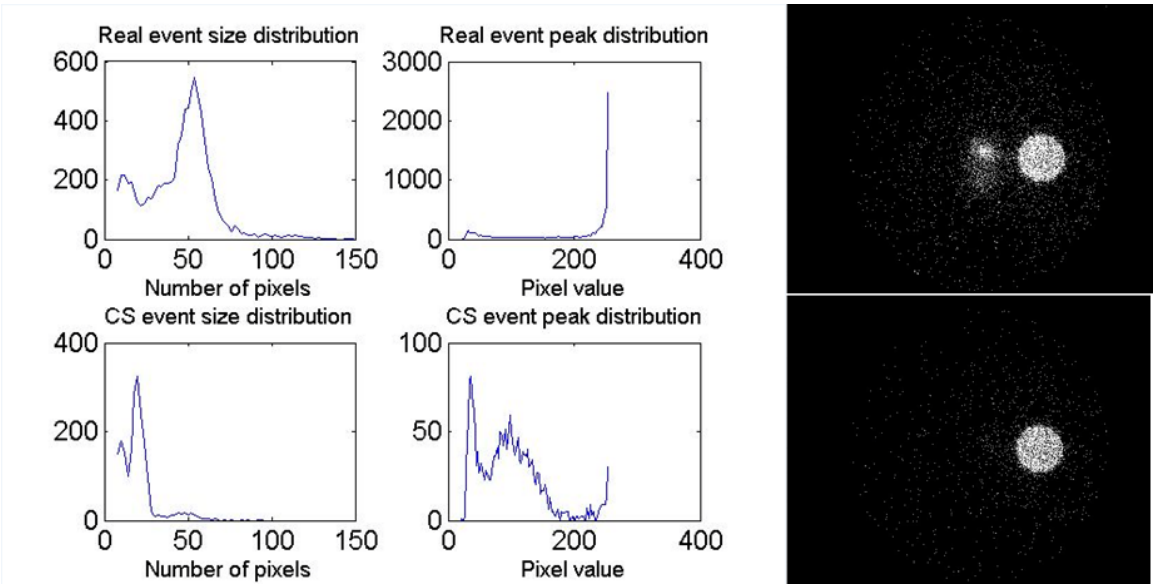

Figure 4.7: Central-spot background-elimination demonstration for 450μm CsI(Tl) scintillator. Left: the size distributions and peak distributions for both central spot (CS) events and gamma-ray events. Right: the centroid images before (Top) and after (Bottom) applying a size threshold of 30 pixels. The central spot noise is effectively removed.

With a relatively thin scintillator, the scintillation light experiences only modest attenuation so that the peak amplitudes of the majority of gamma-ray events can be higher than most central-spot events, allowing the use of an amplitude threshold in addition to a size threshold for removing the central spot. However, another experiment with the same setup, but using a 1.65mm-thick columnar CsI(Tl) scintillator, demonstrated the advantage of using the size threshold over the amplitude threshold to remove central-spot noise events. As shown in Figure 4.8, the peak amplitude distribution of true gamma-ray events has a large overlap with that of central-spot events, while the size distributions can be effectively separated with a simple threshold.

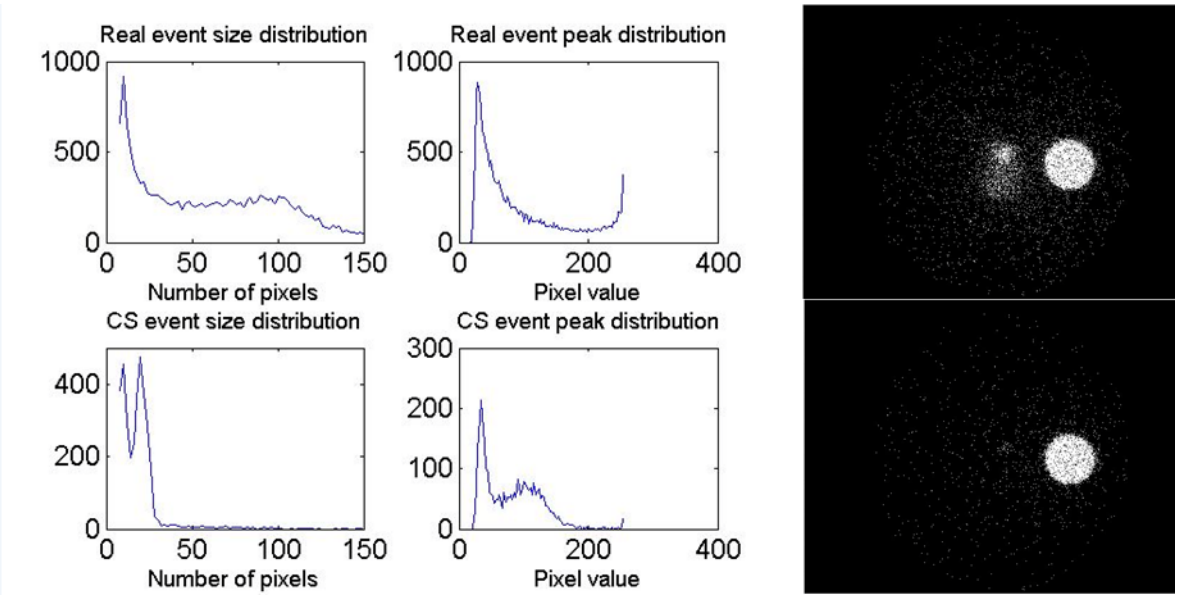

Figure 4.8: Central-spot noise elimination demonstration for 1650µm CsI(Tl) scintillator. Left: the size distributions and peak distributions for both central-spot (CS) events and gamma-ray events. Right: the centroid images before (Top) and after (Bottom) applying a size threshold of 30 pixels. The central-spot noise is removed effectively.

The reason why amplitude thresholding failed in the second case is that scintillation light experienced a larger range of attenuation during transportation in the thicker columnar scintillator, resulting in a continuous spread of amplitudes. The lateral spread of scintillation light, however, tended to increase for the thicker scintillator, making it feasible to remove central-spot events based on this size difference. To further evaluate the effectiveness of the advanced frame-parsing algorithm, a syringe of liquid ^{99m}Tc source was imaged using FastSPECT III equipped with 1650µm columnar CsI(Tl) scintillators. The application of the size threshold again effectively removed central-spot event noise from the projection image as shown in Figure 4.9.

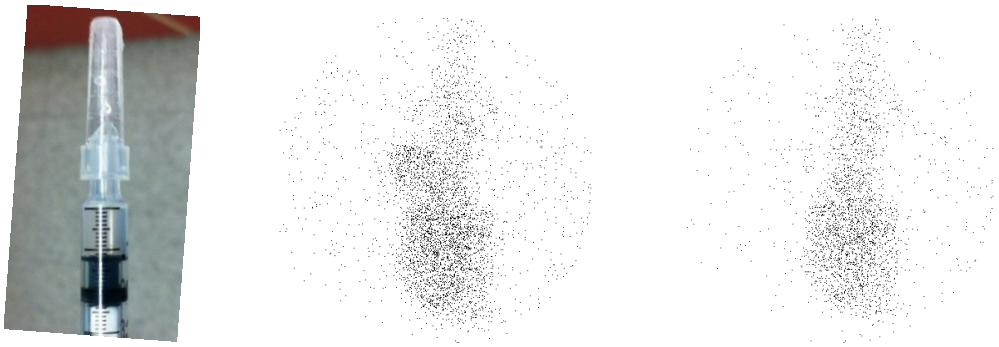

Figure 4.9: Demonstration of central spot elimination with the advanced frame-parsing algorithm running on FastSPECT III system. Left: A syringe of liquid Tc-99m source. Middle: Centroid projection image before applying size filter (central-spot noise present); Right: Same projection image after applying size filter (central-spot noise removed).

From these experiments and statistical analysis, we draw the following conclusions:

(1) Central-spot statistics do not change as long as we don't change image intensifier settings.

(2) The thicker the scintillator is, the more difficult it is to discriminate real events from central-spot noise events.

(3) Higher-energy gamma-rays balance light loss due to transportation and attenuation, so for optimal central-spot elimination, higher-energy sources are preferred.

(4) The advanced frame-parsing algorithm allows effective central-spot elimination and offers more flexibility in the removal of other noise events.

4.3 New Columnar Scintillator

To improve the system sensitivity of FastSPECT III, especially for a higher-energy sources, a 1.65mm-thick columnar CsI(Tl) scintillator was acquired from [RMD] and evaluated in terms of sensitivity and resolution performance. Since pinhole apertures are used on FastSPECT III, parallax error introduced by thick scintillator could affect detector resolution, so a study of the depth-of-interaction effect was also performed. Figure 4.10 shows photos of both the original 450µm columnar CsI(Tl) scintillator and the new 1.65mm columnar CsI(Tl) scintillator.

Figure 4.10: The original 450µm columnar CsI(Tl) scintillator on FastSPECT III (Left) and the new 1.65mm columnar CsI(Tl) scintillator (Right).

4.3.1 Detector Sensitivity

To assess the sensitivity achievable with both scintillators, a ^{57}Co (122 keV) source was placed above the iQID detector to provide a flood illumination. The distance between the source and detector was adjusted such that minimal overlap between events occurred. The experiment was performed for both 450 µm CsI(Tl) scintillator and the new 1650 µm CsI(Tl) scintillator and used the new frame-parsing algorithm to suppress the central-spot background. The experimental setup and the flood images with both scintillators are shown in Figure 4.11. The acquisition time for both flood images is 30 seconds.

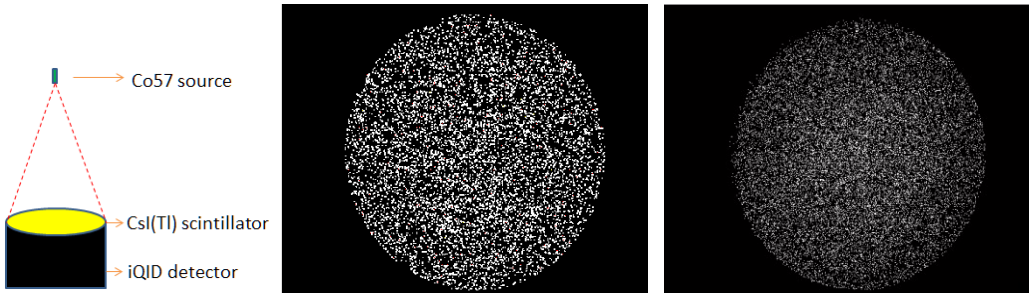

Figure 4.11: Experimental setup for sensitivity measurement (Left) and flood image of 30 seconds acquisition for 450µm CsI(Tl) scintillator (Middle) and 1650µm CsI(Tl) scintillator (Right).

During the above 30-second-exposure experiments, we acquired 11546 counts as a measure of sensitivity for the 450μm CsI(Tl) scintillator and 31629 counts for 1650μm CsI(Tl) scintillator. Given the known activity of the gamma-ray source, the solid angle subtended by the image intensifier, the stopping power of both scintillators and their substrates, and the acquisition time, theoretically there should ideally be ~39000 gamma-ray interactions for the 1650 μm CsI(Tl) scintillator and ~14000 gamma-ray interactions for the 450 μm CsI(Tl) scintillator. Thus an estimated sensitivity loss of ~20% is incurred for central-spot elimination. The new scintillator, however, still provides ~3 times higher sensitivity performance.

When we lowered the size threshold to keep more events, we acquired 48307 counts as a net measure of the sensitivity after subtracting the number of central-spot events, which is above the theoretical value of ~39000. This phenomenon was only found for the thicker scintillator. Several reasons may apply. First, due to the extra thickness, K x-rays have larger probability to interact with the scintillator instead of escaping. Second, Compton-scattered gamma rays also have larger probability to interact again with the scintillator instead of escaping. Because the frame-parsing algorithm is not able to recognize the primary gamma-ray interaction and the spatially-separated reabsorbed K x-ray or Compton-scattered gamma-ray as one event if they are laterally distant from one another (>1 mm), it's likely that they are sometimes counted as two events. Finally, the thicker scintillator also absorbs more background radiation events, though this cannot account for more than a small fraction of the extra counts.

The thicker scintillator was installed on all iQID cameras in FastSPECT III. The total system sensitivity is measured to be ~50cps/MBq for a 140keV gamma-ray source such as ^{99m}Tc, which is ~3-times higher than the original sensitivity of 16cps/MBq.

4.3.2 Spatial Resolution

To measure how the detector intrinsic resolution varies with different scintillators, a 50-μm-wide tungsten slit aperture was used to generate a line image on the iQID detector. If every component of the iQID detector was perfect with no spatial resolution degradation, the line image will have a width of <1 pixel. The experimental setup is shown in Figure 4.12 along

with the acquired line images. Both scintillators were tested to compare their effects on detector resolution.

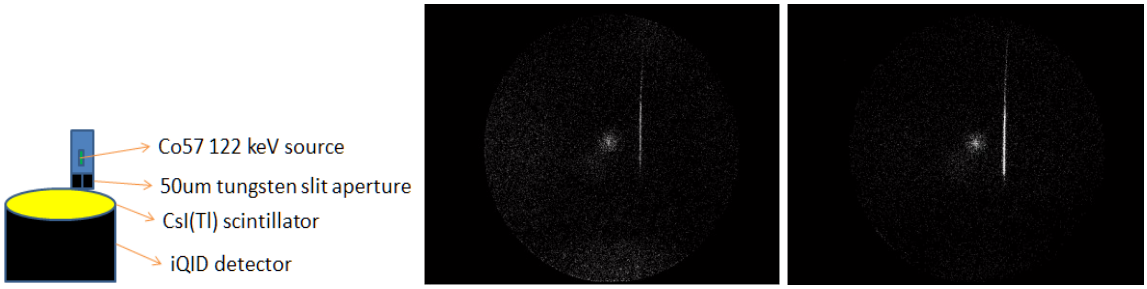

Figure 4.12: Experimental setup for detector resolution measurement (Left) and line images for both 450 µm CsI(Tl) scintillator (Middle) and 1650 µm CsI(Tl) scintillator (Right).

Both line images were taken with two minute acquisitions, and normalized Gaussian-fit line-spread-functions (LSF) were generated as shown in Figure 4.13. The DC signal due to central spot noise and other background radiation was subtracted when generating the LSF. Due to more Compton scattering and lateral spread of scintillation light, the thicker scintillator provided poorer spatial resolution. However, because the other components of iQID all have high-spatial-resolution performance, an excellent intrinsic spatial resolution of ~300 µm was still found.

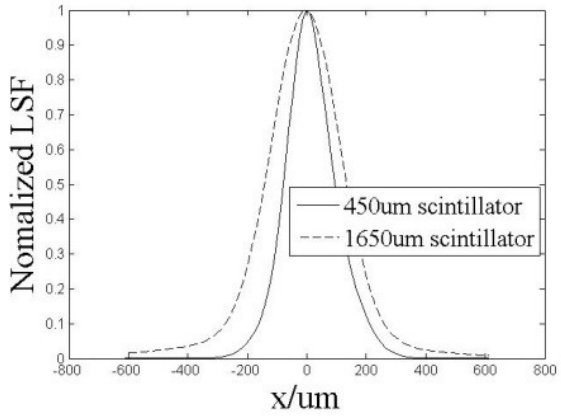

Figure 4.13: Normalized Gaussian-fit line spread function for both scintillators: the FWHM is 150 µm for the 450 µm CsI(Tl) scintillator and 300 µm for the 1650 µm CsI(Tl) scintillator.

4.3.3 Depth of Interaction Effect

The new CsI(Tl) scintillators thus yielded excellent spatial resolution and provided much higher sensitivity than the original CsI(Tl) scintillators. Another effect that needed to be investigated, especially for the thicker scintillator, is the parallax error, which can limit resolution performance at the edge of the FOV. Generally, with iQID we only estimate 2D position of each gamma-ray interaction instead of the 3D position inside the scintillator. Not estimating interaction depth translates into an error in the source location during back projection, thus degrading the image resolution during reconstructions. In a SPECT system like FastSPECT III, the resolution of 3D reconstructed images will be affected. Figure 4.14 depicts the parallax error.

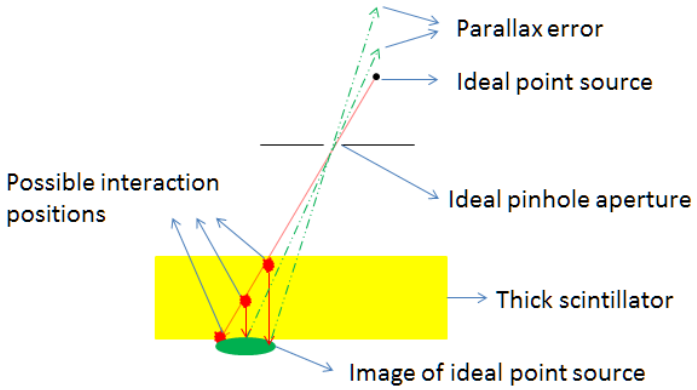

Figure 4.14: Parallax error illustration using an ideal point source, ideal pinhole aperture and a thick scintillator. A finite-size projection of the ideal point source can be caused due to the thickness of the scintillator, which leads to ambiguous source location when the interaction depth is unknown.

To reduce the parallax error especially with thick scintillators and oblique rays, the interaction depth should be estimated for each event. Furthermore, the 3D interaction position and event energy should be estimated with maximum-likelihood estimation (MLE) to gain the advantage of ML such as asymptotic lack of bias. A depth-of-interaction (DoI) calibration is usually required to determine the relationship between scintillator-light output and 3D-interaction position as prior information for implementing MLE. Here we performed a DoI study with both simulation and experiments to explore how the event size and amplitude vary with gamma-ray interaction depth for the new thicker columnar CsI(Tl) scintillators.

DoI Simulation

The simulation was performed in FRED, an illumination-design and ray-tracing software. According to a US patent on the fabrication of pixelated micro-columnar scintillators [Nagarkar and Tipnis 2005], the cross section of a column can be square, octagonal, and circular. The tip of a column can be conical, pyramidal, or flat. The substrate top surface can be non-coated or reflective-coated.

In this simulation, the chosen configuration for the columnar scintillator included a BK7 glass substrate, circular columns with wedge gaps, and conical tips. Three different coating conditions were simulated as well, i.e. non-coated, column 95% reflective and substrate 100% reflective. The detailed simulation parameters are listed in Table 4.1. For each gamma-ray interaction, 10000 scintillation photons were generated and traced with the Monte Carlo method. Figure 4.15 shows a FRED rendering of the simulated micro-columns and ray tracing results for 10 scintillation photons.

Substrate dimensions	2000(x)×2000(y)×1000(z) μm
Substrate coatings	Uncoated, 100% Reflective
Column dimensions	20(Base Diameter) ×10(Top Diameter) ×1000(Length) μm
Column coatings	Uncoated, 95% Reflective
Column tip	90 degree cone
Gap dimensions	0.2(Base Diameter) ×10(Top Diameter) ×1000(Length) μm
Excited-electron range	1(x)×1(y)×20(z) μm

Table 4.1: Detailed specifications of the simulated columnar CsI(Tl) scintillator.

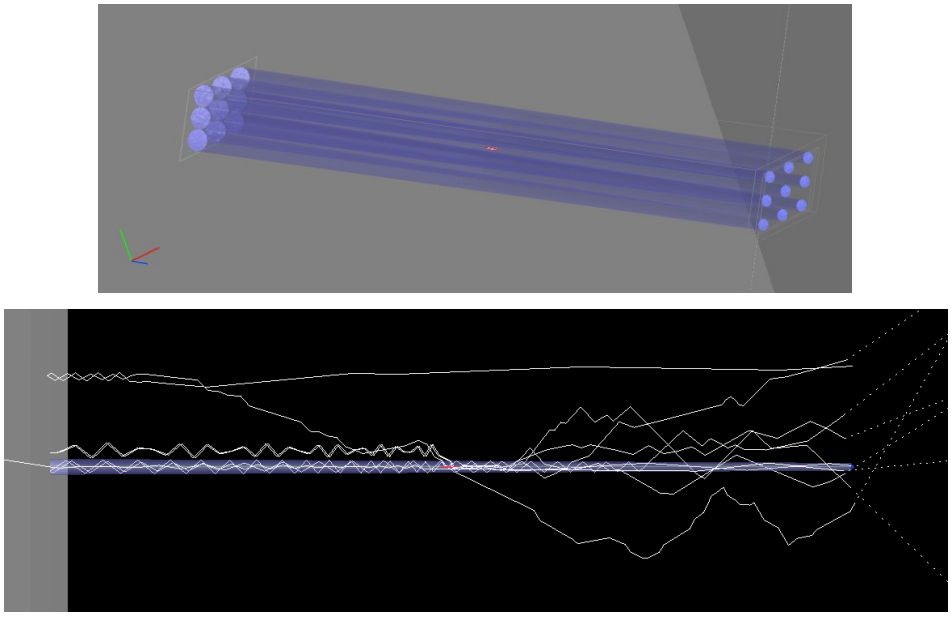

Figure 4.15: Top: FRED rendering of the scintillator columns with wedge-shaped gap. Bottom: Ray tracing demonstration of 10 scintillation photons.

To measure the scintillation light output and lateral spread, an ideal detector was placed close to the exit face of the scintillator. The number of photons detected by the detector was used as the measure of the light output. As illustrated in Figure 4.16, the RMS spot radius after applying an irradiance threshold was calculated as a measure of the lateral spread. By varying the gamma-ray interaction depth in a micro-column and tracing generated scintillation photons, the light output and lateral spread as a function of source location (interaction depth) could be plotted, as shown in Figure 4.16.

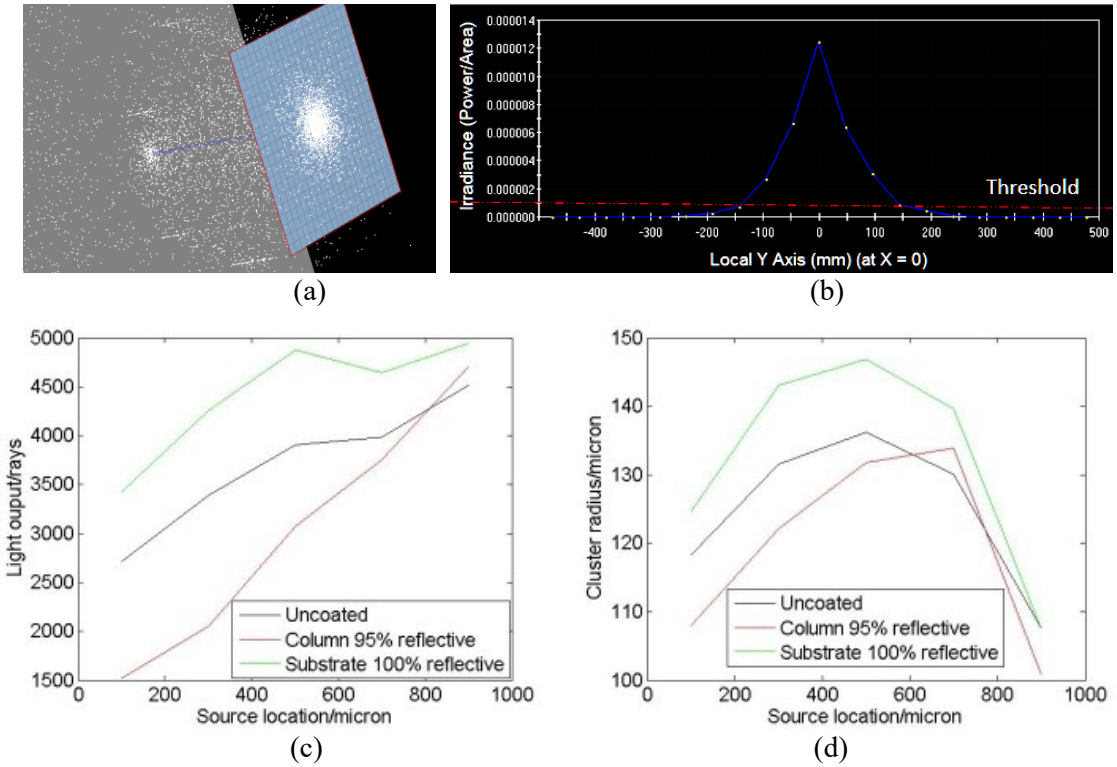

Figure 4.16: (a) Plot of ray-tracing results of 10000 scintillation photons. (b) Illustration of irradiance threshold for RMS-spot-radius calculation. (c) Light output vs. source location under different coating conditions. (d) Lateral spread vs. interaction depth under different coating conditions.

DoI Experiment

The DoI experiment used a 50-µm-wide tungsten slit aperture and the 1650-µm-thick scintillator configured as in Figure 4.17. Then, using a ^{57}Co source and the iQID detector, we acquired the slit projection image over 3-minutes acquisition. For each event produced through the slit aperture and included in the red rectangular region, an ML estimation based on a Gaussian model was performed to estimate the energy, 2D- interaction position and spatial variance. Since the angle of incidence of gamma rays was known, the interaction depth could be calculated based on the 2D interaction position. After all events inside the red region were processed, correlation plots of event energy and light output diameter versus interaction depth were generated, as shown in Figure 4.18.

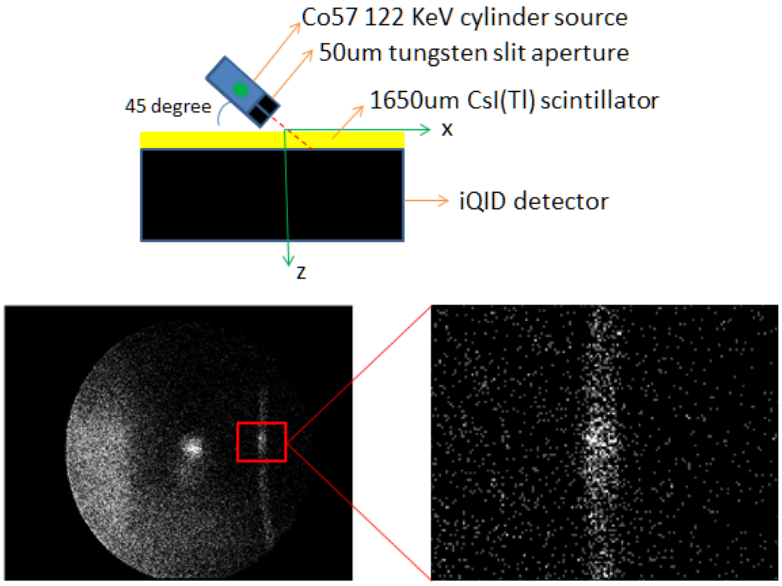

Figure 4.17: Top: Experimental setup for DoI study. Bottom: Projection image of the tungsten slit aperture acquired in 3 minutes. The width equals the thickness of the scintillator due to the 45-degree incidence angle.

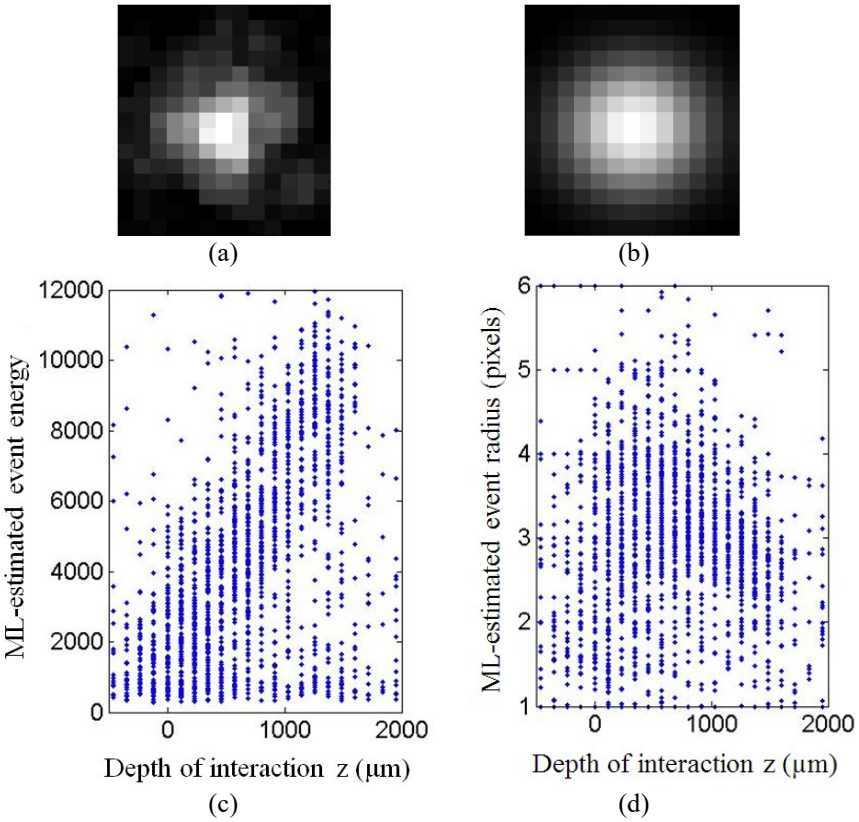

Figure 4.18: (a) Extracted cluster from raw frame data. (b) Gauss-fit result of the cluster in (a). (c) Event energy vs. interaction depth. (d) Event radius vs. interaction depth.

Summary

The experimental results agree with the simulation results. As expected, the detected event amplitude increases proportionally with larger interaction depth and reduced attenuation. The event size, represented by the standard deviation or the RMS of the spot radius, is found to have a maximum value at a certain interaction depth, about 500μm away from the exit surface in the simulation and 1000μm away from the exit surface in the experiment. When the interaction location moves away from the exit face, the event size or lateral spread initially increases, which can be easily understood. However, when the distance keeps increasing, attenuation of scintillation photons propagating through the crystal starts to dominate by absorbing weak signal in the outermost regions. Finally when the distance becomes so large that most energy of the initial scintillation light is absorbed by the scintillator, the event size will shrink with much fewer pixels above threshold. So for thick columnar scintillators, a non-monotonic relationship between event-size and depth was discovered as the result of the balance between absorption of light inside the scintillator and the light cross-talk effect between neighboring columns. This depth-of-interaction study provides the relationships between event energy, event size and interaction depth, which can be used as prior information in ML estimation or assist with detector simulations.

4.4 New System Calibration

SPECT systems can be described by a discrete-to-discrete model as

$$\mathbf{g} = \mathbf{Hf} + \mathbf{n} \ , \tag{4.1}$$

where **f** is the object represented by an N×1 vector of voxels, **H** is the system matrix of M×N elements, **n** is the image noise represented by an M×1 vector of pixels and **g** is the digital projection image represented also by an M×1 vector of pixels. For each voxel in the object, the system can generate a corresponding M×1 vector of pixels as the system response, called a point spread function (PSF). Each column of **H** is a PSF for a voxel of the object and the process of acquiring **H** is called system calibration. An estimate of the object **f** can be reconstructed once the system PSF matrix, **H**, is determined either by measurement or by simulation. This section introduces a new system calibration method for high-resolution pinhole SPECT system with CCD/CMOS- based gamma cameras. The proposed method was implemented on the FastSPECT III system.

4.4.1 Introduction

In recent years, pinhole SPECT systems have become more and more popular because of their high resolution and sensitivity characteristics. They are particularly useful in preclinical or small-animal imaging applications. Many pinhole SPECT systems have been developed that are able to provide <2mm or even <0.5mm resolution performance. [Schramm et al. 2003, Beekman et al. 2005, Funk et al. 2006, Kim et al. 2006, Miller 2012b, Durko 2014, Chaix 2015] When high-magnification pinhole apertures are used, the 3D reconstructed image can provide resolution even better than the intrinsic resolution of the gamma camera. The high-resolution performance, however, also poses great challenge for high-accuracy system calibration. Resolution loss, artifacts, and even reconstruction failure can be caused by using an inaccurately or improperly determined H matrices during tomographic reconstructions.

Several pinhole-SPECT calibration methods have been proposed, which mainly fall into two categories, geometry characterization or exhaustive measurement. Geometry characterization is mainly used on rotating SPECT systems. Analytical models with

necessary intrinsic and extrinsic parameters describing the pinhole projection geometry are used to calculate the H matrix. By imaging specially-designed point-source phantoms and fitting the image data with analytical models, parameters of the model can be estimated. For example, Bequé et al. used a phantom with three non-collinear point-sources to estimate the seven parameters necessary to describe their acquisition geometry and later optimized the configuration of the point sources for image-reconstruction accuracy. [Bequé et al. 2003, 2005] Many other efforts have gone into geometry modeling and calibration of cone-beam tomography systems. [Gullberg et al. 1990, Hsieh et al. 1997, DiFilippo 2008] Although many groups have achieved satisfactory image quality for modest-resolution clinical applications, factors affecting calibration accuracy have been found for high-resolution systems, such as correlations between the seven parameters, and mechanical stability and accuracy of scanners. Prior knowledge of the parameters and a restricted search domain were used to address the correlation problem [Li et al. 1993]. Separate estimation of intrinsic and extrinsic parameters with separate measurements was also adopted to avoid correlation errors in simultaneous estimation of all parameters. [Rizo et al. 1994] Refinement of the calibration was proposed to solve the mechanical stability issue and provide stable estimates [Defrise et al. 2008].

Calibration through exhaustive measurement is the ultimate calibration method pioneered with the FastSPECT systems developed at CGRI, and mainly used on stationary SPECT systems. [Furenlid et al. 2004] With multiple cameras and pinhole apertures fixed, stationary SPECT provides excellent stability and capabilities for dynamic studies. In the exhaustive measurement, a fabricated radioactive point source is sequentially scanned by motorized stages across the FOV, and the PSF corresponding to the point source at each voxel location is recorded. The H matrix is then constructed by smoothing and interpolating the sampled system response matrix. [Chen et al. 2005] This method is able to calibrate detector blur, sensitivity and resolution of each pinhole aperture, any mechanical misalignment, gain variations, and any other characteristics of the gamma cameras into the H matrix. Although it's the gold-standard method that is able to provide the most accurate calibration, modern high-resolution SPECT systems require the voxel size to be as small as 0.1-0.2mm, greatly increasing the number of voxels to cover the necessary FOV and the

space for data storage. By storing only non-zero elements, the size of H matrix can be greatly reduced. For sub-half-millimeter resolution SPECT systems, however, this method still leads to very large H matrices because of the fine sampling with high-resolution sensors. By assuming a Gaussian model for each PSF, six parameters can be calculated and stored instead, resulting in a significantly smaller calibration files. [Chen 2006] GPU-based on-the-fly computation of the H matrix can then be performed using the six parameters during iterative reconstructions. [Miller et al. 2012c] Use of an analytical pinhole models combined with point source measurements at a limited number of positions is also used on high-resolution stationary SPECT systems to address the data storage problem. [van der Have et al. 2008]

The high-resolution performance of pinhole SPECT systems is often achieved by using large-magnification pinhole apertures and small CFOVs, while the TFOV of all gamma cameras may be much larger. Any activity in the TFOV that is outside of the calibrated volume would cause data inconsistency and result in resolution loss, artifacts and even failure of image reconstruction. As a result, the calibration, ideally, should cover the TFOV. This is often prohibitively time-consuming and not practical using exhaustive measurements method due to the large volume, small step sizes between pinholes, as well as limited lifetime and activity of the fabricated point source. To cover as much FOV as possible while maintaining high-resolution performance, a new calibration method is proposed here that is time efficient, storage efficient, accurate and easy to implement by incorporating a hybrid scan of the radioactive point source with analytical and empirical models. This method was implemented on FastSPECT III, where distortion and optical magnification also need to be calibrated due to the use of image intensifiers and lens-coupled CCD sensors. The performance of this calibration was evaluated with both phantom and mouse imaging; results are presented in section 4.6.

4.4.2 Acquisition Parameters Adjustment

It has been observed that XX1332 image intensifiers have temperature-induced gain drift, which could change system sensitivity and cause a prior system calibrations to be inaccurate at the time of imaging. A new system calibration is typically required, which can be time-

consuming. Fortunately, the new frame-parsing algorithm offers two degrees of freedom in event processing, and by properly selecting the combination of both amplitude and size thresholds, the sensitivity change caused by gain drift over time can be at least partially compensated or balanced. If consistent criteria are used during system calibration, the same criteria can be met by adjusting the two acquisition thresholds shortly before imaging such that the prior system calibration remains accurate.

The criterion chosen in this work is equal sensitivity response across all iQID cameras on FastSPECT III for a point source at the center of the FOV. When a point source is fabricated, the activity is measured by a counter. Then the point source is positioned to the center of FOV. By setting relatively-low amplitude and size thresholds, list-mode data including the size information of all events for a short acquisition time (10 minutes, for example) are acquired for each iQID camera. Example centroid images of the point source from the 20 iQID cameras are shown in Figure 4.19. After identifying the projection regions of the point source, a relationship between the sensitivity of each camera and the threshold parameters can be generated by post processing the list-mode data. An example is shown in Figure 4.20, where a chosen criterion is plotted with blue lines. Based on the resulting curves, proper thresholds can be set to meet the criterion, and the system is ready for acquisition.

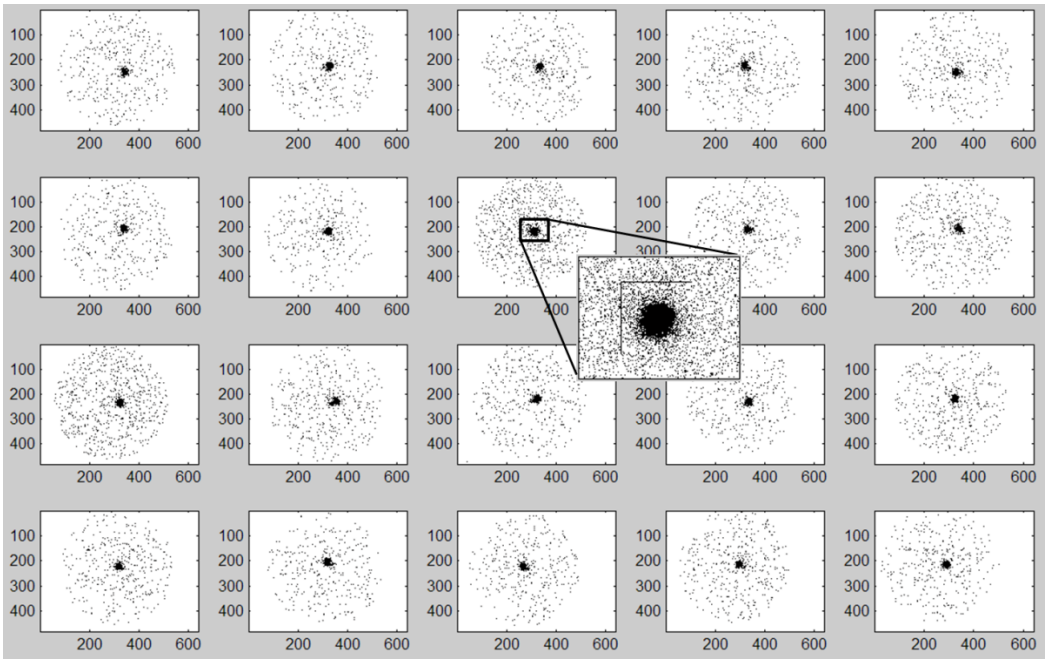

Figure 4.19: Centroid images of a point source with the projection regions identified.

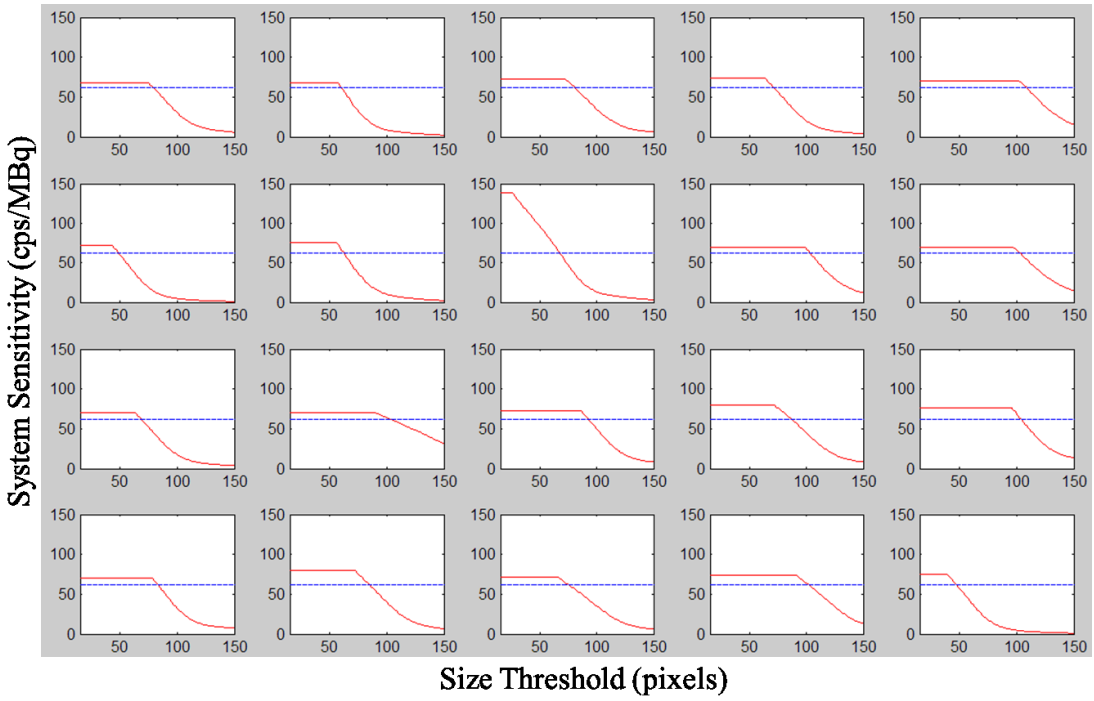

Figure 4.20: Variation of system sensitivity responses as a function of size threshold. Blue lines indicate a chosen criterion for proper threshold settings.

The parameter adjustments can be performed with the same point source fabricated for system calibration, and the procedure requires only 10-15 minutes. For future imaging tasks, a sealed radioactive point source such as ^{57}Co can be used, such that no point source needs to be fabricated. Once adjusted, the acquisition parameters set the system into a similar state as to when the system was calibrated, which maintains the accuracy of previously acquired calibration matrix. Although this method is applied to FastSPECT III system, the idea of fine tuning acquisition parameters to balance gain fluctuations is also routinely carried out on other SPECT and PET systems. [Simmons 1988]

4.4.3 Hybrid Scan

For a stationary SPECT system, the exhaustive measurement calibration method usually starts with the scanning of a fabricated point source in a regular-grid pattern. The step between two adjacent positions is fixed, which determines the sampling of the calibration and the pattern is usually cubic or cylindrical. The number of grid points that can be measured is determined by the activity of the point source and the sensitivity of each gamma camera. The scanning step is determined as a compromise between the FOV and resolution

requirements. For example, in the original system calibration, a point source made from ^{99m}Tc usually contained activity of ~400μCi and could support up to an 11×11×11 cubic scan on the FastSPECT III system. The total acquisition time was ~12 hours with 15-seconds of acquisition time for the first position. The maximum scanning step was 1.5mm and an interpolation factor of 7 was used to provide 0.214mm voxels for high-resolution reconstructions. This resulted in a maximum scanned volume of 15×15×15mm^3, which was enough to cover the 15mm-diameter-sphere common-FOV, but not enough compared with the overall size of a mouse.

To substantially increase the scanned volume while maintaining high-resolution performance in the CFOV, a hybrid multi-gridded scan was developed that consists of two interleaved cylindrical scans, one with small scanning step over a small volume and another with large scanning step over a surrounding large volume. Specifically, the first scan covers a cylindrical volume of 15mm (diameter) ×15mm (depth) with 891 positions and a 1.5mm step size in each direction. The second scan covers a cylindrical volume of 24mm (diameter) ×24mm (depth) with 441 positions and a 3mm step size. The second scan is performed immediately after the first scan is finished without interrupting the point source. Radioactive decay is considered during both scans and precisely compensated for by an increasing acquisition time. Starting with 15-seconds acquisition for the first position, both scans take about the same time of 6 hours (~12 hours in total) to finish. Figure 4.21 depicts a cross sectional view of the hybrid scan.

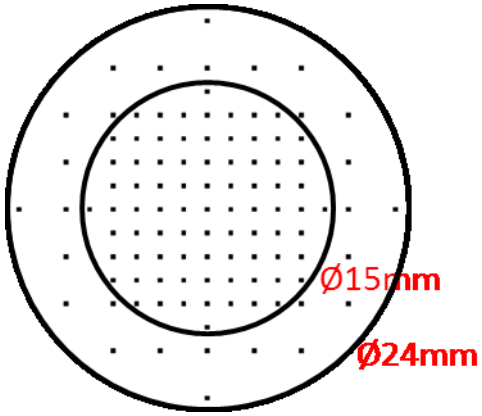

Figure 4.21: Cross section view of the hybrid scan. Two traditional cylindrical scans with different sampling density are overlapped.

Compared with the original 11×11×11 cubic scan, the hybrid scan is able to cover a ~4-times larger volume, with the same acquisition time and the same accuracy in the CFOV. Since the point source is not interrupted during the whole scan, high-precision motorized stages guarantee the coincidence of the centers of both scans. There are a total of 105 repeated positions between the two scans, which can help reduce the uncertainty of system responses and increase calibration accuracy in the CFOV. Although the second scan uses a larger step size that could reduce calibration accuracy for the outer region, the much larger scanned volume solves the inconsistency problem and removes artifacts that would otherwise appear in the reconstructed object.

4.4.4 Gaussian Fitting

After the hybrid scan is finished, PSFs of all source positions are stored in list-mode files. However, due to a lot of counting noise, the measured PSFs cannot be directly used in image reconstruction. To reduce random counting noise and recover the mean PSF responses, Gaussian fitting is applied using a least-squares algorithm, which also substantially suppresses the necessary information to be stored. It's also employed in FastSPECT II [Chen 2006] and the accuracy and reproducibility has been estimated on FastSPECT III [Miller et al. 2012c]. Six parameters including amplitude A, centroid position $\bar{x}$ and $\bar{y}$, standard deviation σ_x and σ_y, and correlation coefficient ρ are used to parameterize the 2D Gaussian model. Normalization based on the energy conservation principle is also applied. Mathematically the 2D Gaussian model is described as

$$h_{in}(x,y) = \frac{A}{2\pi\sigma_x\sigma_y\sqrt{1-\rho^2}} \times exp\left\{-\frac{1}{2(1-\rho^2)}\left[\frac{(x-\bar{x})^2}{\sigma_x^2} + \frac{(y-\bar{y})^2}{\sigma_y^2} - \frac{2\rho(x-\bar{x})(y-\bar{y})}{\sigma_x\sigma_y}\right]\right\} \quad (4.1)$$

where i is the index for each iQID camera and n is the index for each source position. After Gaussian fitting, each measured PSF is represented by six parameters, which are stored in a file and will be used during reconstruction. Figure 4.22 demonstrates some examples comparing the measured PSFs with Gaussian-fit PSFs. The point source was made from ^{99m}Tc with ~400 μCi activity, and PSF-acquisition time for the starting position was 15 seconds.

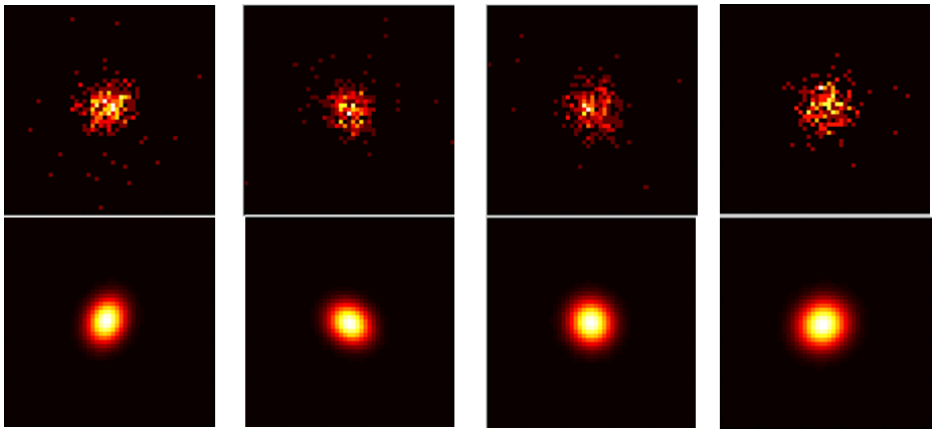

Figure 4.22: Comparison between measured PSFs and Gaussian-fit PSFs.

4.4.5 System Models

The hybrid scan provides accurate PSF information with only 1227 source positions in a 24mm (diameter) ×24mm (depth) cylindrical volume, which means an average voxel size of ~2×2×2 mm. To provide ~0.2mm voxels for high-resolution reconstruction on FastSPECT III, almost 1000-times more source positions need to be interpolated, which could cause large interpolation error. To get around this problem, multiple analytical and empirical models were developed to estimate the system response (sensitivity, 2D projection location, pinhole and detector blur) for a point source at arbitrary locations in the FOV. By minimizing the difference between estimated and measured system responses, parameters of the models could be accurately estimated. An H matrix with any voxel size can then be established based on the system models.

1) Effective Detection Region

Due to the finite detector area and large scanned volume, the PSF of a point source placed far from the center of FOV could be truncated at the edge of the effective detection region, causing an abrupt change of system response. These truncated PSFs will greatly affect the accuracy of system characterization. To avoid the influence of these PSFs, a circular mask was used to estimate the boundary of the effective detector area and was described as

$$(u'' - u_0'')^2 + (v'' - v_0'')^2 = R^2 \tag{4.2}$$

where u'', v'' are the vertical and horizontal pixel coordinates of the projection image, (u_0'', v_0'') and R are the center coordinates and radius of the effective detection area, respectively.

An integrated image of all PSFs acquired by an iQID camera was used for estimating the effective region of that particular camera, as shown in Figure 4.23. Once the boundary is determined, a distance threshold is applied to remove any PSF that is too close to the boundary and has a high risk of being truncated.

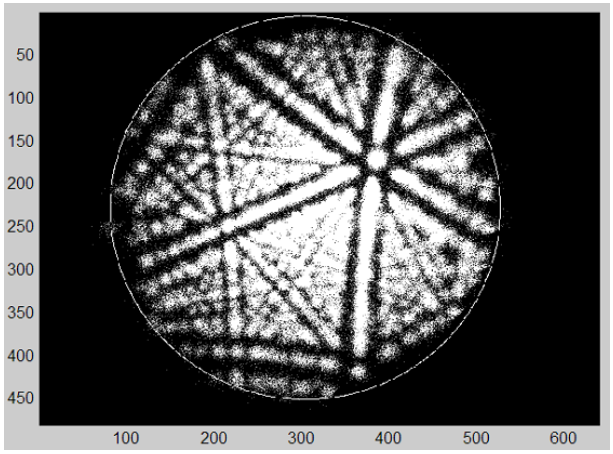

Figure 4.23: Estimation of the effective detection region of iQID camera.

2) Pinhole Projection

To be able to accurately predict the projected pixel location of a point source on an iQID camera, an ideal pinhole projection model, distortion correction and optical magnification model, and electrical shift model are required.

As was employed by Bequé et al. [2003], an ideal pinhole aperture is first assumed with the object space on one side and image space on the other side, as shown in Figure 4.24. The coordinate system of the motorized stages is denoted as xyz. A central ray is defined as the line perpendicular to the detector surface that passes through the center of the pinhole. The normal distance between the origin of the xyz system and the central ray is denoted m. A 2D coordinate system uv is defined on the detector plane with u and v parallel to the image axis and the line connecting uv origin, and xyz origin parallel to the central ray. As shown in

equation (4.3), with three rotations around x, y and z, a new coordinate system x’’’y’’’z’’’ can be defined, where x’’’ and z’’’ are parallel to u and v. The normal distance between the center of the pinhole and the x’’’y’’’ plane is denoted as d and the focal length between center of the pinhole and the detector plane is denoted as f. Then, the pinhole projection geometry is fully defined.

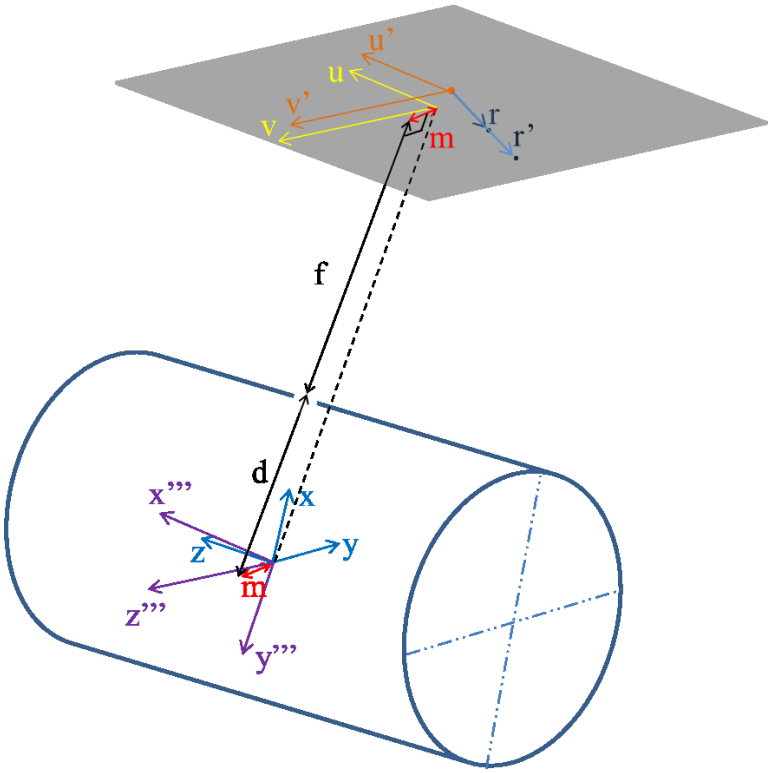

Figure 4.24: The fully-defined pinhole projection geometry.

$$\begin{bmatrix} x''' \\ y''' \\ z''' \end{bmatrix} = \emptyset_y \emptyset_x \emptyset_z \begin{bmatrix} x \\ y \\ z \end{bmatrix} \tag{4.3}$$

Based on triangle geometry and the pinhole projection model as defined above, the projection location (u, v) of a point source at (x’’’, y’’’, z’’’) can be calculated as

$$u = f\frac{m_u - x'''}{d + y'''} + m_u \tag{4.4}$$

$$v = f\frac{m_v - z'''}{d + y'''} + m_v \tag{4.5}$$

where m_u is the projected m along axis u and m_v is the projected m along axis v.

Because of the use of an image intensifier and optical lens, distortion is present in the image. To correct for the distortion, a coordinate system u'v' is defined with u' and v' parallel to u and v, and the origin aligned with the optical axis of the image intensifier as shown in Figure 4.24. The optical axes of the image intensifier and the lens are assumed to be aligned. With a third-order radial distortion model, the projection location of the point source can be recalculated as

$$r' = r + k_1 r + k_2 r^2 + k_3 r^3 \tag{4.6}$$

Before the final pixel location of the point source can be estimated, electrical shift and magnification need to be corrected. The electrical shift is a collective translation of the projection image and is caused by detector hardware drift. [Bequé et al. 2003] The magnification is caused by both the image intensifier and the optical lens. To account for these two effects, a translation of the projection image followed by a scaling are applied to estimate the final pixel location as

$$u'' = \frac{u' + e_u}{p} \tag{4.7}$$

$$v'' = \frac{v' + e_v}{p} \tag{4.8}$$

where e_u and e_v are the horizontal and vertical shifts, p is the effective pixel size at the detector plane, and u'' and v'' are the estimated pixel location in the image.

3) Sensitivity Model

The sensitivity determines the number of counts detected in each PSF and is mainly affected by the pinhole geometry and source location. However, because of uncertainty in the pinhole casting process, it's impossible to know the exact shape of each pinhole aperture. Vignetting can further complicate the relationship between sensitivity and source location. To accurately fit the sensitivity of measured PSFs at scanned point-source locations, an empirical exponential function of third-order polynomials was proposed, which relates the sensitivity to the 3D coordinates as

$$A = A_0 \exp(-(a_1 x_s + a_2 {x_s}^2 + a_3 {x_s}^3 + b_1 y_s + b_2 {y_s}^2 + b_3 {y_s}^3 + c_1 z_s + c_2 {z_s}^2 + c_3 {z_s}^3)) \quad (4.9)$$

where A_0 is an initial estimate of the sensitivity for the point source at the origin of $x_s y_s z_s$ system, which is a slightly translated version of the x'''y'''z''' system to have the origin aligned with the central ray.

4) Resolution Model

Similarly, to fit the width of measured PSFs, which is a complicated function of pinhole geometry, system blur, vignetting and 3D source location, an empirical exponential function of second-order polynomials was proposed, which relates the standard deviation of a Gauss-fit PSF to the 3D coordinates as

$$\sigma = \sigma_0(\alpha + \exp(-(\alpha_1 x_r + \alpha_2 {x_r}^2 + \beta_1 y_r + \beta_2 {y_r}^2 + \gamma_1 z_r + \gamma_2 {z_r}^2)) \quad (4.10)$$

where $x_r y_r z_r$ is a slightly translated version of the x'''y'''z''' system to have the origin aligned with the central ray. The presence of factor α is the result of finite pinhole diameter. This function is applied to both x-direction standard deviation and y-direction standard deviation so there are two independent sets of parameters.

The correlation coefficient describes the standardized correlation between x and y of a Gaussian function and can be interpreted as the rotation of a 2D Gaussian distribution. It was observed, however, that correlation coefficients of the PSFs in FastSPECT III are distributed around 0 and have a small variance. So in this work, the correlation coefficients were assumed to be 0. That is, the spatial extents in coordinates u'' and v'' of the events in a PSF are assumed to be independent of each other.

4.4.6 System Characterization

To use the proposed system models for estimation of PSF response at any voxel in the FOV, all parameters in the system models need to be characterized or estimated. The pinhole projection model is based on the assumption of perfect pinhole geometry, so it's independent of sensitivity model and resolution model. The sensitivity and resolution of a PSF could be correlated, but they are fit with an independent sets of parameters. Therefore,

the parameters used in the pinhole projection model, sensitivity model, and resolution model were estimated separately.

All of the 1332 measured PSFs from each iQID camera, except the ones that have high risk to be truncated, were fit with Gaussian functions and used to characterize the large number of parameters. With a constrained, nonlinear optimization algorithm implemented in Matlab as *fmincon*, a minimum of the least-squares difference between the Gaussian-fit PSFs and the estimated PSFs can be found.

As discovered by Bequé et al. [2003], some parameters in the pinhole projection model can be correlated, although not all correlations cause trouble in image reconstruction. Local minima are expected to exist that could reduce the estimation accuracy and make it dependent on initial estimates. However, because FastSPECT III system is a stationary system with distances between components designed and fixed, we can provide very good initial estimates and small ranges for most parameters in the pinhole projection model. The additional *a priori* knowledge can help confine the solution to a region near the global minimum of the cost function.

Because sensitivity model and resolution model are empirical models, the accuracy of fitting in part depends on the flexibility of the mathematical models. We found that the proposed models can fit the sensitivity and resolution with high accuracy in the CFOV. Lower accuracy is expected for voxels close to a pinhole, where sensitivity can vary dramatically. However, as shown in evaluation section, the errors in sensitivity and resolution estimation have minimal effects on image reconstruction.

Table 4.2 lists all the parameters estimated in the system characterization.

Effective detection region	
u_0'', v_0''	Center of effective detection area
R	Radius of effective detection area
Pinhole projection model	
$\theta_x,\ \theta_y,\ \theta_z$	Rotation angle around x, y and z
m_u, m_v	Normal distance between xyz origin and central ray
e_u, e_v	Electronic shifts
f	Focal length
d	Distance from xyz origin to pinhole along central ray
p	Effective pixel size
n_u, n_v	Distance from uv origin to optical distortion center
k_1, k_2, k_3	Distortion model parameters
Sensitivity model	
s_x, s_y, s_z	Translation between $x_s y_s z_s$ origin to xyz origin
A_0	Initial guess of sensitivity at xyz origin
$a_1 - a_3, b_1 - b_3, c_1 - c_3$	Sensitivity model parameters
Resolution model	
r_x, r_y, r_z	Translation between $x_r y_r z_r$ origin to xyz origin
σ_0	Initial guess of standard deviation
$\alpha_0, \alpha_1, \alpha_2, \beta_1, \beta_2, \gamma_1, \gamma_2$	Resolution model parameters

Table 4.2: Summary description of estimated parameters in system models

To evaluate the accuracy of system characterization, statistical distributions of estimation errors of PSF centroid position, sensitivity, and standard deviation were generated as shown in Figure 4.25. The centroid-position estimation has an average error of ~1pixel that rarely falls beyond 2 pixels. The sensitivity has an average of <10% estimation error and the spatial-widths are estimated with an average of <10% error. A distribution of the PSF correlation coefficients also validated the prior assumption that the PSFs are independently distributed along the u'' and v'' axes.

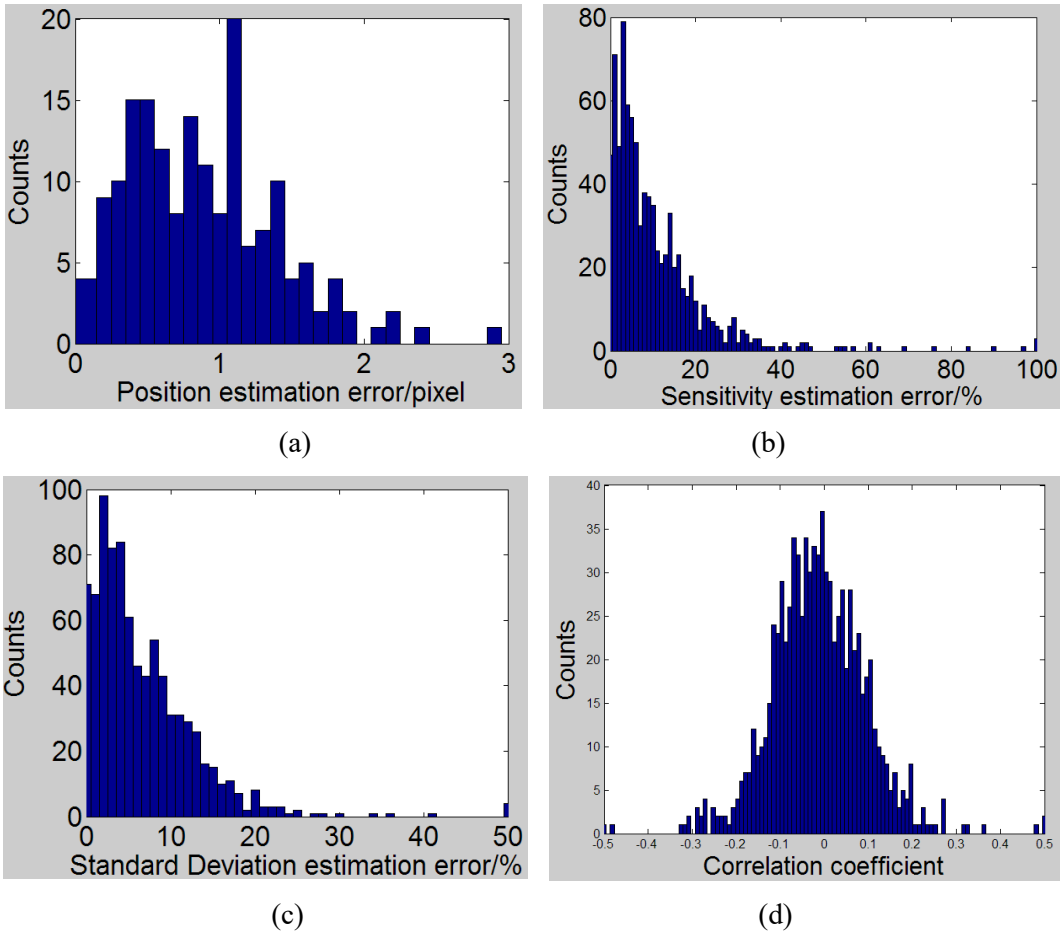

Figure 4.25: Statistical distributions of estimation errors of centroid position (a), sensitivity (b) and standard deviation (c) of PSFs. (d) Distribution of correlation coefficients of Gauss-fit PSFs.

To compare the Gaussian-fit PSFs and estimated PSFs using the parameterized system models, two examples are shown in Figure 4.26. Example (a) shows the PSF comparison for a voxel inside the CFOV. From the horizontal and vertical cross profiles, we can see the 2D projection location, sensitivity and resolution are all estimated with high accuracy. Example (b) shows the worst-case scenario for a voxel close to a pinhole, which demonstrates some sensitivity error as expected. In conclusion, high-accuracy interpolation is achieved for the CFOV where high-precision calibration data are available from the hybrid scan. Larger errors are observed when the voxel is close to the pinhole and the dramatic sensitivity variation cannot be fit accurately with the empirical sensitivity model.

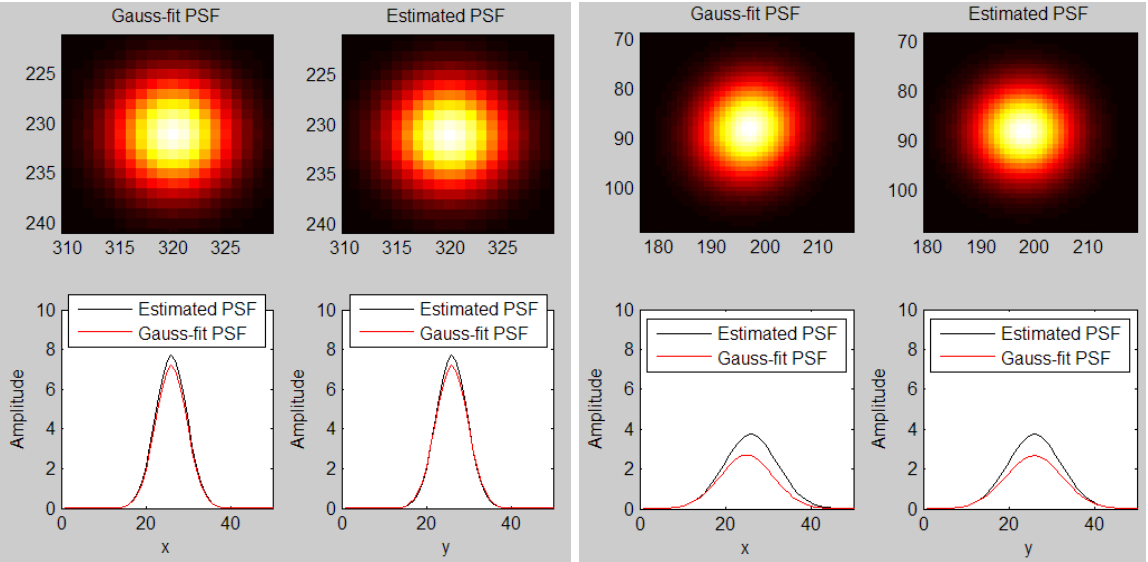

(a) (b)

Figure 4.26: (a) Gauss-fit PSF vs. Estimated PSF for a source position in CFOV, horizontal and vertical profiles for both PSFs are also plotted. (b) Gauss-fit PSF vs. Estimated PSF for a source position close to edge of TFOV, horizontal and vertical profiles for both PSFs are also plotted.

With the fully-characterized system models, PSFs corresponding to any source locations in the FOV can be estimated with the interpolation of the six Gaussian parameters. An H matrix with any voxel size and total dimension can then be calculated and used for image reconstruction.

4.5 Multi-bed-position MLEM

To be able to reconstruct a whole-body image of the mouse, a GPU-based iterative multi-bed-position MLEM algorithm is used, which was implemented by Luca Caucci at the Center for Gamma-Ray Imaging. A similar algorithm was also used in the U-SPECT I system to expand the FOV. [Beekman and Vastenhouw 2004] Before applying the algorithm, a series of projection images corresponding to multiple bed positions are acquired. In accordance with the spatial relationships between the multiple bed positions, a large system matrix is constructed from multiple shifted copies of the calibrated H matrix. Then the iterative MLEM is applied to reconstruct all voxels of the object simultaneously. Figure 4.27 illustrates the multi-bed-position MLEM algorithm with a 10-voxel object and 3 sets of projection images from three bed positions. Each set of projection images is generated from 5 voxels of the object. A large system matrix H_Σ contains 3 sets of H matrix for the 3 bed positions. An iterative MLEM is then used to reconstruct the 10 voxels of the object from the concatenated projection images and constructed system matrix H_Σ.

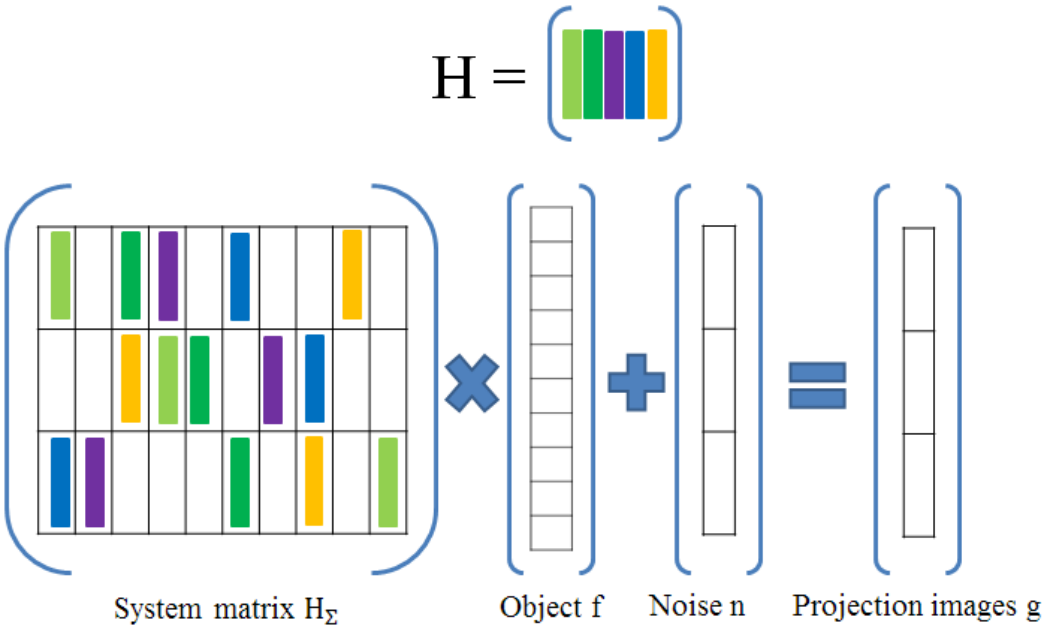

Figure 4.27: Illustration of the multi-bed-positions MLEM algorithm for image reconstruction.

4.6 Performance Evaluation

To evaluate the 3D imaging performance of the combination of the advanced frame-parsing algorithm, the thick columnar CsI(Tl) scintillators, and especially the new system calibration method, both phantoms and mice were imaged on FastSPECT III. Reconstructed images using multi-bed-position MLEM demonstrated high system resolution.

4.6.1 Phantom Imaging

To demonstrate the current resolution of FastSPECT III, the same high-resolution micro-Derenzo phantom [VANDERWILT] that was originally used to evaluate the resolution performance of FastSPECT III was again used. [Miller et al. 2012c] ~2mCi liquid ^{99m}Tc was drawn into the micro-bores of the phantom through capillary action. The smaller bores were easily filled while the larger ones were only partially filled. A total of six sets of projection images were acquired with two different approaches. The first approach was to take one set of projection images with a 15-minutes acquisition with the phantom was placed at the center of CFOV. The other approach was to place the phantom at five different locations with overlap between each position, and acquire five sets of projection images, each with 3-minutes exposure. Figure 4.28 illustrates both image acquisition approaches. The one-circle and five-circle symbols on the upper-right corner of the reconstructed images in Figure 4.29 represent the first and the second image acquisition approaches. For reconstructing the images acquired through the first approach, regular MLEM reconstruction algorithm and a cubic H matrix acquired through the original calibration method with 77^3 voxels (0.214 mm voxels and 15 mm in each dimension) were used. Reconstructed images with 100 and 30 iterations are shown in (b) and (d) of Figure 4.29. For reconstructing the images acquired through the second approach, the multi-bed-position MLEM reconstruction algorithm and a new cubic H matrix acquired through the new system calibration method with 126^3 voxels (0.214mm voxel and 26.8mm in each dimension) were used. The reconstructed image with 30 iterations is shown in (c) of Figure 4.29.

Figure 4.28: Projection images acquisition approaches. Left: 15-minutes acquisition with the phantom at the center of CFOV. Right: 15-minutes total acquisition with phantom at five different positions, each with 3-minutes acquisition.

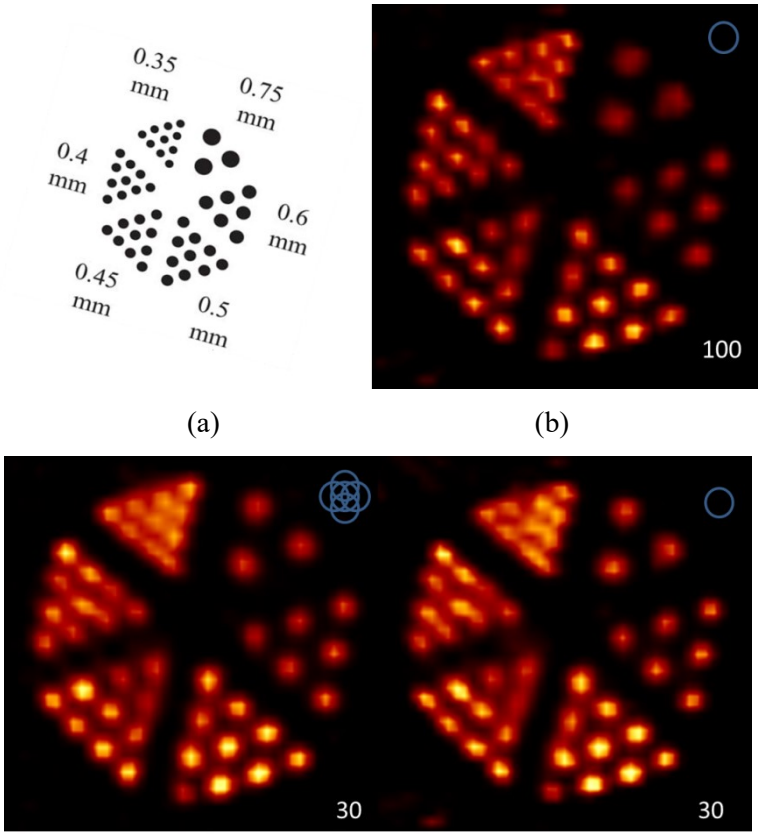

Figure 4.29: Image reconstructions of high-resolution micro-Derenzo phantom. (a) The configurations of the micro-resolution phantom. Bore sizes range from Ø 0.35mm to Ø0.75mm with spacing equal to the bore diameter. (b) and (d): MLEM reconstructed images of the phantom at the center of CFOV with 100 and 30 iterations, respectively. The original system calibration method was used. Acquired H matrix has 77×77×77 voxels (0.214 mm voxel size). (c) Reconstructed image of the phantom placed at five different positions with multi-bed-position MLEM and 30 iterations. The new system calibration method was used and the acquired H matrix had 126×126×126 voxels (0.214 mm voxel size).

From the reconstruction images, we subjectively judge that the advanced FastSPECT III offers better than 350 μm spatial resolution. The multi-bed-position MLEM with the new calibration method provides as high resolution as the original calibration method.

4.6.2 Mouse Imaging

To demonstrate the full-body mouse imaging capability, a bone scan was performed for a mouse on FastSPECT III. Approximately 5mCi ^{99m}Tc-MDP was injected via tail vein into the mouse. This tracer is primarily absorbed by active bone reformation. Three hours after the injection, the bladder of the mouse was emptied to reduce the effect on image quality, and the imaging started with a helical scan. With the head of the mouse positioned at the center of CFOV as the first position, the scan consisted of a total of 13 positions on a helical trajectory as shown in Figure 4.30. The axial translation step was ~7mm (33 0.214mm voxels) and the vertical translation step was ~1.5mm (7 0.214 voxels). The acquisition started with 10-minutes for the first position and ended up with 13-minutes for the last position as times were scaled to compensate for source decay. With the new calibration matrix, the full-body mouse image was reconstructed with 30-iterations of multi-bed-position MLEM as shown in Figure 4.31. To compare the resolution performance of FastSPECT II and FastSPECT III, the same mouse was imaged on FastSPECT II following the same helical scan routine immediately after finishing on FastSPECT III. Since FastSPECT II has much higher sensitivity, the starting acquisition time was set to 6 minutes. The same multi-bed-positions MLEM was again used to reconstruct a full-body image of the mouse as shown in Figure 4.31.

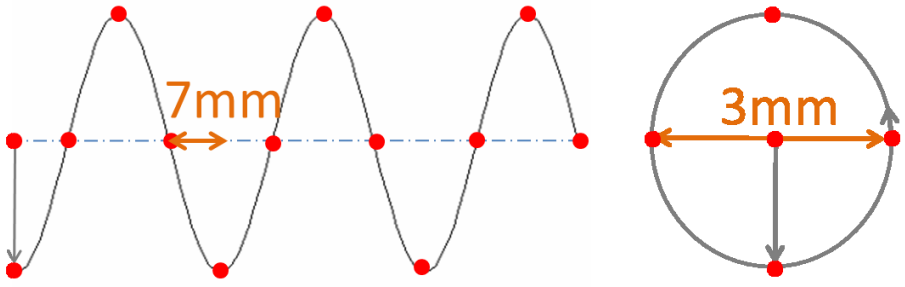

Figure 4.30: Helical scan with 13 positions for data acquisition. Axial translation step is ~7mm and vertical translation step is ~1.5mm.

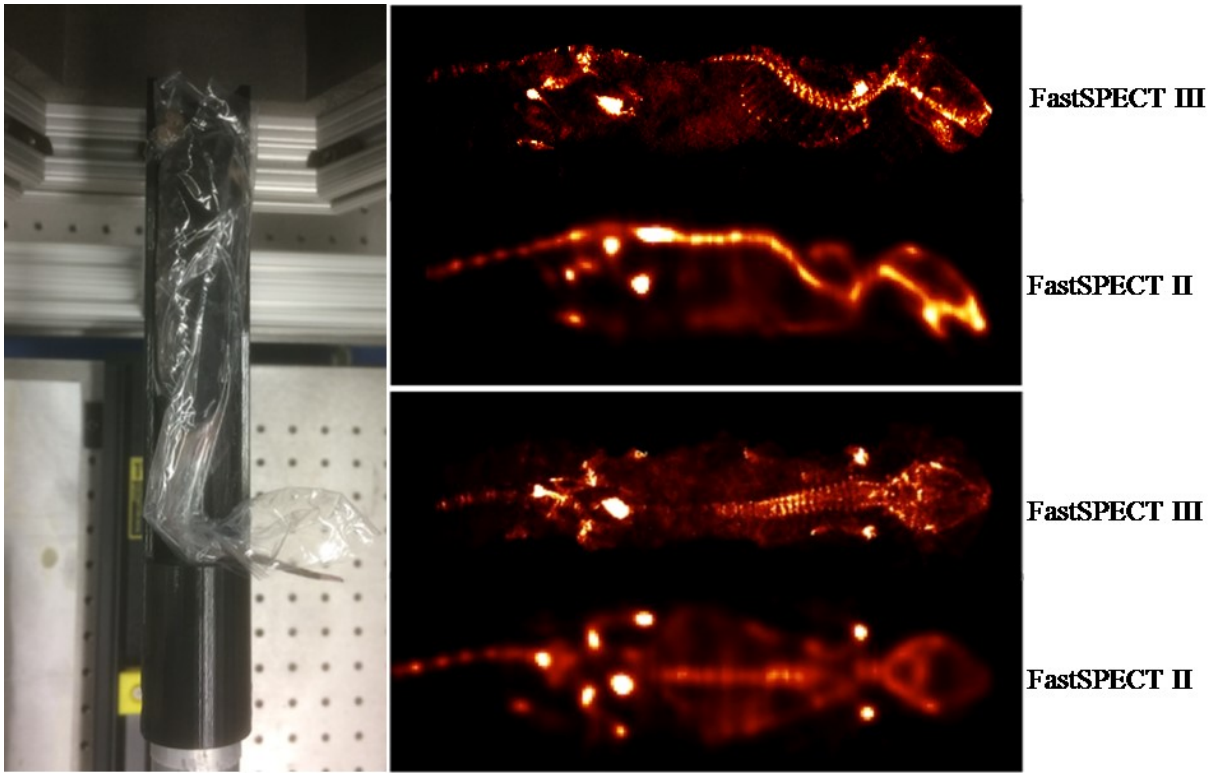

Figure 4.31: Mouse ^{99m}Tc-MDP bone-scan study. Left: a picture of the mouse with ~5mCi ^{99m}Tc-MDP injected three-hours earlier and bladder emptied. Right: Reconstructed images of the mouse acquired from both FastSPECT III (upper one) and FastSPECT II (lower one). 30-iterations multi-bed-position MLEM is used for images reconstruction. Side view (Top) and top view (Bottom) of the 3D reconstructed images demonstrated superior resolution of FastSPECT III over FastSPECT II.

The reconstructed images of the mouse bone structure acquired from FastSPECT III show superior resolution performance over FastSPECT II. The bone structure of the skull, spine, rib, shoulders, hips, tail and legs can be clearly identified in the images. The nose tip, nasal turbinates, inner spine, and rib tips all demonstrate higher activity, since these regions have more active bone reformation and thus show greater metabolic activity and MDP absorption.

To demonstrate soft tissue imaging for a living mouse, heart perfusion sudy was also performed on FastSPECT III. About 5mCi ^{99m}Tc-Sestamibi was injected via tail vein into the mouse and the imaging started ~100 minutes after the injection. The scan consisted of a total of 12 positions on a helical trajectory with ~2.6 mm (12 0.214-mm voxels) axial translation steps and ~1.9 mm (9 0.214-mm voxels) vertical translation steps. The

acquisition time for each position was 5 minutes and the total acquisition time was about 60-minutes, during which time the mouse was kept in an anesthetized state. With the new calibration matrix, the full-body mouse image was reconstructed with 30-iterations of multi-bed-position MLEM. The reconstructed images of the mouse heart in 1-mm slices in different planes are shown in Figure 4.32. An anatomy figure of a mouse heart is also shown in Figure 4.33 for interpretation of the reconstructed images.

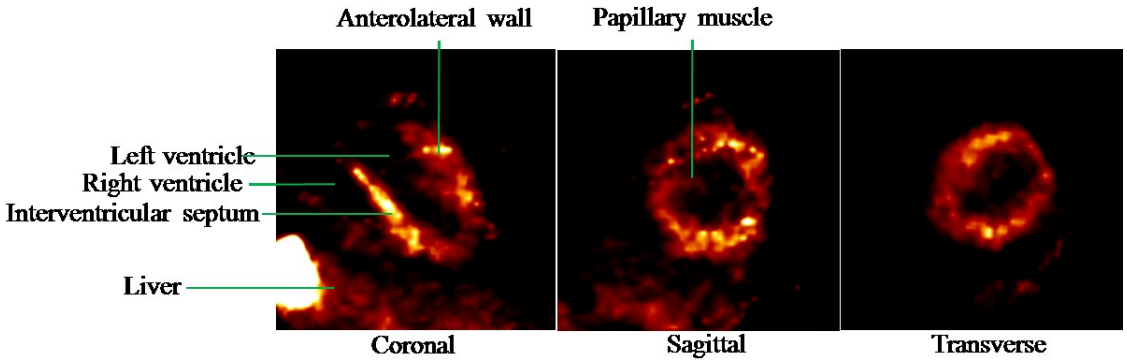

Figure 4.32: 1-mm-slices of the reconstructed mouse heart in coronal, sagittal and transverse planes.

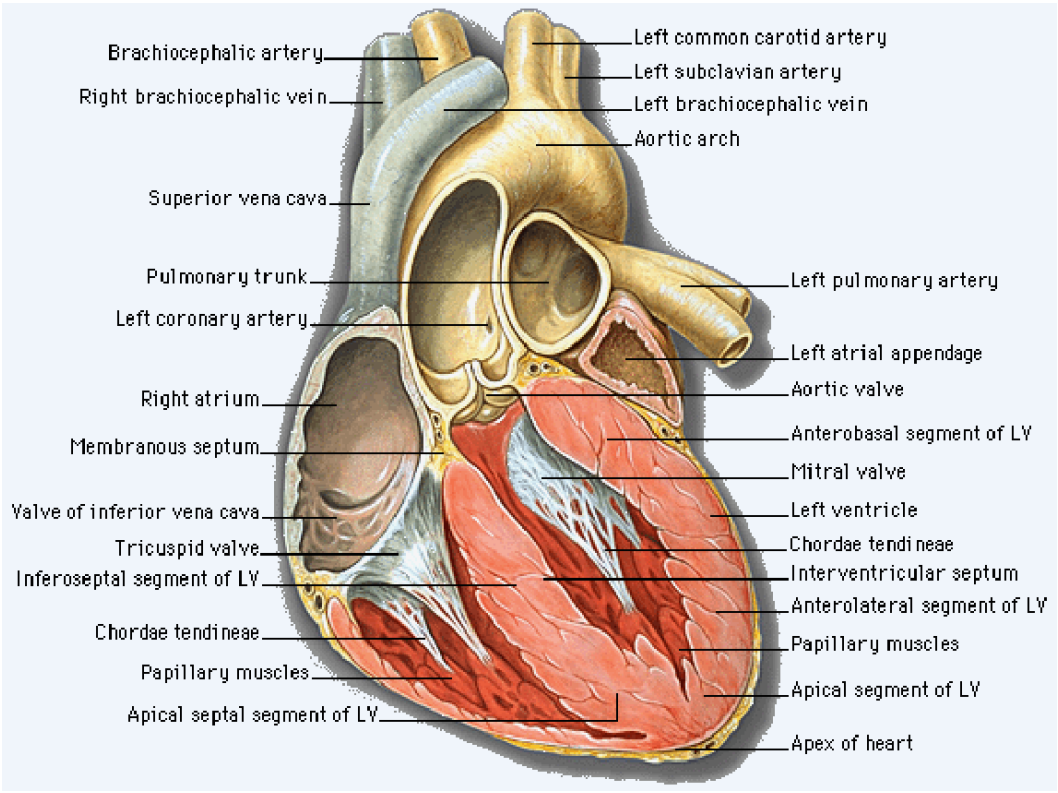

Figure 4.33 [Anatomy]: The mouse heart anatomy.

The mouse heart has been successfully reconstructed with high resolution. The anterolateral wall, left ventricle, right ventricle, and interventricular septum are all visible in the image. There is also an indication of the papillary muscle protruding into the left ventricle. Due to the fast beating of the mouse heart and dynamic biological processes, the radiotracers may not be uniformly distributed in the heart, which was also demonstrated in heart perfusion images of a rat as shown in Figure 4.34.

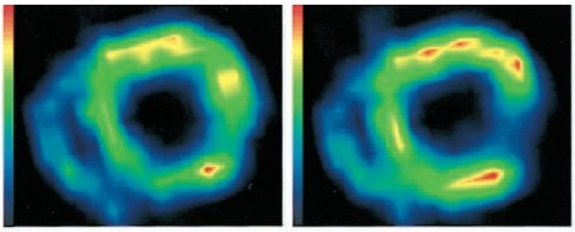

Figure 4.34 [Liu et al. 2002]: Heart perfusion images of a rat acquired from FASTSPECT system showing similar spatially-varying radiotracer distributions.

4.7 Conclusions

In this chapter, many advances have been achieved for the FastSPECT III system, which greatly improve the system's capabilities and performance. An advanced frame-parsing algorithm was proposed and implemented on FastSPECT III, which was able to effectively and statistically remove the central-spot background noise originating from the XX1332 image intensifiers while maintaining high-speed real-time data-processing by the acquisition software. A 1.65-mm-thick new columnar CsI(Tl) scintillator was tested in terms of spatial resolution, sensitivity and depth-of-interaction, and was installed on all iQID cameras in FastSPECT III. A comparison study of the new scintillator versus the originally-equipped 0.45mm columnar CsI(Tl) scintillator demonstrated ~3-times higher sensitivity and very good spatial resolution (~0.3mm FWHM). A new system calibration method was also proposed for FastSPECT III. With a novel hybrid multi-gridded scan, high-precision calibration data in a large volume can be achieved. Physics-based and empirical system models were proposed and fully characterized that are able to provide an H matrix with any voxel size and dimensions for image reconstruction. Finally, both resolution phantoms and mice were imaged. The reconstructed phantom demonstrated better than 0.35mm spatial resolution, and the new system calibration method provided as high resolution as good as the the original system-calibration method. A mouse bone scan was performed on FastSPECT

III with helical scanning and reconstructed with both the new calibration matrix and a multi-bed-position MLEM algorithm. Results demonstrated superior spatial resolution over FastSPECT II. Finally a heart perfusion study of a living mouse was also performed on FastSPECT III, demonstrating high-resolution reconstruction of the mouse heart, further validating the effectiveness of the new system calibration method. Originally envisioned as an I-125 (~30keV) mouse imager, the FastSPECT III system was impractical for ^{99m}Tc and other >100keV gamma emitters. With all of the advances, FastSPECT III is now able to provide full-body high-resolution mouse images with more conventional radiotracers for general preclinical studies.

CHAPTER 5

LA-IQID: A HIGH-RESOLUTION CLINICAL GAMMA CAMERA

After successfully advancing the iQID technology in preclinical imaging applications, we have achieved further advances, described in this chapter, with the development of the first large-area iQID-based dedicated clinical gamma camera, i.e. LA-iQID. Key features of LA-iQID include sub-mm ultra-high spatial resolution, 188 mm×188 mm large detection area, mobility and portability. Although developed for human lymphatic system imaging, LA-iQID can also be applied to other dedicated clinical imaging tasks such as mammoscintigraphy. There are many challenges in translating a laboratory-developed technology to clinical applications. This chapter will introduce the novel architecture, component design, system integration, data acquisition, calibration, and performance evaluation of the LA-iQID camera.

5.1 Lymphoscintigraphy

The lymphatic system is a second circulatory system in the body that operates in parallel with the blood circulation system, as shown in Figure 5.1. Consisting of lymphatic capillaries, vessels and nodes, the lymphatic system removes interstitial fluid from tissues and maintains tissue interstitial pressure, and assists with immune response by transporting antigen-presenting cells (APCs) and white blood cells when presented with infection or inflammation. Disseminating tumor cells from many different types of cancers, such as breast cancer, melanoma and prostate cancer, are also transported through the lymphatic system in early metastases. Malfunction of the lymphatic system can cause lymphedema and local immuno-compromise, both of which result in significant morbidity. The significance of the lymphatic system to a variety of pathological processes motivated the development of imaging techniques to visualize its anatomy and function. [Murtaza et al. 2014, Sevick-Muraca et al. 2014, Munn and Padera 2014] Most imaging modalities depend on injected tracers that are transported in the lymphatic vessels and absorbed by the lymphatic network, such as optical imaging with blue dye or lymphoscintigraphy with radiotracers.

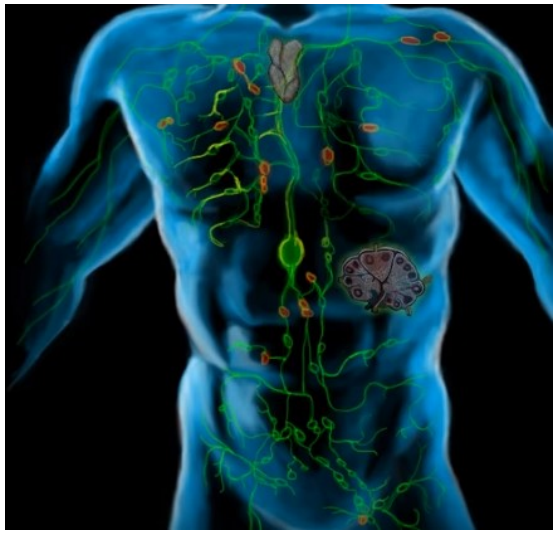

Figure 5.1: Human lymphatic system with lymphatic capillary, lymphatic vessels and lymph nodes.

As with other clinical scintigraphy technologies, lymphoscintigraphy starts with injection of ^{99m}Tc-labeled radiopharmaceuticals as imaging tracers. Typical tracers include ^{99m}Tc-labeled human serum albumin, ^{99m}Tc-labeled dextran, and ^{99m}Tc-labeled sulfur colloid. As soon as the injection is finished, a gamma camera can be used to acquire dynamic planar-projection images as the tracers flow through the lymphatic system. When the tracers are absorbed throughout the lymphatic network, static images reflecting the anatomy and function of lymphatic system can be acquired. An important application of lymphoscintigraphy is the identification of lymph nodes, especially sentinel lymph nodes (SLN), for evaluation of early tumor metastasis. [Niikura et al. 2005, Ozmen et al. 2006, Wei et al. 2015, Moslehi et al. 2015] As the first regional lymph node that drains the lymph from the primary tumor, the SLN is potentially the first node to receive metastatic tumor cells. Being able to detect the presence or absence of metastatic cells has prognostic implications for patients with cancer. Other applications of lymphoscintigraphy include the diagnosis of lymphedema [Yuan et al. 2006] and mapping of lymphatic drainage [Seo et al. 2011]. This has been reported to be a reliable, feasible and easy-to-carry-out study.

Although commonly used in the clinic, traditional lymphoscintigraphy has been reported to suffer from poor spatial resolution (1-2cm), which does not allow clear identification of lymphatic vessels or accurate estimation of lymph node locations. [Munn and Padera 2014,

Sevick-Muraca et al. 2014, Murtaza et al. 2014] To improve the performance of lymphoscintigraphy, several portable dedicated gamma cameras have been developed recently. [Fernández et al. 2004, Bugby et al. 2014, Olcott et al. 2014] The resolution performance is also improved to 3-4mm. For example, Trotta et al. [2007] developed a portable gamma camera with a CsI(Tl) crystal, integrated square parallel-hole collimator, and H8500 PSPMT to achieve 3.32mm system resolution at a 1 cm distance over a FOV of 49 mm × 49 mm. Sánchez et al. [2004] developed a portable gamma camera with a CsI(Na) crystal and R2486 PSPMT to achieve a ~3 mm system resolution at 2 cm distance over a 46 mm-diameter FOV with a high-resolution parallel-hole collimator. Knoll et al. [2014] developed a hand-held gamma camera with cadmium-zinc-telluride (CZT) and LEHR parallel-hole collimator to achieve a system resolution of ~3.8 mm at 2.5 cm distance over a FOV of 40 mm × 40 mm. A major disadvantage of these dedicated gamma cameras, however, is the small FOV, which usually requires prior information of the SLN location before the camera can be used. For a dedicated clinical gamma camera, ~20 cm × 20 cm FOV would be ideal. In addition, the average size of lymph nodes is ~4 mm, with a large variability. As a result, a 3 – 4 mm resolution can only provide limited localization accuracy relative to the size of the lymph nodes.

A novel high-resolution Large-Area iQID (LA-iQID) gamma camera has been developed to greatly improve the spatial resolution while maintaining a large FOV, thus providing superior image quality for lymphatic-drainage mapping and lymph-node localization. By coupling large-magnification-fiber-optic (FO) taper between an array of image intensifiers and a columnar scintillator, the iQID effective detection area has been greatly increased to 188 mm × 188 mm. Equipped with a custom low-energy, ultra-high-resolution (LEUHR) parallel-hole collimator manufactured with photochemical etching technology by [Tecomet, Inc], the LA-iQID is able to provide sub-mm planar resolution. This chapter will introduce the LA-iQID camera in all aspects, including system architecture, component design, system integration, data acquisition, camera calibration, and performance evaluation.

5.2 Large-Area IQID Configurations

In recent advances of iQID cameras, large-magnification FO tapers have been used to increase the detection area, which have higher NA and thus better light-collection efficiency compared to an optical lens coupling. [Miller et al. 2012a, 2015; Barber et al. 2013] The maximum achieved FOV through this method, however, is 115 mm diameter, which was accomplished by coupling a 3:1 FO taper to a 40mm image intensifier. Further expansion of the FOV is limited by the high-cost and manufacturing challenges of creating either larger-area image intensifiers or higher-magnification FO tapers. To work around this limitation, four identical iQID cameras are tiled together in the LA-iQID, each with its own square large-magnification FO taper and a secondary round smaller-magnification FO taper coupled to the image intensifier. Using this configuration, lower-cost 25mm-diameter image intensifiers can be used while the FOV of each iQID camera can be increased from 25 mm to ~10 cm. The total effective FOV after tiling is increased to 188 mm × 188 mm. A custom flat-panel columnar CsI(Tl) scintillator and the ultra-high-resolution parallel-hole collimator are then integrated to become the front of the LA-iQID. Clocks can be synchronized across all four iQID cameras, and data simultaneously acquired and processed. The total pixel resolution is 4 MP with an effective pixel size of ~120 μm. Figure 5.2 shows a SOLIDWORKS rendering of the configuration of LA-iQID camera before the scintillator and collimator were integrated.

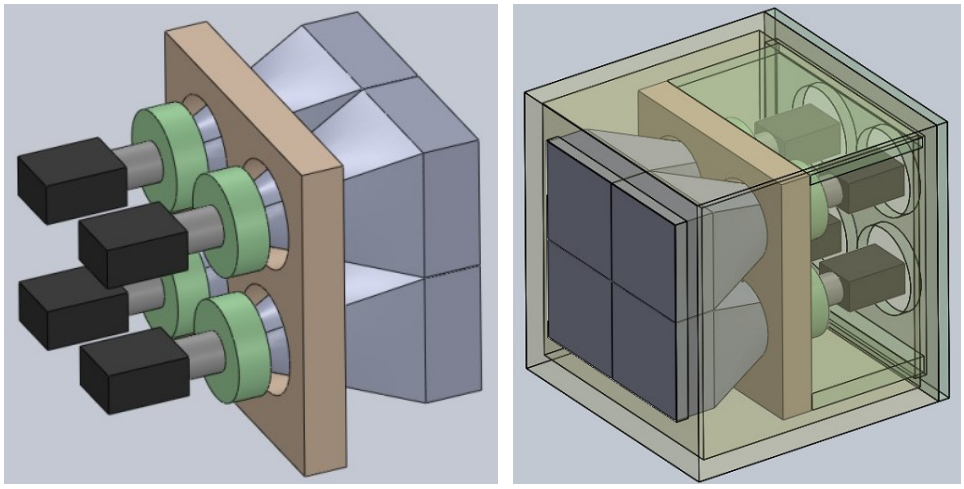

Figure 5.2: LA-iQID configurations with four identical iQID cameras tiled together to form a large detection area.

5.2.1 Flat-Panel Columnar CsI(Tl) Scintillator

The gamma-ray converter used on the LA-iQID is a 1-mm-thick GPXS100 columnar CsI(Tl) scintillator on 0.5mm aluminum substrate manufactured by [Hamamatsu]. The effective usable area is 193 mm × 193 mm with total area of 199 mm × 199 mm. The light output is 344% higher than the conventional phosphor screen (Lanex-R). A resolution of 3 lp/mm with 21.8% contrast is provided by the scintillator with a sensitivity of ~26.6% for 140keV photons. Figure 5.3 shows a photograph of the scintillator. Figure 5.4 shows the emission spectra of CsI scintillators with different dopants. Table 5.1 lists the major physical properties of CsI(Tl) scintillator that are relevant to this work.

Figure 5.3: The flat-panel 193 mm × 193 mm 1-mm-thick columnar CsI(Tl) scintillator.

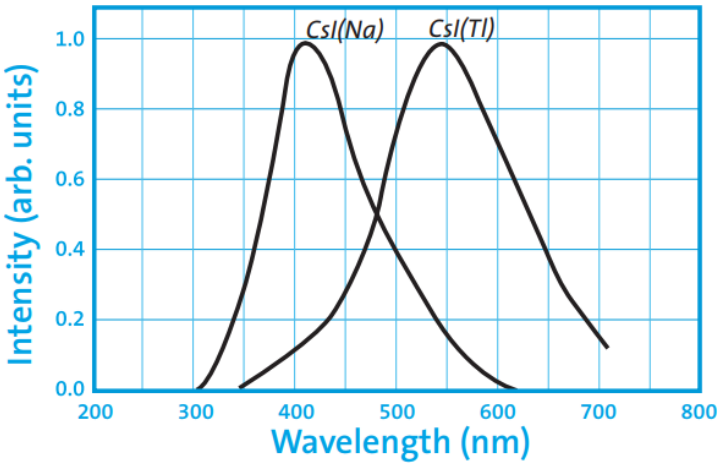

Figure 5.4: Normalized emission spectrum of CsI scintillator with Na and Tl dopings.

CsI(Tl) Scintillator	
Density (g/cm^3)	4.51
Peak Emission Wavelength (nm)	550
Refractive Index @ Peak Wavelength	1.79
Primary Decay Time (ns)	1000
Light Yield (photons/keV)	54

Table 5.1: Physical properties of CsI(Tl) scintillator.

5.2.2 Fiber-Optic Tapers

For each iQID camera, two FO tapers manufactured by [INCOM] are used sequentially for coupling the scintillator to the entrance face of the image intensifier. The first taper has a square entrance with 94 mm × 94 mm dimensions, and a round exit, with a 3.6:1 demagnification. This taper is surplused from a legacy synchrotron x-ray diffraction detector, called Quantum4, so detailed specifications are not available. However, some specifications of similar products from INCOM are shown in Table 5.2. The spectral transmission at 25 mm thickness is shown in Figure 5.5. The second taper is a custom taper with 1.6:1 demagnification and a 44.19mm diameter usable large-end area. Figure 5.6 and Table 5.3 show the detailed design drawing and other specifications of this secondary taper. With both tapers in place, the total demagnification is 5.76:1, which provides a 16.3 mm × 16.3 mm square minified exit image (23 mm-diameter) that fits into the 25 mm-diameter entrance window of the image intensifier.

INCOM Tapers with >100mm Diameter (BLS59-18)	
Core Index	1.8
Clad Index	1.49
Theoretical Core Percentage (%)	75
Fiber Size (μm)	18
Density (g/cm^3)	4.04

Table 5.2: Specifications of INCOM large-diameter tapers.

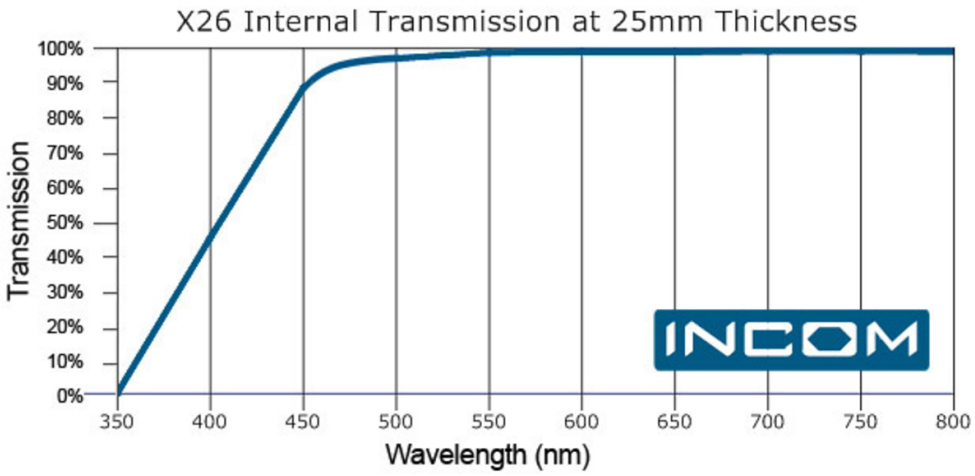

Figure 5.5: Spectral transmission of INCOM large-diameter FO tapers at 25mm thickness.

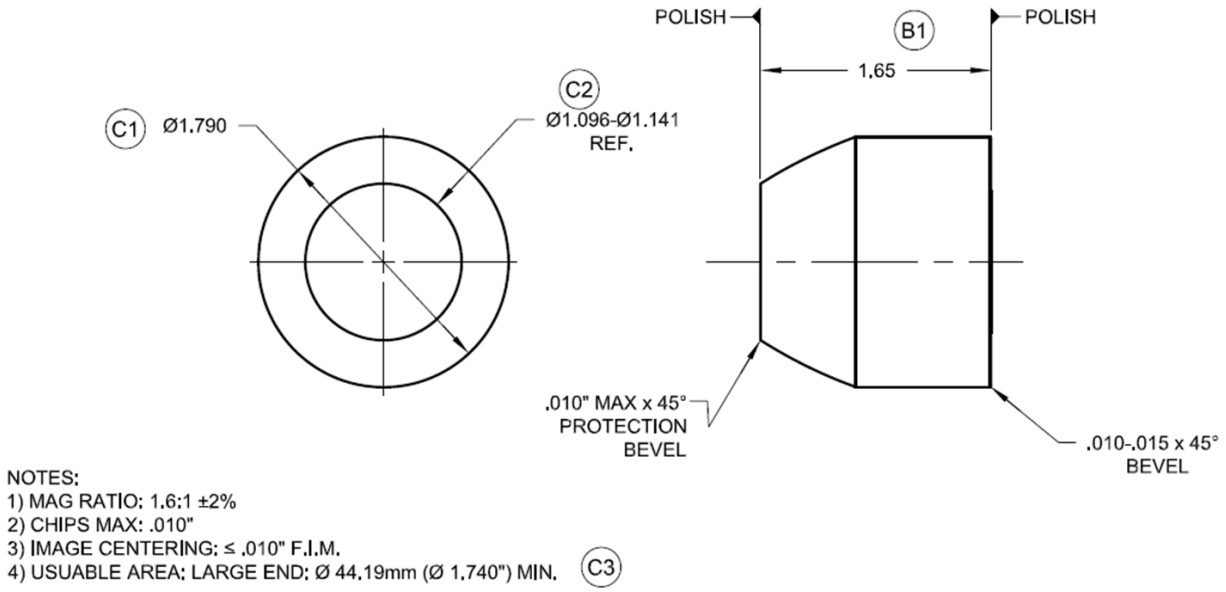

Figure 5.6: Design drawing of the smaller-diameter FO taper.

45mm Fiber-Optic Taper (Plano/Plano)	
Large End Diameter (mm)	45.46mm Dia. (1.790”)
Small End Diameter (mm)	28.39mm Dia. (1.118”)
Length (mm)	41.9mm (1.650”)
Usable Large End Diameter (mm)	44.19mm dia. (1.740”)
Magnification	1.6:1 +/- 2%
Material	Block Press BLS59-6
Shear Distortion	.004” Max
Gross Distortion Max	2% over usable area

Table 5.3: Specification of the smaller-diameter customized FO taper.

5.2.3 High-Gain Image Intensifiers

The image intensifier used for each iQID quadrant is a 25mm-diameter 2-MCP image intensifier manufactured by [ProxiVision GmbH], as shown in Figure 5.7. With a bialkali photocathode deposited on a fiber-optic entrance faceplate, thus providing high-resolution light detection, the image intensifier features a low dark-emission rate of 15 electrons/cm^2/sec as shown in Table 5.4 and ~12.4% quantum efficiency at 500nm. The 2 MCPs can provide electron gain of up to 10^6 el/el at 1800V bias voltage as shown in Figure 5.8. A Gd_2O_2S:Tb (P43) exit phosphor screen is also deposited on a fiber-optic faceplate to transfer amplified electron energy back into visible light with minimal light spread. The P43 phosphor screen also features high light-emission efficiency at a peak emission wavelength of 545 nm. The total optical gain of the 2-MCP image intensifier is up to 1.2×10^6 W/W at 480nm wavelength, and the limiting resolution is 24-28 lp/mm. [ProxiVision]

Figure 5.7: The 2-MCP image intensifier used in LA-iQID manufactured by ProxiVision in its 3D-printed custom housing.

Photocathode / Substrate	Code	Composition	Dark Emission Rate (Electrons/cm^2/sec)
Advanced Solar Blind / Quartz	C	CsTe	3
Bialkali / Quartz	B	K_2SbCs	15
UV Enhanced S 20 / Quartz	T	$(Na_2KSb)Cs$	500
S 20 / Quartz	Q	$(Na_2KSb)Cs$	1500

Table 5.4 [ProxiVision]: Dark emission rates of different photocathode materials.

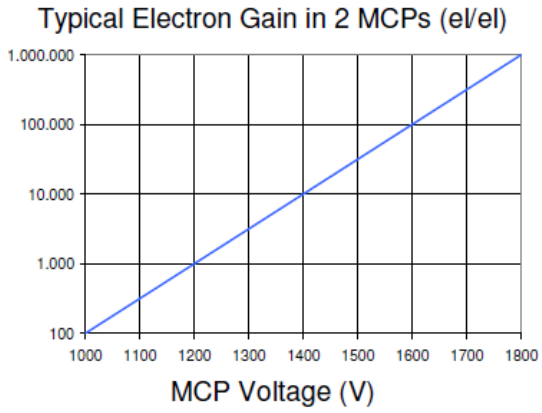

Figure 5.8 [ProxiVision]: Typical electron gains of 2 MCPs as a function of bias voltage.

5.2.4 Relay Optics

The relay lens used in each iQID camera is a 6mm, F/1.2, Fujinon DF6HA-1B lens, as shown in Figure 5.9. [Fujinon] Designed to support up to 1.5 megapixel sensors, this C-mount lens can be adapted to our 1 megapixel sensor as shown in the next section. The 6 mm short focal length also allows a compact form for the iQID cameras. Table 5.5 lists the optical specifications of this lens.

Figure 5.9 [Fujinon]: The 6 mm, F/1.2, Fujinon DF6HA-1B lens.

Fujinon DF6HA-1B Lens Specifications		
Focal Length (mm)		6
Iris Range		F1.2-F16
Operation	Focus	Manual
	Iris	Manual
Angle of View (H×V)	1/2”	56°09′×43°36′
	1/3”	43°36′×33°24′
	1/4”	33°24′×25°22′
Focusing Range (from front of the lens) (m)		0.1-∞
Back Focal Distance (in air) (mm)		11.4
Exit Pupil Position (from image plane) (mm)		-46
Filter Thread (mm)		M27×0.5
Mount		C
Mass (g)		55

Table 5.5 [Fujinon]: Specifications of Fujinon DF6HA-1B lens.

5.2.5 High-Resolution CCD Sensor

The CCD sensor used in LA-iQID is a Grasshopper Express 1024×1024 (5.5μm×5.5μm pixel size) monochrome Kodak KAI-01050 CCD sensor manufactured by Point Grey Research, Inc. [FLIR] The maximum frame rate is 70 fps in 8-bit A/D mode. Data transmission is accomplished with a 9-pin FireWire 1394b bus supporting a bandwidth of up to 800 Mbps. The CCD camera can be operated at temperatures between 0 ^{o}C to 40 ^{o}C with no external cooling system. The housing schematics and specifications are shown in Figure 5.10.

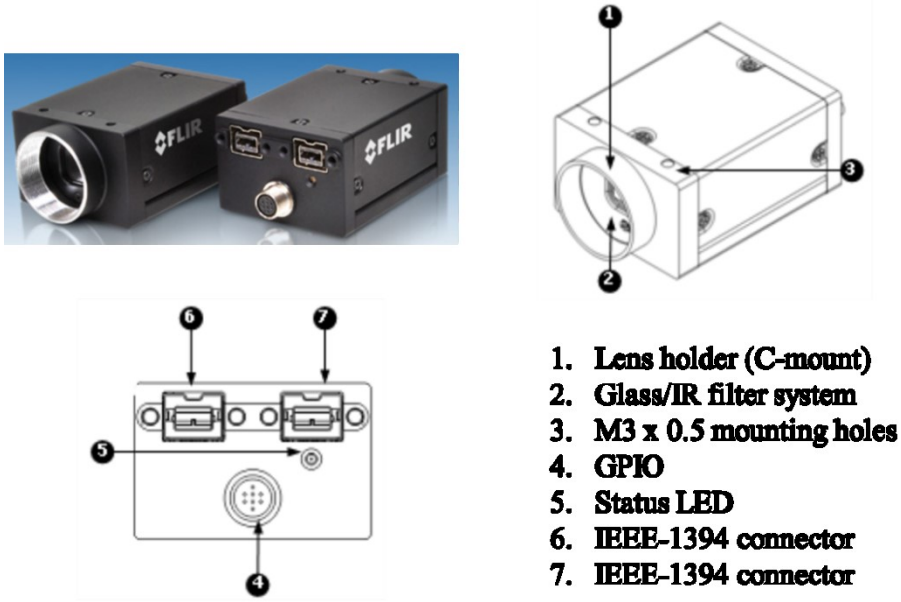

Figure 5.10: Grasshopper Express CCD schematics with physical descriptions.

5.3 LEUHR Parallel-Hole Collimator Design

Because iQID cameras can provide high intrinsic resolution of a few hundred microns or less, the gamma-ray imaging optics such as pinhole and parallel-hole collimator are usually the elements limiting the system's resolution performance. It has been demonstrated that high-resolution collimators, even at substantial cost in sensitivity, can provide significant improvements in clinical imaging tasks. [Mueller et al. 1986] Therefore, to provide high-resolution performance while maintaining a 1:1 imaging magnification for the LA-iQID, a LEUHR parallel-hole collimator was designed and optimized based on the tradeoff between performance and cost. Both analytical solutions and Monte Carlo validation were used in the design. Finally, the photochemical etching and laminating technique was used for manufacture of the collimator by [Tecomet].

5.3.1 Analytical Design

There are many analytical design and optimization methods for parallel-hole collimators in the literature. [Gerber and Miller 1974, Causer 1974, Smith et al. 2003] This work used a similar design approach as that employed by Keller [1968].

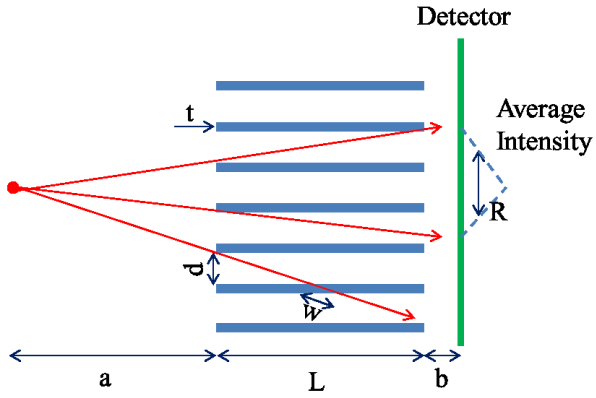

Figure 5.11: Parallel-hole collimator imaging geometry.

As shown in Figure 5.11, the FWHM of the average point source projection intensity (the PSF) is denoted as R, and is given by

$$\mathrm{R} = \mathrm{d}(\mathrm{a} + L_e + b)/L_e \,, \tag{5.1}$$

where d is the diameter of the bore, a and b are the source to collimator and collimator to detector distances. L_e is the effective bore length that is shorter than the physical length due to gamma-ray penetration through the septal material and is approximated as

$$L_e = L - \frac{2}{\mu} \,, \tag{5.2}$$

where μ is the total attenuation coefficient of the collimator material. [Mather 1957] The maximum penetration probability p from one bore to another can be calculated as

$$\mathrm{p} = \exp(-\mu \mathrm{w}) \,, \tag{5.3}$$

and is expected to be below 5% for low-resolution collimators. Since we need a high-resolution collimator, 1% penetration probability is aimed for. The sensitivity, defined as the ratio of image-forming gamma-rays and total emitted gamma-rays by the source, can be calculated as

$$\mathrm{S} = \left[\frac{\mathrm{k}d^2}{L_e(d+t)}\right]^2 \,, \tag{5.4}$$

where k is a constant shape factor determined by the bore shape and pattern, and t is the septal distance. [Anger 1967] When L>>2d+t in practical collimators, septal distance t can be calculated from the minimum penetration distance w, bore diameter d and bore length L as

$$t = \frac{2dw}{L-w} \quad . \tag{5.5}$$

With equations (5.1)-(5.5), we can set values for design parameters and study the performance of collimators with different designs. For lymphoscintigraphy applications, the objects to be imaged, i.e. lymphatic vessels and lymph nodes, are usually located just under the skin, so the object distance can be as small as 1-2 cm. For collimator material, Tungsten is typically preferred because of its high density, large atomic number, and hardness. To achieve high-resolution performance, a 1-mm FWHM resolution with 1% penetration or less is desired. Table 5.6 lists the design-parameter values for the new collimator.

Parameters	**Desired Value**
R (mm)	1
k	0.24 (Round bore in hexagonal pattern [Sorenson and Phelps 1987, Anger 1967])
a (mm)	20
b (mm)	1
μ (1/mm)	3.43 (for 140keV photon and Tungsten collimator material)

Table 5.6: Desired parameter values for designing the LEUHR parallel-hole collimator.

With a range parameter values, different design solutions with corresponding sensitivity performance can be generated as shown in Figure 5.12. It can be seen that as the bore length varies, bore diameter and septal distance of the designed collimator also vary accordingly to maintain the 1 mm resolution performance with 1% penetration. An optimal solution exists with ~9 mm bore length, 284 μm bore diameter, and 100 μm septal distance. However, the number of layers, which is determined by the ratio of bore length to septal distance as set by the photo-chemical etching technique, is ~90, which could easily make the cost unreasonably high, based on the pricing at the time of this dissertation. The cost can be reduced, but only with a sacrifice of sensitivity.

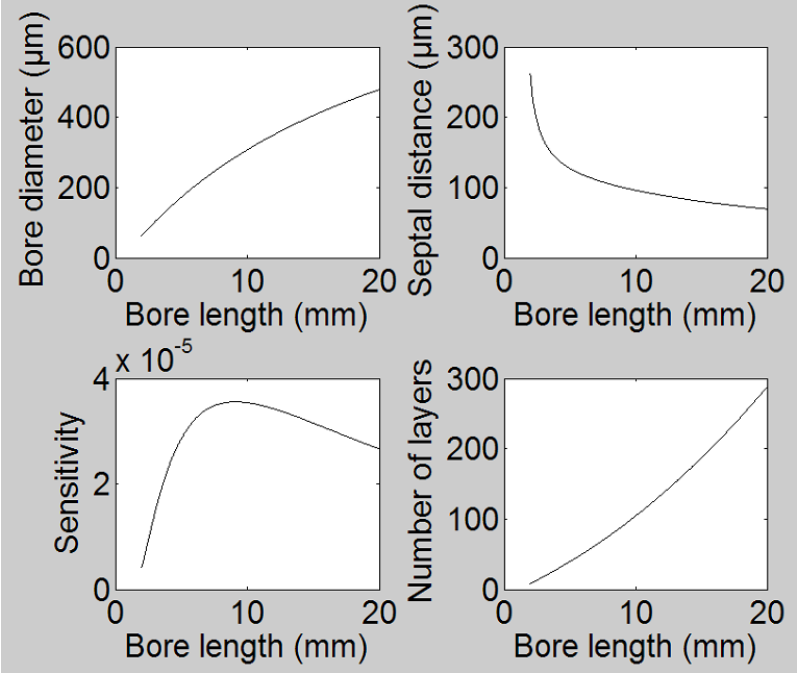

Figure 5.12: Efficiencies and number of layers of different collimator designs.

Finally, based on manufacturing details provided by Tecomet, a few design solutions were proposed with the same 1-mm resolution but different penetration, cost and sensitivity as shown in Table 5.7. To more accurately evaluate the sensitivity and resolution performance of the proposed designs, a Monte Carlo simulation was developed that is introduced in next section.

Analytical Design					**Monte Carlo Simulation**	
Bore length (µm)	Bore diameter (µm)	Septal thickness (µm)	No. layers	Penetration (%)	Resolution (mm)	Sensitivity ($\times 10^{-5}$)
4.4	150	100	44	2.31	1.17	1.8
5.15	180	125	42	1.06	1.17	1.8
6.9	225	150	46	0.28	1.15	1.4

Table 5.7: Different analytical designs with Monte Carlo evaluations of the LEUHR parallel-hole collimator based on manufacturing requirements.

5.3.2 Monte Carlo Simulation

The Monte Carlo simulation takes the collimator geometry parameters as input, creates a 3D profile and traces many gamma-rays emitted by a point source until they are absorbed by the collimator or penetrate through the collimator. Because Compton scattering is a minor effect for low-energy gamma-rays (such as 140keV photons), Compton-scattered photons are not traced. There are only two possible outcomes after the interaction between gamma-rays and the collimator materials, i.e. either absorption or penetration. For penetrated gamma-ray photons, a pixelated detector with the effective pixel size of the LA-iQID was used for photon collection. Figure 5.13 shows a simulated PSF and its corresponding cross-cut profile. The Monte Carlo simulation has been applied to the proposed design solutions to evaluate the resolution and sensitivity performance. The results are shown in Table 5.7.

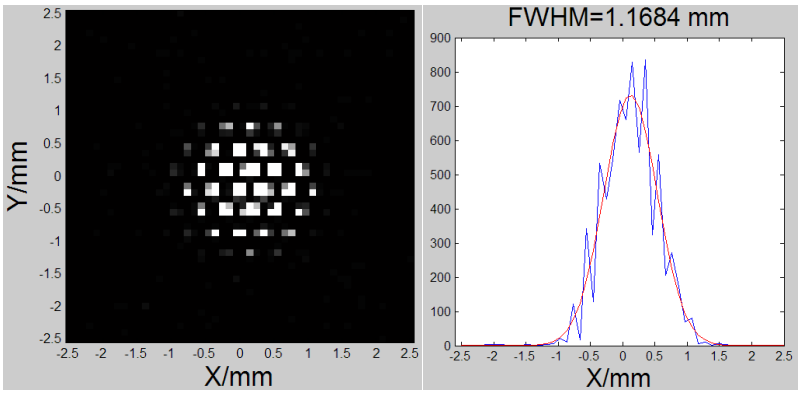

Figure 5.13: Left: Monte Carlo simulated PSF of a point source 2cm away from an analytically designed parallel-hole collimator (L=5.15mm, d=180μm, t=125μm). Right: Cross profile of the simulated PSF demonstrating 1.17mm FWHM resolution.

5.3.3 Optimized Solution

From Table 5.7 we can see that the second solution provides the same resolution and sensitivity performance as the first solution, but with lower cost and penetration. The third solution can provide better penetration and resolution performance than the second solution, but the price is higher and the sensitivity is compromised. Therefore, the second solution with 5.15 mm bore length, 180 μm bore diameter and 125 μm septal distance was chosen as the final design of the LEUHR parallel-hole collimator, and it was manufactured by Tecomet using their photo-chemical etching and lamination technique as shown in Figure

5.14. The collimator has an effective area of 19 cm × 19 cm with a total dimension of 20 cm × 20 cm.

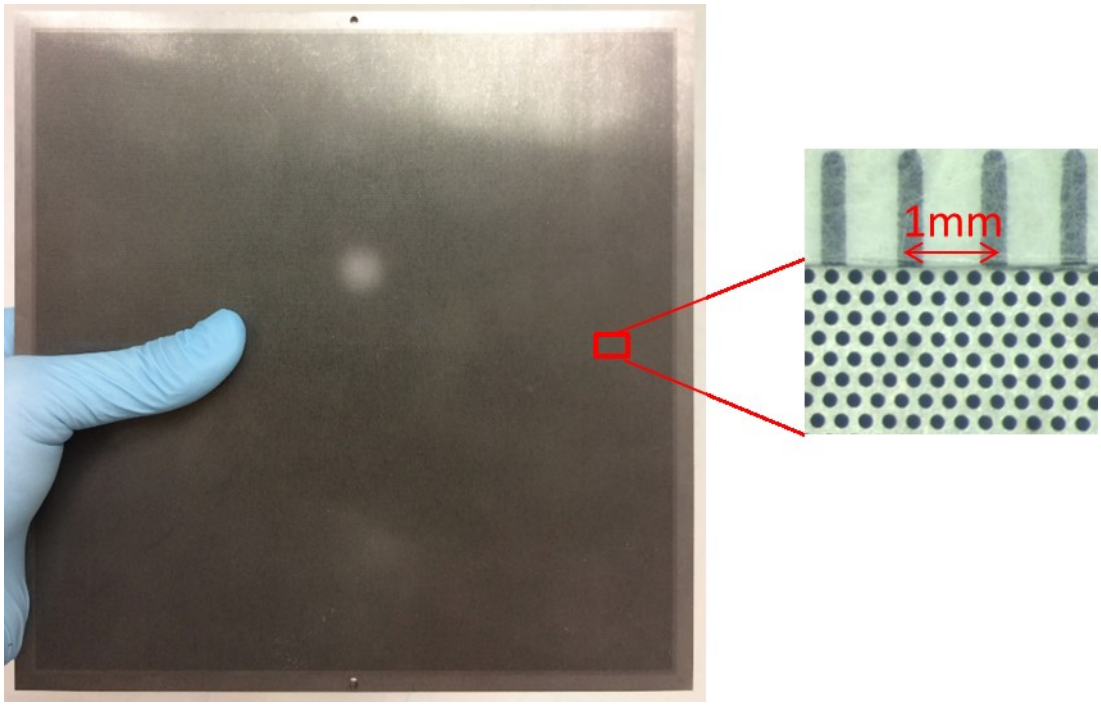

Figure 5.14: The manufactured LEUHR parallel-hole collimator with 5.15 mm bore length, 180 µm bore diameter, and 125 µm septal distance from the optimized design solution.

5.4 Camera Integration

The camera integration started with the four square FO tapers, which were already affixed to aluminum blocks with strong epoxy. To integrate the round FO taper and image intensifier for each iQID, a light-sealed housing was required because the high-gain image intensifier will see any weak-intensity light leaking through the housing and amplify it to a very strong signal, causing damage to the photocathode or phosphor screen. Therefore, a thick customized housing with a built-in baffle was designed and 3D printed on CGRI's Stratasys Connex 350 printer using VeroBlack material for both the round FO-taper and the image intensifier as shown in Figure 5.15. [Stratasys] Silicone optical grease was used between the tapers and entrance faces of the image intensifiers during integration. Since both the FO entrance face of the image intensifier and the round FO-taper are fragile, strong pressure could damage either of them. Therefore, three spring-loaded screws were used for holding the image intensifier to the round FO-taper so that precisely adjustable pressure can be

applied. This also makes the image intensifier tolerant to any small accidental slide of the square FO taper due to epoxy failure. A test piece was subjected to a load test and no expoxy failure has been observed.

After the round FO taper and the image intensifier were integrated, two small rectangular aluminum plates with 8 screws were used to fasten while aligning each square FO taper with 6-degrees of freedom to a bigger aluminum frame as an external protection for the four iQID cameras as shown in Figure 5.16. An extra aluminum cylinder was also applied surrounding the round taper and image intensifier assembly. The four CCD sensors with relay lenses attached were then attached to 3D-printed holders with screws, which were further aligned with the image intensifiers and fastened to the external aluminum frame.

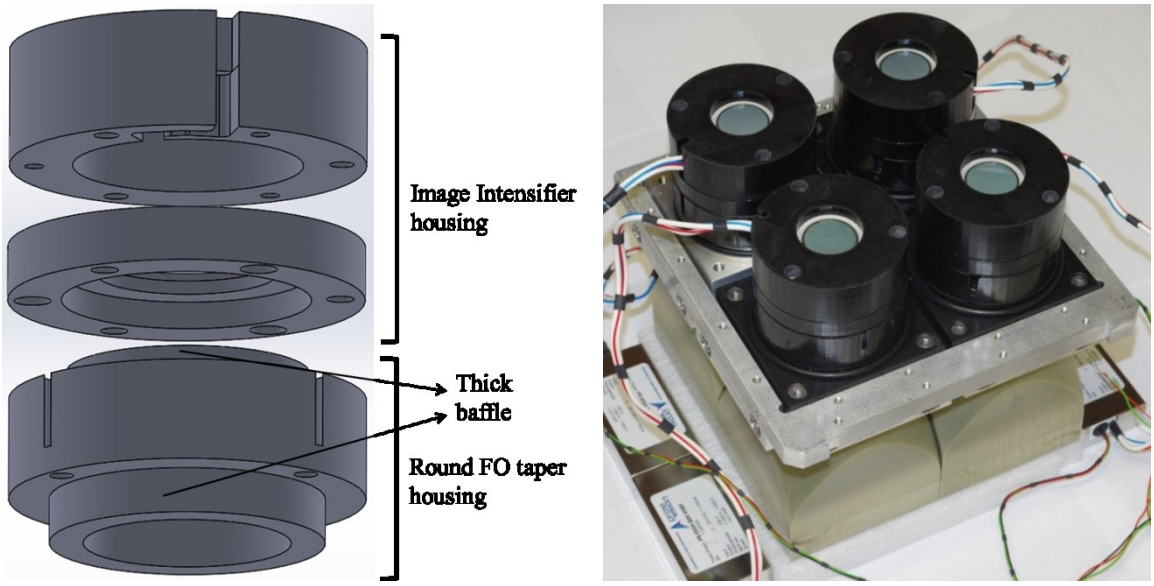

Figure 5.15: Left: SOLIDWORKS rendering of the designed baffle-embedded housing for the round FO taper and image intensifier assembly. Right: 3D-printed housing installed on the round FO tapers and image intensifiers and integrated on the square FO tapers.

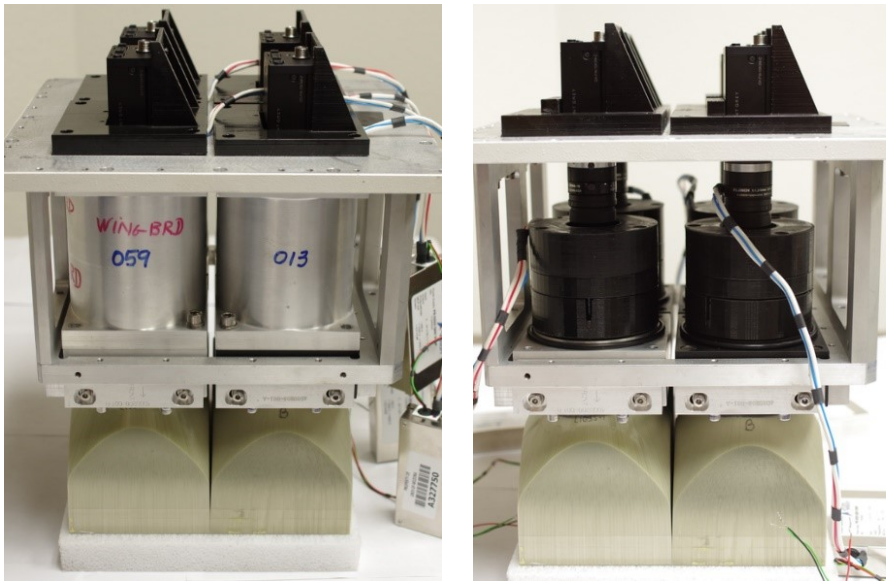

Figure 5.16: Inner view of the LA-iQID camera with all components fixed onto an aluminum frame with (Left) and without (Right) protective aluminum cylinders sealing the round FO tapers and image intensifiers.

The whole assembly as shown in the left figure of Figure 5.16 was rotated with square FO tapers facing horizontally and a thick aluminum box was carefully and gently placed around the aluminum frame. Steel shims are used to fill the gaps between square FO tapers and the aluminum box and screws are used to fasten the box and the frame together, thus finishing the whole assembly of LA-iQID as shown in Figure 5.17.

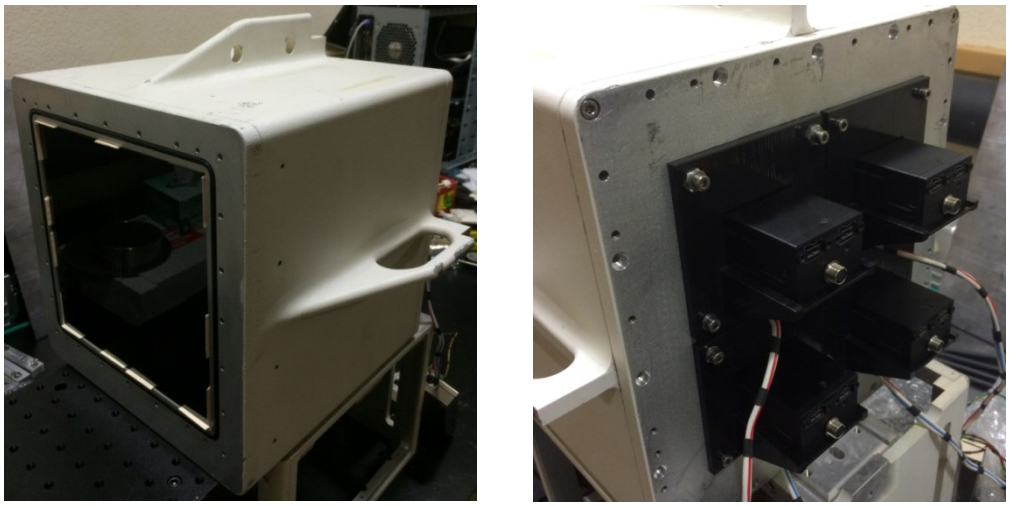

Figure 5.17: Front view (Left) and rear view (Right) of the fully integrated LA-iQID camera (except scintillator and collimator) with external thick-aluminum housing.

Finally, the customized large-area flat-panel columnar CsI(Tl) scintillator was aligned and adhered onto the square tapers with artist tape, which leaves no residual after removal. The custom LEUHR square parallel-hole collimator was secured with corner aluminum plates (no direct contact but close enough to protect the collimator from falling) as shown in Figure 5.18. Spring-loaded screws then provide adjustable pressure to make sure the collimator is held against the scintillator with gentle force so as not to damage the scintillator. There are a total of 8 spring-loaded screws designed to fully balance the weight of the collimator (~8 pounds) when the LA-iQID is facing downward, although only four of them are shown in Figure 5.18. At this point, the LA-iQID with gamma-ray detector and imaging collimator is fully integrated and ready for data acquisition, camera calibration and imaging tasks.

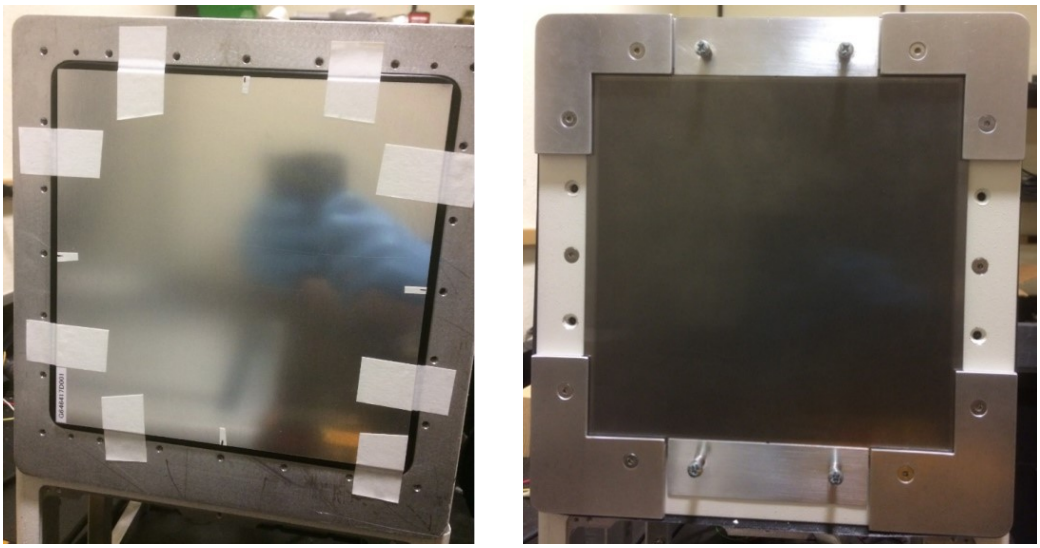

Figure 5.18: Integration of the flat-panel columnar CsI(Tl) scintillator (Left) and the custom LEUHR parallel-hole collimator (Right) with spring-loaded screws and corner plates.

5.5 Data Acquisition and Graphic User Interface

Two frame grabber cards with PCIe Express 2.0×1 bus, each with 2 FireWire 1394b ports, were used to synchronize the four CCD sensors and simultaneously acquire image data. Although up to 70 fps frame rates are supported, with current 10-meter FireWire cables, missing images in data transmission have been observed at maximum frame rates. A frame rate of 40 or below is thus recommended for collecting all image data in real-time. However, this limitation can be resolved with shorter FireWire cables. Multi-core parallel-processing of the images from the four iQID cameras are then applied in real time with the new frame-parsing algorithm, which is able to acquire list-mode data and does not require GPU processing as introduced in Chapter 4. However, the PC is equipped with an i7-3770 CPU @ 3.40GHz and 8.00 GB of RAM.

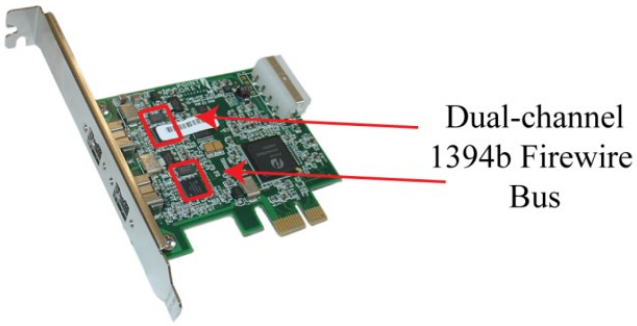

Figure 5.19: The dual-channel frame-grabber card with IEEE 1394b FireWire bus for simultaneous image acquisition from two iQID cameras. Two identical cards are used in LA-iQID.

A user-friendly graphical interface (GUI) was designed and developed to facilitate easy data acquisition by any potential user. Acquisition parameters can be preset for noise discrimination. Three acquisition modes, i.e. live object positioning, static image acquisition and dynamic image acquisition, are available for different imaging tasks. The acquired raw images from four iQIDs can be viewed in real time, and distortion-free images can be viewed as soon as the acquisition is finished. Figure 5.20 shows the developed GUI with image acquisition panel and viewing panel.

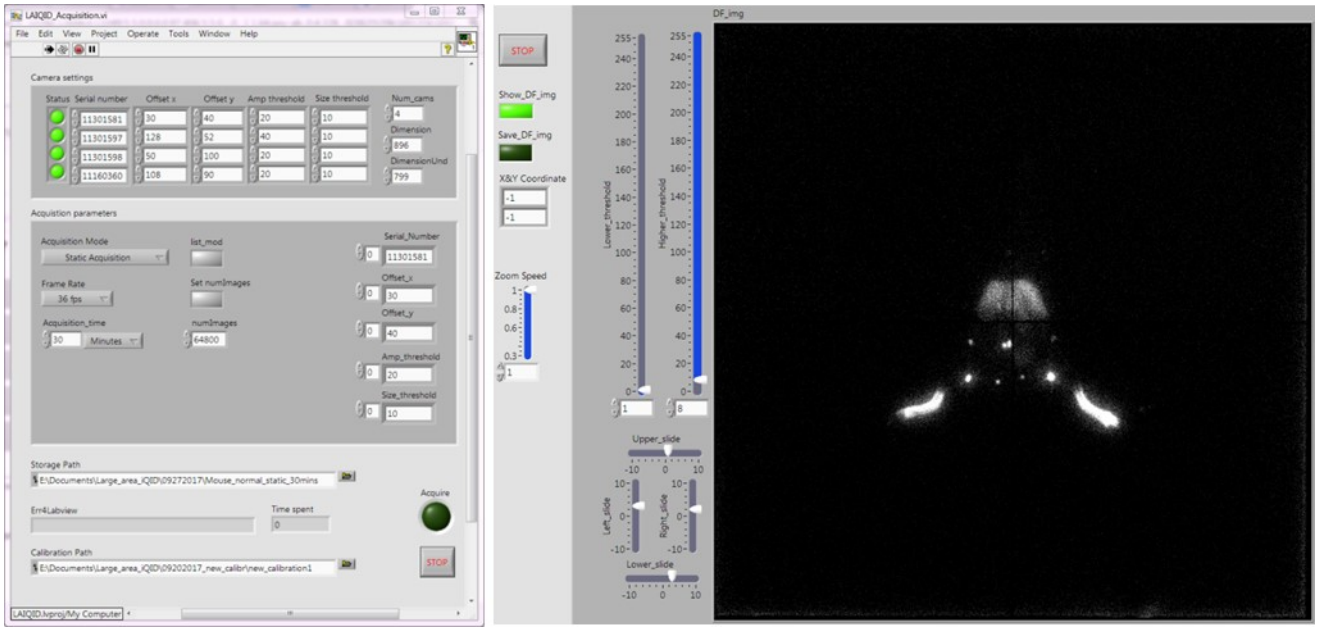

Figure 5.20: The GUI of the LA-iQID camera for image acquisition and viewing. Multiple data acquisition modes are built in including live object positioning, static image acquisition and dynamic image acquisition.

5.6 Camera Calibration

Due to the use of an optical lens and FO tapers, optical distortion is introduced in the projection images, which needs to be corrected before an accurate representation of the object position and dimensions can be made. Also, due to manufacturing limitations, a narrow insensitive edge along the perimeter of the square FO tapers is inevitable, causing a 400-600 μm gap between adjacent tapers. This results in a discontinuous projection image with a black cross in the middle. To recover a continuous and smooth image across the whole FOV of LA-iQID, an image-stitching algorithm is needed and image uniformity needs to be corrected.

5.6.1 Distortion Correction

In the LA-iQID camera, optical distortion is caused by the optical lens and FO tapers, with the lens being the dominating factor. If the distortion is solely caused by the lens and demonstrates rotational symmetry, an analytical distortion model can be characterized by minimizing RMS distance between predicted and a priori known lines. [Alvarez et al. 2010] The characterized model can then be used for distortion correction. However, because the

FO tapers introduce extra distortion, an alternative distortion correction method based on bilinear interpolation was used in this work. A similar method has also been applied by Zhao et al. [2009].

First, a 5-mm-thick calibration pattern consisting of a grid of 74×74 1-mm-diameter holes with a pitch of 2.54 mm (0.1 inch) was designed and 3D printed with VeroBlack material, as shown in Figure 5.21. The total area of the calibration pattern is 188 mm × 188 mm, which matches perfectly the total FOV of LA-iQID. The calibration pattern was backed with a Lanex phosphor screen with the same area, and then set against the square FO tapers of the LA-iQID (the scintillator and collimator were temporarily removed). Alignment between the calibration pattern and the square tapers was also performed to make sure no holes fell into any gap. After sealing with the camera cover, a ^{57}Co source was placed at five different positions (center of FOV, upper-left, upper-right, lower left and lower-right corners), 5 cm over the phosphor screen for uniform image acquisition of the calibration pattern. In this work, the ^{57}Co had an activity of ~65 μCi and the total acquisition time used was ~1 hour with 10-12 minutes at each source position. Figure 5.22 shows the acquired centroid image of the calibration pattern from one iQID camera, which demonstrates apparent barrel distortion. Based on the distorted image, distortion correction was implemented with the following steps:

(1) Identification of the holes from the background and estimation of the center-of-gravity centroid location of each hole in the distorted image. Record the x and y coordinates of each centroid location based on local coordinate system.

(2) Establish another distortion-free image with a grid of 74×74 points (multiple pixels between neighboring two points, for example, 20 pixels as used in this work), representing the true locations of the centroids of all holes. Record the x and y coordinates of all points based on local coordinate system.

(3) Calculate matrices of the x and y translations from true centroid locations to distorted centroid locations.

(4) Use bilinear interpolation to calculate the corresponding x and y translations for any pixel in between the 74 × 74 points based on the distances from the pixel to its neighboring four corner points, the translation matrix of which is already calculated in step (3).

(5) Similarly, use linear interpolation to calculate the corresponding x and y translations for pixels within one pitch (20 pixels in this work) beyond the 74×74 grid.
(6) Save the fully-calculated mapping matrices into files for future distortion correction.

After step (1)-(6), two matrices containing x and y translations of any pixel from the distorted image to a distortion-free image are generated, yielding a complete mapping. Correct coordinates for each pixel in a distorted image can then be calculated by applying the coordinate mapping matrices. Based on the mapping, each pixel (x, y) in the distortion-free image can be mapped to a corresponding location (x', y') in the distorted image. Four neighboring pixels can then be found in the distorted image surrounding the location (x', y'). The amplitude of pixel (x, y) is then bilinear-interpolated based on the neighboring four corner pixels in the distorted image. A distortion-free image is thus created as shown in Figure 5.22. As distortion-free images for the four iQID cameras are generated, they can be easily registered based on their relative locations defined by the calibration pattern. The registered image is now ready for image stitching.

Figure 5.21: The 3D-printed calibration pattern with 74 × 74 holes, 2.54-mm pitch and 5-mm thickness, each hole with 1-mm diameter.

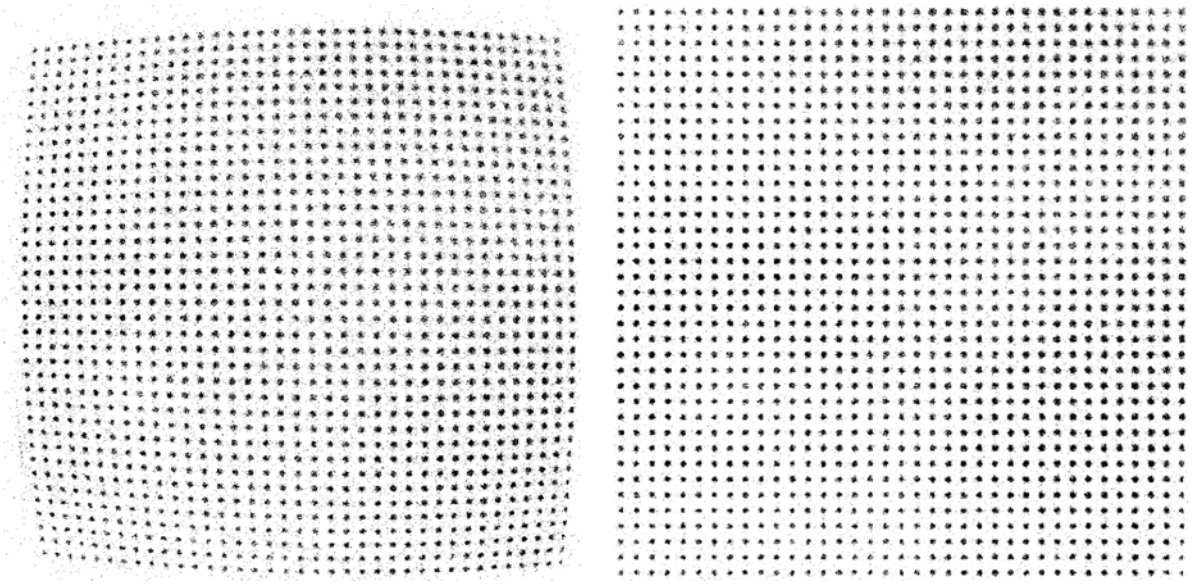

Figure 5.22: Left: Raw distorted projection image of the calibration pattern illuminated by a phosphor screen and acquired from one iQID camera. Right: Distortion-free version of the same projection image using the proposed algorithm.

In this distortion correction method, the design and manufacture of the calibration pattern plays a crucial role. The large number of small diameter holes guarantees a high-accuracy calibration. The VeroBlack material with 5 mm thickness improves the image contrast for easy and accurate identification of holes. Because the image intensifier is so sensitive to light, a typical light source cannot be used for illuminating the calibration pattern, which could easily damage the photocathode or the whole image intensifier. As a result, the idea of backing the calibration pattern with a Lanex screen as illumination-light source and forming an image with long-time illumination guarantees the safety of the image intensifiers. Finally, compared with an alternative exhaustive-measurements method with a scanning pencil beam, this method does not require any motorized stages and can finish calibration in a relative short time.

5.6.2 Image Stitching and Uniformity Correction

Because of the presence of insensitive gaps between adjacent square tapers, the registered distortion-free image shows a dark cross in the middle, which separates the image into four disconnected square sub-images as shown in Figure 5.23. To stitch the four square sub-images and fill the gaps in between, interpolation is needed. There are many well-

established image processing filters or methods that can be applied to fill a gap in a general image, including average filter, median filter, mid-point filter etc. [Ali and Mohammed 2013] Almost all of the methods, however, require the image to have significant amplitude, or enough counts, which cannot always be satisfied for high-resolution gamma-ray centroid images (where pixel values represent the number of gamma-ray photons detected at that pixel location). Due to very small number of detected photons per pixel and the resulting sparse nature, the image content can potentially be erased if one of above mentioned filters is applied. Therefore, a new interpolation method that works with few counts and sparse gamma-ray images is required. In this work, a photon-based interpolation method was proposed that works by adding individual photons one by one to the gap pixels until the average amplitudes of gap pixels matches with the average amplitude of pixels on both sides of the gap. The whole image stitching procedures can be described as follows:

(1) 2D flood illumination images from four iQIDs are acquired using a ^{57}Co point source at a relatively far distance (33 inches as used in this work) for a long time (6 hours was used in this work). (The collimator is removed beforehand)

(2) The distortion in the images is corrected and the distortion-free images are registered as shown in (a) of Figure 5.23.

(3) A square mathematical model is used to define the effective region/FOV of the LA-iQID.

(4) An amplitude threshold is applied to identify all pixels in the effective region that need to be interpolated, which include gap pixels, center-of-cross pixels, and dark pixels resulting from image intensifier or fiber-optic taper defects as shown in (b) of Figure 5.23.

(5) A classification algorithm is applied to separate identified pixels from step (3) into three categories represented by different colors, i.e. horizontal gap (yellow), vertical gap (red), and defects (white), as shown in (c) of Figure 5.23. All identified and classified pixels will be recorded in a look-up table.

(6) All pixels in the look-up table are interpolated with the photon-based interpolation method based on their locations in the image.

(7) The interpolated distortion-free flood image is further normalized as shown in (d) of Figure 5.23 and saved to a file for future uniformity correction.

The steps (1)-(7) are performed only once during camera calibration. After the look-up table and result (d) of Figure 5.23 have been acquired, for each set of newly acquired projection images only step (2) and (6) are performed, as shown in (a) and (b) of Figure 5.24. However, as shown in (b) of Figure 5.24, the stitched image can still demonstrate nonuniform amplitude especially at the gap pixels. To correct the nonuniformity, the image (d) of Figure 5.23 is used as a normalization, resulting in a seamless and uniform image with an example shown in (c) of Figure 5.24.

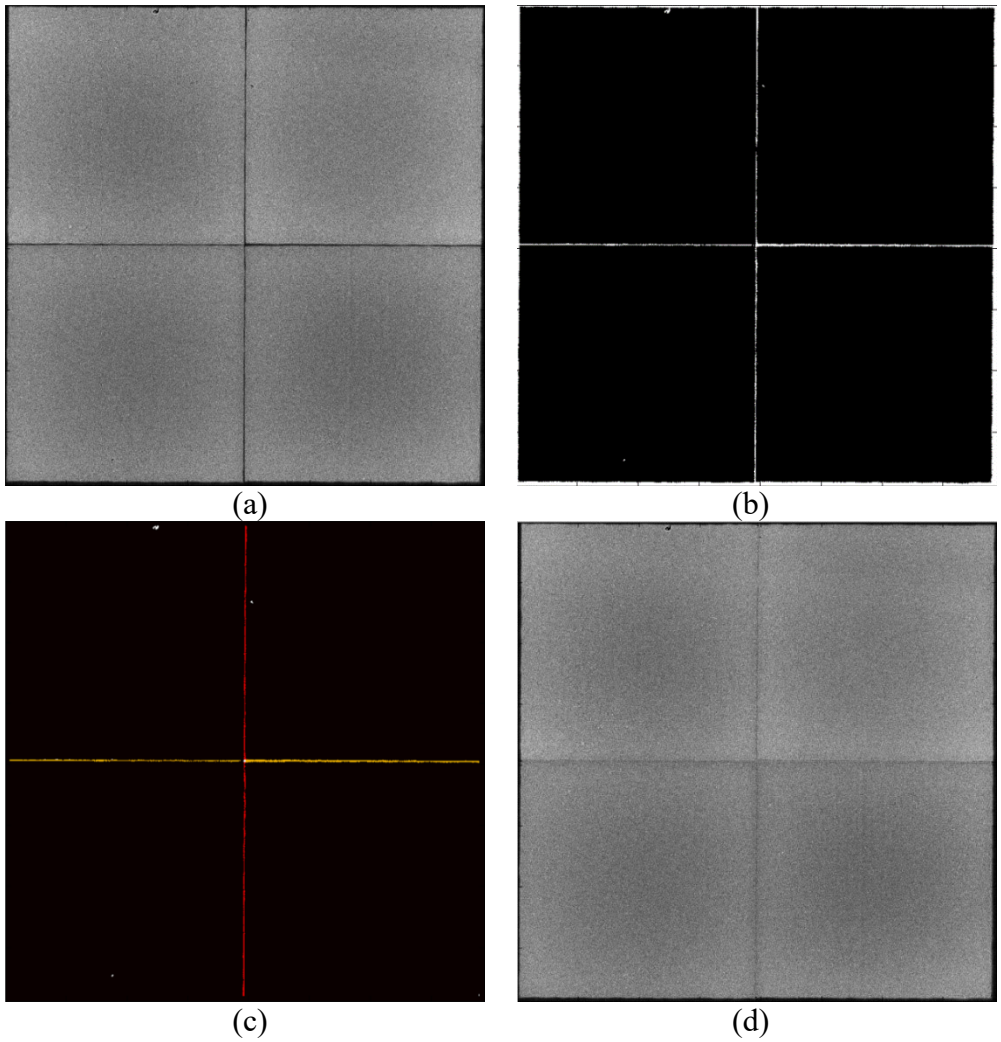

Figure 5.23: (a) 6-hour flood illumination image acquired with the LA-iQID camera (without collimator) and a ^{57}Co source placed 33 inches away. (b) Resulting image of (a) by applying an amplitude threshold to identify gap pixels and defect pixels. (c) Classification image with horizontal gap, vertical gap and the remaining pixels to be interpolated shown in yellow, red and white colors. (d) Stitched flood illumination image after interpolation.

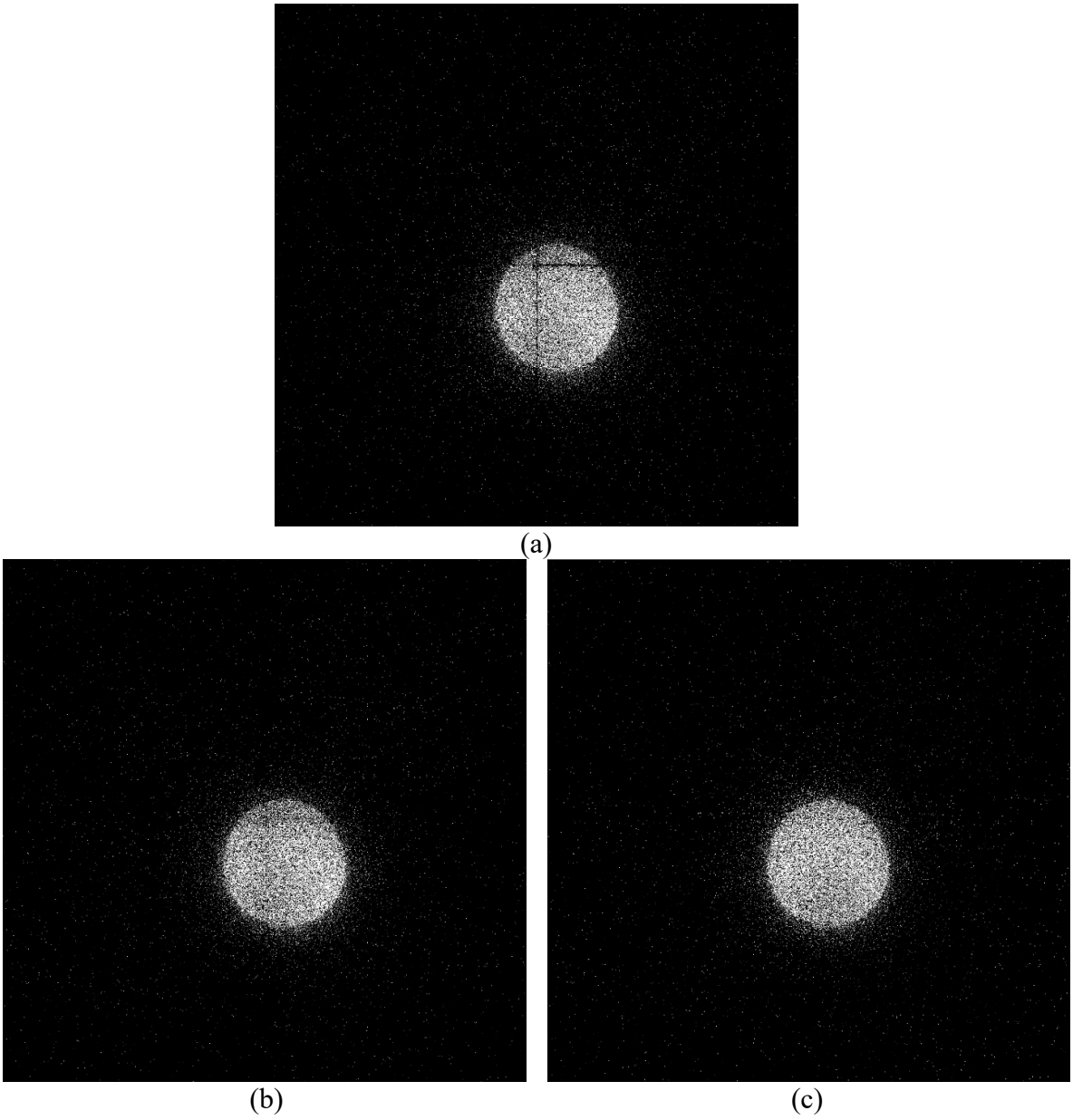

(a)

(b) (c)

Figure 5.24: (a) A distortion-free circular projection image of a ^{57}Co source through a circular aperture. (b) Interpolated version of (a) with nonuniform intensity around the gap region. (c) Smoothed version of (b) after divided by the stitched and normalized flood illumination image, demonstrating smooth and uniform intensity distribution.

With distortion-correction mapping, interpolation look-up table, and interpolated flood image acquired, the LA-iQID is fully characterized. Any images acquired in future imaging tasks can have distortion corrected, gaps interpolated, and uniformity corrected. The LA-iQID camera is now ready for performance evaluation.

5.7 Performance Evaluation

In this section, the intrinsic resolution and system resolution, as well as the lymphatic imaging capability of the LA-iQID are evaluated. The results demonstrate subjectively excellent resolution performance and image quality.

5.7.1 Intrinsic Resolution

To evaluate the intrinsic resolution of the LA-iQID camera, a 75 μm-wide tungsten-slit aperture was placed in front of each iQID as shown in Figure 5.25 (the collimator was removed). A ^{57}Co source was then placed in front of the slit aperture to acquire a projection image for each iQID. An example slit image is shown in Figure 5.25 as well. Because the effective pixel size of LA-iQID is ~120 μm, an ideal detector will yield a slit image of 1-pixel width. By fitting a Gaussian line-spread-function (LSF) for each projected line image, the FWHM can be calculated as shown in Figure 5.26, and used as a measure of intrinsic spatial resolution. Results show that the intrinsic resolution of the LA-iQID vary between 445-541 μm, which is 6-7 times better than the system resolutions of most dedicated clinical gamma cameras (3-4 mm). The origin of resolution variation among the iQID cameras is mainly the variation of effective pixel size due to different magnifications incurred by slightly different phosphor-to-lens distances.

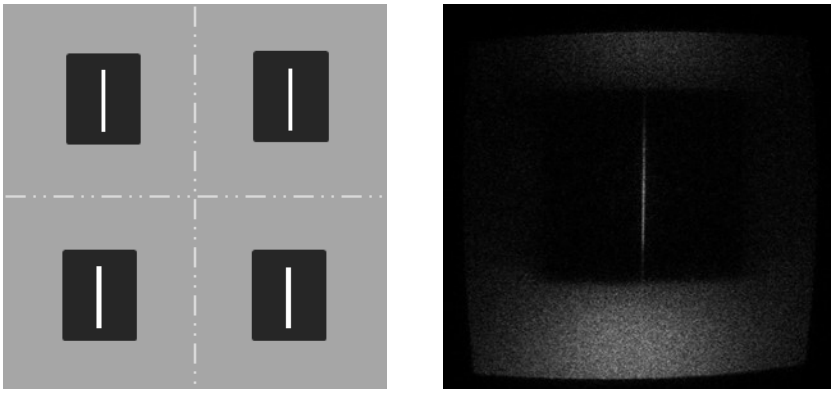

Figure 5.25: Left: experimental setup for intrinsic resolution evaluation with a 75 μm slit aperture placed in front of each iQID. Right: The line projection image of the slit aperture illuminated with a ^{57}Co source acquired from one iQID.

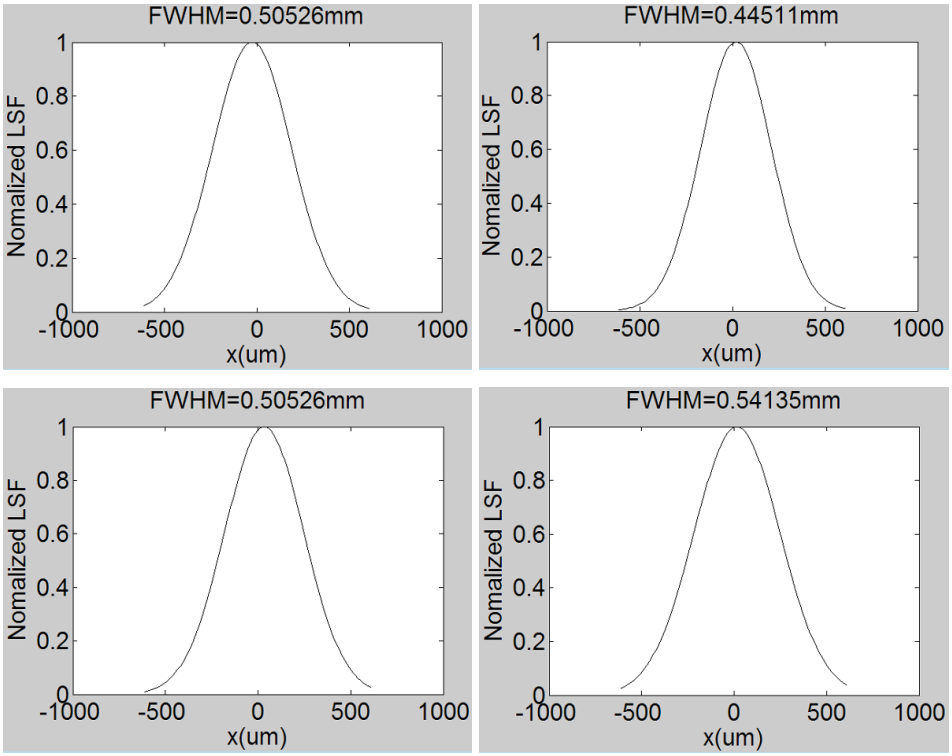

Figure 5.26: Generated LSFs for the four iQIDs based on acquired line projection images, which demonstrate 445-541μm intrinsic spatial resolution across the whole FOV.

5.7.2 Phantom Imaging

With the collimator installed, the system resolution is dominated by the resolution performance of the collimator, although detector intrinsic resolution also contributes. To evaluate the system performance of LA-iQID, a phantom with five 1-mm bores was 3D printed with FullCure720 material (transparent). The edge-to-edge distance between two adjacent bores varies from 1.2 mm to 0.6 mm as shown in Figure 5.27. Approximately 1mCi of liquid ^{99m}Tc-pertechnetate was injected into all five bores and the phantom was placed at 5 mm and 2 cm away from the collimator entrance face at the center of one iQID camera. 10-minute projection images were then acquired for both locations as shown in Figure 5.28. From the acquired projection images, we can see that at the 2-cm distance, the second and third bores can be separated, which demonstrates ~1mm resolution performance with 18.5% contrast. For 5mm distance, all bores can be separated, demonstrating 0.6 mm resolution performance with 20% contrast. The contrast is defined based on Michelson formula [Peli 1990] as

$$Contrast = \frac{(Peak-Valley)}{(Peak+Valley)} \times 100\% \,, \tag{5.6}$$

and is applied to the cross-cut profiles of the projection images of the phantom as shown in Figure 5.27: The designed phantom with five 1mm-diameter bores and varying pitch in between for system resolution evaluation.

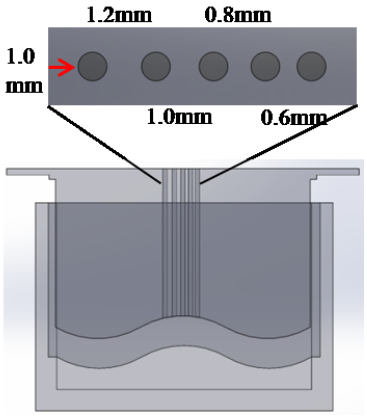

Figure 5.27: The designed phantom with five 1mm-diameter bores and varying pitch in between for system resolution evaluation.

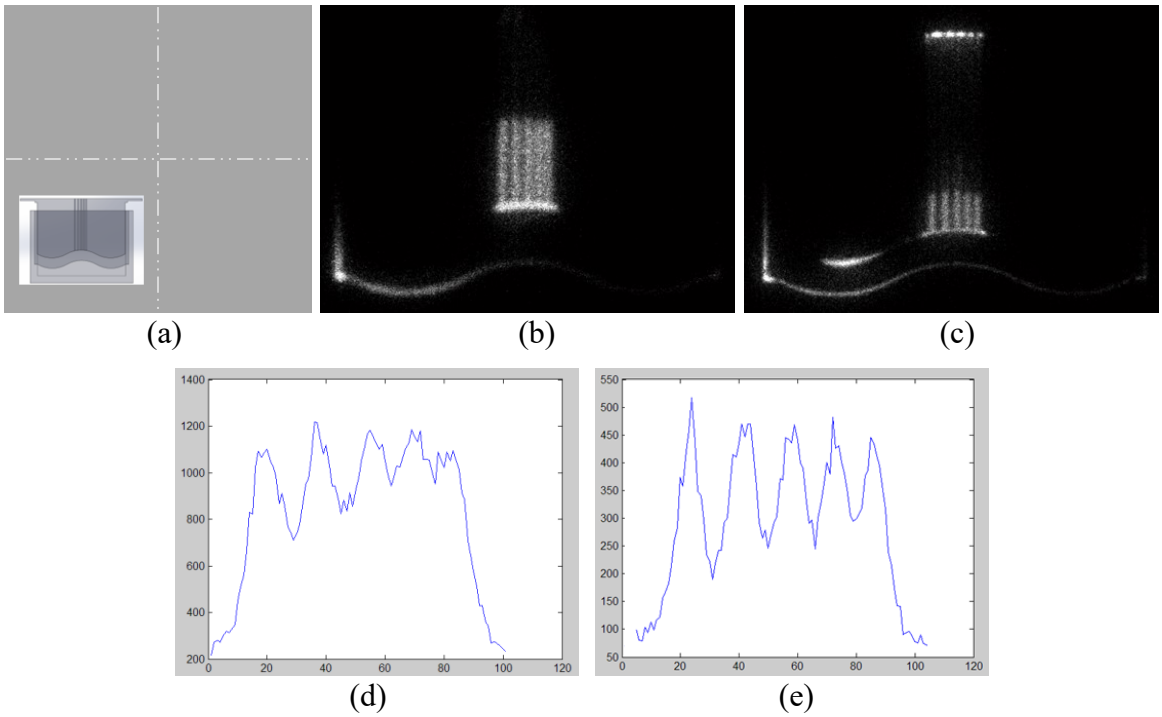

Figure 5.28: (a) Experimental setup with the phantom placed in the middle of one iQID. 10-minute projection images were acquired with the phantom placed 2 cm (b) and 5 mm (c) away from the collimator. Cross-cut profiles of (b) and (c) are shown in (d) and (e) respectively and are used to calculate the Michelson contrast of both phantom images.

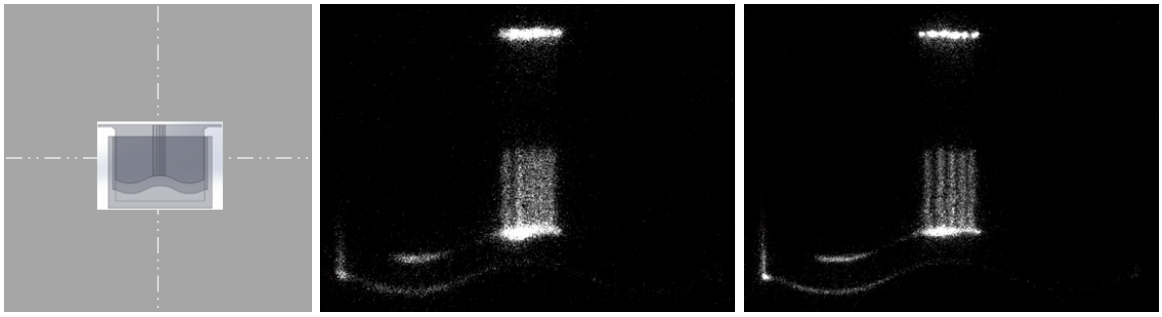

Figure 5.29: Left: Experimental setup with the phantom placed in the center of the LA-iQID FOV. 10-minute projection images were acquired with the phantom placed 2 cm (Middle) and 5 mm (Right) away from the collimator. Results demonstrate distortion free, seamless and uniform images.

To evaluate the performance of the distortion-correction and image-stitching algorithms, an extra 0.25 μCi liquid ^{99m}Tc-pertechnetate was added to the phantom since the initially injected liquid was diminished due to evaporation and leakage from the bores. The phantom was then placed in the center of the FOV of the LA-iQID. Projection images were again acquired within 10 minutes for both the 2-cm and 5-mm distances as shown in Figure 5.29. We find that the distortion has been corrected and the images are registered and stitched so that no gaps are visible. The uniformity is also corrected for both images such that the interpolation is invisible. The resolution can be preserved after the interpolation unless the features are very small and exactly falls into the gap between tapers. As shown in the middle image of Figure 5.29, the gap between the 2nd and 3rd bores exactly fall into the gap between the square tapers and cannot be recovered during interpolation. The distortion correction is very accurate except for the few edge pixels outside of the calibration pattern, where ~200-300 μm error can be visible when the system resolution is comparably high. For example, the bores in the right image of Figure 5.29 demonstrated slight bending.

5.7.3 Mouse Lymphoscintigraphy

Finally, to demonstrate the lymphatic imaging capability of the LA-iQID camera, lymphoscintigraphy was performed on two mice. One mouse was normal and served as a control mouse. The other was genetically modified and might express an abnormal lymphatic system. For the normal mouse, a total of 360 μCi of Tc-99m Sulfur Colloid was injected through both feet and a 30-minute image was acquired ~300 minutes after the injection. For the genetically-altered mouse, a total of 411 μCi of Tc-99m Sulfur Colloid was injected through both feet and a 30-minute image was acquired ~360 minutes after the injection. Both images are registered with the optical images of the mice and are shown in Figure 5.30. We observed that the lymph nodes of both mice can be seen clearly with high resolution and contrast. Both livers are also visible in the images with clear shapes and outlines. Both livers were located in the center of the FOV but the images show no effects of the gap after stitching.

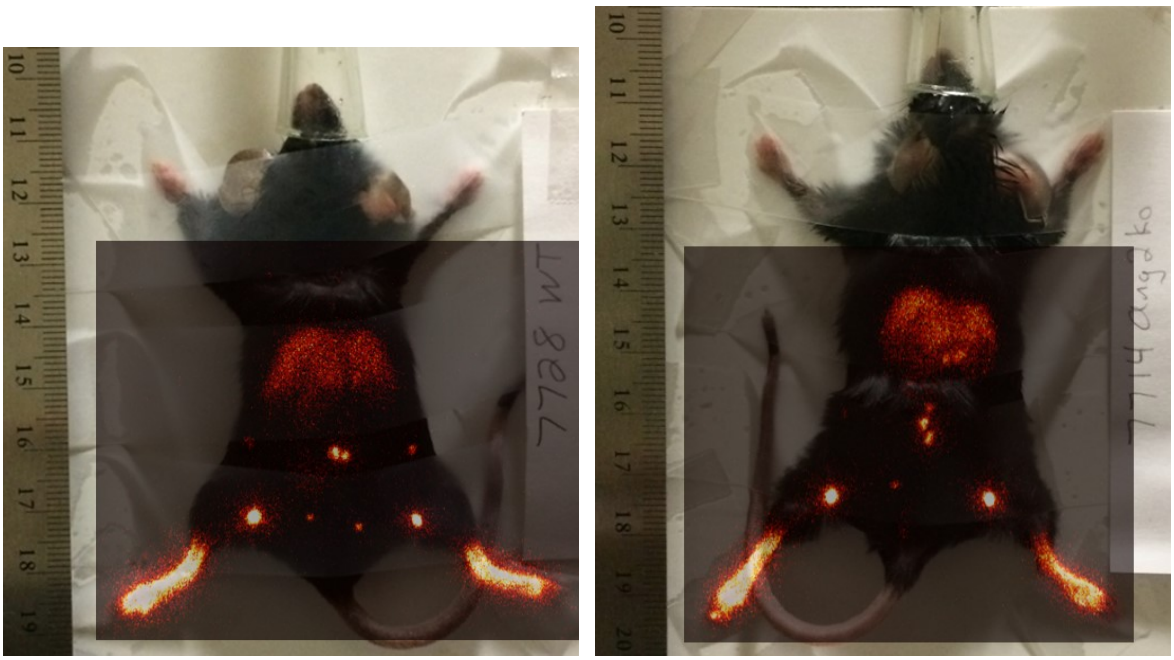

Figure 5.30: 30-minute lymphoscintigraphy images fused with optical images of a normal mouse (Left) and a genetically-altered mouse (Right), demonstrating high-resolution and seamless visualization of the lymph nodes and livers.

5.8 Mobility and Portability

A mobile and portable gamma camera can be very convenient for clinical imaging applications. However, the use of large-area FO tapers and thick aluminum housing greatly increase the weight of the LA-iQID. To add mobility and portability features to the LA-iQID, a steel holder has been custom manufactured that is able to connect the LA-iQID to the steel arm of a clinical cart. With a cylindrical pin inserted into the arm, the holder and the camera can be rotated together in one plane. Constructed with multiple sections connected by joints, the steel arm can be easily folded or stretched to position the camera at different locations. Also, because the arm is set in a vertical track and is counter-weighted by steel bricks, it can be lifted or lowered readily by hand. Finally, the cart has space for setting up a workstation and a monitor for data acquisition and image viewing. Equipped with four casters, the cart with complete LA-iQID system can be easily moved around as needed. Figure 5.31 shows the custom holder, the LA-iQID camera housing held by the holder, and the cart with camera housing and holder in place.

Figure 5.31: Top left: The customized steel holder with cylindrical pin for the LA-iQID camera. Top right: The external housing of LA-iQID held by the holder and attached to the arm of a clinical cart. Bottom: A photography of the counter-weighted clinical cart with LA-iQID external housing attached through the custom holder.

5.9 Conclusions

In this chapter, we have presented the development of a high-resolution large-area dedicated clinical gamma camera, called LA-iQID, from concept to prototype for lymphoscintigraphy. This is also the first attempt to advance iQID technology towards clinical imaging applications. The novel architecture of tiling of multiple FO-taper-coupled iQID cameras to increase the effective FOV while maintaining high-resolution performance has been introduced. High-performance components are used in the LA-iQID and described in detail. A LEUHR parallel-hole collimator was designed and manufactured with photochemical etching and lamination technique, which is able to provide ~1 mm system resolution and ~1.8×10^{-5} sensitivity for 140keV photons at a 2-cm distance and sub-mm system resolution at closer distances. The whole camera was fully integrated with a custom light-sealing housing to ensure operation in a normal room environment. Synchronized and simultaneous image acquisition from multiple cameras with a real-time list-mode processing and viewing GUI was developed. New gamma camera-calibration methods including distortion correction and image stitching have been demonstrated that are able to provide distortion-free, seamless, and uniform images across whole FOV. The performance of the LA-iQID camera and calibration methods were evaluated with slit aperture, resolution phantom and mice imaging, demonstrating ~1 mm resolution with 18% contrast at a 2-cm distance and ~0.6-mm resolution with 20% contrast at a 5-mm distance. Finally, a counter-weighted clinical cart with a flexible arm and a custom holder were presented, which provides mobility and smooth handling of the LA-iQID camera for convenient clinical imaging.

CHAPTER 6

CONCLUSIONS AND FUTURE WORK

6.1 Conclusions

This work started shortly after the novel high-resolution CCD/CMOS-based gamma camera, BazookaSPECT, and the first BazookSPECT-based preclinical SPECT system, FastSPECT III, were developed by Miller et al. in the Center for Gamma-Ray Imaging. Because of later-developed charged-particle imaging capability, as well as the need for a more serious name, BazookaSPECT was renamed iQID (intensified Quantum-Imaging Detector). Demonstrating superior spatial resolution performance and many other advantages over traditional gamma cameras, iQID technology is very promising for both preclinical and clinical applications. However, several advances and innovations were required before the concept-proven technology could be routinely used in practice.

A general limitation of iQID cameras observed to date is the poor energy resolution suggested to be due to the use of the image intensifier as the key amplification device. Image intensifiers have high spatial resolution but also large gain variations due to its continuous-dynode structure. The FastSPECT III system was designed for high-resolution rodent brain imaging. However, only a resolution phantom was successfully imaged at the time of its commissioning. Several factors limited its applications in mouse imaging, including the central-spot background noise generated by the XX1332 military-surplus image intensifier, low system sensitivity, and small common-FOV. To apply the iQID technology in clinical imaging applications, the primary challenge is to increase of FOV. The original iQID configuration only supports 1-2 inches (diameter) FOV limited by the effective area of image intensifiers. Although a fiber-optic taper can be coupled between the image intensifier and the scintillator to increase the FOV, only ~100-mm diameters can be achieved due to manufacturing limitations of large-area image intensifiers or light loss of large-magnification FO tapers.

This research successfully advanced the iQID technology by proposing and developing new hardware and software solutions so that the technology is ready for preclinical mouse

imaging and dedicated clinical evaluations. The significant contributions of this research on advancing iQID technology include:

- A Monte Carlo simulation package of the MCP physics, which analyzed the effects of gain variation on energy resolution and confirmed that it is the randomness in the number of wall interactions that is the largest variance contributor. We suggested possible solutions for improving energy resolution of iQID cameras.
- Development and implementation of a new frame-parsing algorithm, which has strong noise filtering capability with both amplitude and size thresholding for extracting gamma-ray events and is effective in removing the central-spot background events generated by XX1332 image intensifiers.
- Investigation and integration of a set of new thicker columnar CsI(Tl) scintillators, which greatly improved the system sensitivity of FastSPECT III while maintaining high spatial resolution.
- A new system calibration method for FastSPECT III that permitted full-body high-resolution mouse imaging when used with a multi-bed-position MLEM reconstruction algorithm, consisting of:
    - Hybrid multi-grid scan of a radioactive point source that is able to cover a large volume while maintaining high accuracy in the common-FOV.
    - System models including both geometry models and empirical models to interpolate the H matrix for any voxel in the FOV.
    - System characterization that estimated all parameters in system models based on constrained non-linear least-squares optimization algorithm.
- Development of a novel large-area iQID (LA-iQID) gamma camera based on tiling of multiple iQID cameras coupled with square fiber-optic tapers for dedicated clinical lymphoscintigraphy applications.
- A customized LEUHR parallel-hole collimator that is able to provide high-resolution (~1 mm at a 2 cm distance and ~0.6 mm at a 5 mm distance) imaging of commonly-used clinical radiotracers that emit 140 keV gamma-ray photons.
- System integration of the LA-iQID camera with 3D printed light-sealing housing and protective aluminum housing.

- Customized LabVIEW GUI for static and dynamic real-time image acquisition and viewing.
- Gamma camera calibration method including a novel distortion correction method based on a 3D-printed calibration pattern coupled with a phosphor screen, and a gap-filling interpolation method based on random event generation.
- A customized steel holder to connect the LA-iQID camera to a counter-weighted clinical cart with a multi-joint flexible arm for smooth operation and mobile capability around patients.

6.2 Future Work

Because the use of image intensifiers limits the energy resolution performance of iQID cameras, we suggest continued investigation of new image amplification devices that are able to preserve high spatial resolution while maintaining good energy resolution. The discovery of such a device in the future could yield next-generation iQID cameras with improved energy resolution and S/N ratios, suitable for more applications such as multi-isotope imaging.

To enhance the calibration accuracy of FastSPECT III system, a better sensitivity model is desired that is able to fit more accurately the dramatic sensitivity variations close to the pinhole apertures. Fully automated image acquisition along with helical scanning of the object is desired, which will be able to shorten acquisition times for each scanning position and increase the number of positions to reduce artifacts and improve reconstructed image quality. The current image-acquisition software also generates a set of projection images for each bed-position, yielding a large number of files when a large number of positions are scanned. So modification of the image acquisition code to generate one image file with data acquired at all bed positions is highly desired. Finally, the clearance in the current imaging aperture only allows up to 4 mm diameter helical scanning of the object, which provides an effective FOV of ~16 mm diameter and thus a tight tolerance for positioning the mouse in the center of the FOV. A young mouse with small size is also required to fit into the small effective FOV. To overcome this limitation, a new imaging aperture with ~2-cm-larger diameter is desired.

For long-term, routine and stable service, some hardware and software components of FastSPECT III system needs to be replaced. Some image intensifiers were observed to flash frequently, causing over-exposed image frames and reducing the sensitivity of corresponding iQID cameras. The data-acquisition computers have been running for almost 10 years, so that some components including hard drives, CPU fans and thermal paste are experiencing age-related problems. The shared-variable system used for communication between the control computer and the five slave computers is unstable and could corrupt system files over time, causing various system failures including frequent software crashes, blue screens, black screens, unable to boot, and so on. It's highly recommended to replace the shared-variable system with another more stable interprocess communication system.

The LA-iQID camera demonstrated excellent performance in phantom and mouse imaging, however, as a portable and mobile camera, the stability can be further improved. Although the designed orientation of the camera is facing downward, slow sagging was observed over time when the camera is facing horizontally, demonstrating a potential stability issue. Instead of filling the gaps between tapers and external housing with steel shims, steel plates supported with screws through the external housing could provide better mounting of the tapers, thus better stability performance. Because high-resolution performance requires rigidity for the camera calibration data to remain accurate, the current 3D-printed parts holding the CCD sensors may flex over time, causing image shifts, and are therefore recommended to be replaced with aluminum parts. The flat-panel columnar CsI(Tl) scintillator was manufactured to have an effective area of 193 mm × 193 mm, which is larger than the designed effective area of 189 mm × 189 mm. The inaccurate dimensioning by the manufacturer makes the scintillator float over the entrance face of the square FO tapers at a distance of ~0-1 mm, which could reduce the light collection efficiency and cause sensitivity reduction. Also because of the wrong dimension, the scintillator is supported only along the four edges, making it too fragile to support any extra weight, so extra protection is required when the camera is facing upward and the collimator needs to be placed on top of the scintillator. Returning the scintillator to the manufacturer for cutting and processing is recommended until the designed dimensions are achieved.

Finally, due to the excellent performance and the large FOV, the LA-iQID is a promising candidate gamma camera for dedicated clinical SPECT imaging applications. When set on two rotation stages, projection images from multiple directions can be acquired and 3D high-resolution image can be reconstructed. Potential applications include dedicated breast imaging and brain imaging.

REFERENCE

[Adams 1966] J. Adams and B. W. Manley, IEEE Trans. Nucl. Sci. NS-13, No. 3,88 (1966).

[Agarwal] Tarun Agarwal, https://www.elprocus.com/know-about-the-working-principle-of-charge-coupled-device/

[Alford 2009] R. Alford, M. Ogawa, P. L. Choyke, and H. Kobayashi, Molecular probes for the in vivo imaging of cancer, Molec. BioSyst., vol. 5, no. 11, pp. 1279-1291,2009.

[Ali 2013] S.M. Ali, M.J. Mohammed, Gap-Filling Restoration Methods for ETM+ Sensor Images, Iraqi Journal of Science,2013, Vol.54, No. .1, Pp.206-214.

[Alvarez 2010] Luis Alvarez, Luis Gomez, J. Rafael Sendra, Algebraic Lens Distortion Model Estimation, Journal Image Processing On Line, DOl http: dx.doi.org 10.5201 ipol.2010.ags-alde,2010.

[Anger 1952] H. Anger, Use of a gamma-ray pinhole camera for in vivo studies, Nature,1952.

[Anger 1958] H. O. Anger, Scintillation camera, Rev. Sci. Inst., vol. 29, no. 1, pp. 27_33,1958.

[Anger 1964] H. O. Anger, "Scintillation camera with multichannel collimators," J. Nucl. Med., vol. 5, pp. 515-531, 1964.

[Anger 1967] ANGER, H. O., Radioisotope cameras. In instrumentation in nuclear medicine, ed. G. J. Hine, Academic Press, Inc., New York, 1967,vol. 1, p. 485

[Auricchio 2003] Auricchio, A., P. D. Acton, M. Hildinger, J.-P. Louboutin, K. P, E. O'Connor, H. F. Kung, and J. M. Wilson (2003). In vivo quantitative noninvasive imaging of gene transfer by single-photon emission computerized tomography. Human gene therapy, 14(3), pp. 255-61. ISSN 1043-0342. doi: 10.1089/10430340360535805.

[Authinarayanan 1976] A. Authinarayanan and R. W. Dudding, Adv. Electron. Electron Phys. 40, 167 (1976).

[Barber 2013] H. B. Barber et al., "Imaging properties of pixellated scintillators with deep pixels," in Proc. SPIE Opt. Eng. Appl. Int. Soc. Opt. Photon., San Diego, CA, USA, Sep. 2013, Art. no. 92150F

[Barrett, 1981] H. H. Barrett, W. Swindell, Radiological Imaging: The Theory of Image Formation, Detection, and Processing Vol. 1 and 2, Academic Press, New York, 1981.

[Barrett, 2004] H. H. Barrett, K. J. Myers, Foundations of Image Science, New York, John Wiley and Sons, 2004.

[Barrett 2005] H. H. Barrett and W. C. J. Hunter, “Detectors for Small-Animal SPECT I”, ch.2 in “Small Animal SPECT Imaging”, M. A. Kupinski and H. H. Barrett, editors, Springer Science+ Business Media, 2005.

[Barrett 2009] Harrison H. Barrett, William C. J. Hunter, Brian Miller, Stephen K. Moore, Yichun Chen, and Lars R. Furenlid, Maximum-Likelihood Methods for Processing Signals From Gamma-Ray Detectors, IEEE transactions on nuclear science 56 (2009), no. 3, 725.

[Beekman 2004] F.J. Beekman and B.Vastenhouw, Design and simulation of a high-resolution stationary SPECT system for small animals, Physics in Medicine and Biology 49 (2004), no. 19, 4579-4592.

[Beekman 2005] F. J. Beekman, F. van der Have, B.Vastenhouw,A. J.A. van der Linden, P. P. van Rijk, J. P. H. Burbach, and M. P. Smidt, “U-SPECT-I: A novel system for submillimeter-resolution tomography with radiolabeled molecules in mice,” J. Nucl. Med., vol. 46, pp. 1194–1200, 2005.

[Bennink 2005] Bennink, R. J., J. Hamann, K. de Bruin, F. J. W. ten Kate, S. J. H. van Deventer, and A. a. te Velde (2005). Dedicated pinhole SPECT of intestinal neutrophil recruitment in a mouse model of dextran sulfate sodium-induced 165 colitis. Journal of nuclear medicine, Society of Nuclear Medicine, 46(3), pp. 526-531. ISSN 0161-5505.

[Bequé 2003] D. Bequé, J. Nuyts, G. Bormans, P. Suetens, and P. Dupont, “Characterization of pinhole SPECT acquisition geometry,” IEEE Trans. Med. Imag., vol. 22, pp. 599–612, May 2003.

[Bequé 2005] Bequé D, Nuyts J, Suetens P and Bormans G, 2005, Optimization of geometrical calibration in pinhole SPECT, IEEE Trans. Med. Imaging 24 180-90

[BK precision] B&K precision corporation, http://www.bkprecision.com/

[Bora 2015] V. Bora, H. Barrett, D. Fastje, E. Clarkson, L. Furenlid, A. Bousselham, K. Shah, and J. Glodo, “Estimation of fano factor in inorganic scintillators,” Nuclear Instruments & Methods in Physics Research, Section A: Accelerators, Spectrometers, Detectors, and Associated Equipment , 2015. Advance online publication. doi:10.1016/j.nima.2015.07.009.

[Bruining 1954] Bruining, H., “Physics and Applications of Secondary Emission” McGraw Hill, New York (1954).

[Bryant 1965] D. A. Bryant and A. D. Johnstone, Rev. Sci. Instrum. 36, 1662 (1965).

[Budinger 1974] T. F. Budinger and G. T. Gullberg, Three-dimensional reconstruction in nuclear medicine emission imaging, IEEE Trans. Nucl. Sci., vol. 21, no. 3, pp. 2-20, 1974.

[Bugby 2014] Bugby SL, Lees JE, Bhatia BS, Perkins AC. Characterization of a high resolution small field of view portable gamma camera. Physical Med 2014;30:331–9.

[Causer 1974] Causer D A 1974 Int. J. Appl. Radiat. Isot. 26 355

[Chaix 2015] Cécile Chaix, ADAPTISPECT: A PRECLINICAL IMAGING SYSTEM, Ph.D. thesis, University of Arizona, 2015.

[Chen 2005] Chen, Y-C.; Furenlid, L. R.; Wilson, DW.; Barrett, HH. Calibration of Scintillation Cameras and Pinhole SPECT Imaging Systems. In: Kupinski, MA.; Barrett, HH., editors. Small-Animal SPECT Imaging. Springer: New York: 2005. p. 195-201.

[Chen 2006] Y.C. Chen, System calibration and image reconstruction for a new small-animal SPECT system, Ph.D. thesis, University of Arizona, Department of Optical Sciences, Tucson, Arizona, 2006.

[Choong 2002] Choong WS, Gruber GJ, Moses WW, Derenzo SE, Holland SE, Pedrali-Noy M, Krieger B, Mandelli E, Meddeler G, Wang NW, Witt EK. A compact 16-module camera using 64-pixel CsI(Tl)/Si p-i-n photodiode imaging modules. Nuclear Science, IEEE Transactions on. 2002; 49:2228–35.

[Chung 2002] J.-K. Chung. "Sodium iodide symporter: its role in nuclear medicine," J. Nucl Med., vol. 43, pp. 1188-1200, 2002.

[Constantinesco 2005] Constantinesco, A., P. Choquet, L. Monassier, V. Israel-Jost, and L. Mertz (2005). Assessment of left ventricular perfusion, volumes, and motion in mice using pinhole gated SPECT. Journal of nuclear medicine, Society of Nuclear Medicine, 46(6), pp. 1005-1011. ISSN 0161-5505.

[Defrise 2008] Defrise M, Vanhove C and Nuyts J 2008 Perturbative refinement of the geometric calibration in pinhole SPECT IEEE Trans. Med. Imaging 27 204-14

[DiFilippo 2008] DiFilippo F P 2008 Geometric characterization of multi-axis multi-pinhole SPECT Med. Phys. 35 181-94 Univ. Arizona, Tucson, AZ, 2006.

[Denvir 2002] D.J. Denvir and E. Conroy, Electron multiplying CCD technology - The new ICCD, 4796 (2002), 164–174.

[Deutscher 2009] Deutscher, S. L., S. D. Figueroa, and S. R. Kumar (2009). Tumor targeting and SPECT imaging properties of an (111)In-labeled galectin-3 binding peptide in prostate carcinoma. Nuclear medicine and biology, 36(2), pp. 137-46. ISSN 0969-8051. doi:10.1016/j.nucmedbio.2008.10.015.

[Dorenbos 1995] P. Dorenbos, J. T. M. de Haas, C. W. E. van Eijk, "Nonproportinoality in Scintillator Response and Energy Resolution Obtainable with Scintillator Crystals," IEEE Trans Nucl Sci, vol. 42, pp. 2190-2202, 1995.

[Durko 2014] Durko, H. L. (2014). Anamorphic Preclinical SPECT Imaging with High-Resolution Silicon Double-Sided Strip Detectors. Ph.D. thesis, The University of Arizona.

[Eberhardt 1979] E.H. Eberhardt, Appl. Opt. 18 (1979) 1418.

[Felber 2002] Philip Felber, CHARGE-COUPLED DEVICES, http://www.ece.iit.edu/~pfelber/ccd/project.pdf

[Fernández 2004] Fernández M, Benlloch J, Cerdá J, Escat B, Giménez E, Giménez M, et al. A flat panel-based mini gamma camera for lymph nodes studies. Nucl Instrum Methods Phys Res Sect A 2004;527:92–6.

[Fiorini 2000] Fiorini C, Longoni A, Perotti F. New detectors for gamma-ray spectroscopy and imaging, based on scintillators coupled to silicon drift detectors. Nuclear Instruments and Methods in Physics Research Section A: Accelerators, Spectrometers, Detectors and Associated Equipment. 2000; 454:241–6.

[FLIR] FLIR Imaging Systems, https://www.ptgrey.com/

[Fujinon] Fujinon, Inc., http://www.fujinon.com/.

[Funk 2006] T. Funk, P. Després, W. C. Barber, K. S. Shah, and B. H. Hasegawa, "A multipinhole small animal SPECT system with submillimeter spatial resolution," Med Phys, vol. 33, no. 5, pp. 1259–1268, 2006.

[Furenlid 2004] Furenlid, L. R., D. W. Wilson, Y.-C. Chen, H. Kim, P. J. Pietraski, M. J. Crawford, and H. H. Barrett (2004). FastSPECT II: A Second-Generation High-Resolution Dynamic SPECT Imager. IEEE transactions on nuclear science, 51(3), pp. 631-635. ISSN 0018-9499. doi:10.1109/TNS.2004.830975.

[Furenlid 2005] L. R. Furenlid et al., "SPECT Imager Design and Data-Acquisition Systems", ch.2 in "Small Animal SPECT Imaging", M. A. Kupinski and H. H. Barrett, editors, Springer Science+ Business Media, 2005.

[Furman 2002] M. A. Furman and M. T. F. Pivi, Probabilistic model for the simulation of secondary electron emission. Phys. Rev. ST Accel. Beams 5, 124404 (2002).

[Gambini 2011] Gambini, J. P., P. Cabral, O. Alonso, E. Savio, S. D. Figueroa, X. Zhang, L. Ma, S. L. Deutscher, and T. P. Quinn (2011). Evaluation of 99mTc glucarate as a breast cancer imaging agent in a xenograft animal model. Nuclear medicine and biology, 38(2), pp. 255-260. ISSN 1872-9614 (Electronic). doi:10.1016/j.nucmedbio.2010.08.002.

[Genna 1988] Genna S, Smith AP. The Development of Aspect, an Annular Single-Crystal Brain Camera for High-Efficiency SPECT. Ieee T Nucl Sci. 1988; 35:654–8.

[Gerber 1974] Gerber MS, Miller DW: Parallel-hole collimator de sign. J Nucl Med 15:724-725,1974

[Golestani 2010] Golestani, R., C. Wu, R. a. Tio, C. J. Zeebregts, A. D. Petrov, F. J. Beekman, R. A. Dierckx, H. H. Boersma, and R. H. Slart (2010). Small-animal SPECT and SPECT/CT: application in cardiovascular research. European journal of nuclear medicine and molecular imaging, 37(9), pp. 1766-77. ISSN 1619-7089.

[Gullberg 1990] Gullberg GT, Tsui BMW, Crawford CR, Ballard JG, Hagius JT. Estimation of geometrical parameters and collimator evaluation for cone beam tomography. Med Phys 1990;17:264–272.

[Gunter 1996] D. L. Gunter, "Collimator characteristics and design," Nuclear Medicine eds R. E. Henkin, et al. St. Louis, MO, 1996.

[Hamamatsu] http://www.hamamatsu.com/resources/pdf/etd/FOS_ACS_GPXS_ALS_TXPR1024E.pdf

[Harris 1971] L.A. Harris, Rev. Sci. Instrum. 42 (1971) 987.

[Herbert 2006] Herbert DJ, Saveliev V, Belcari N, D'Ascenzo N, Del Guerra A, Golovin A. First results of scintillator readout with silicon photomultiplier. Nuclear Science, IEEE Transactions on. 2006; 53:389–94.

[Hevesy 1923] Hevesy, G. (1923). "The Absorption and Translocation of Lead by Plants: A Contribution to the Application of the Method of Radioactive Indicators in the Investigation of the Change of Substance in Plants". The Biochemical Journal. 17 (4–5): 439–445. PMC 1263906. PMID 16743235. doi:10.1042/bj0170439.

[Hevesy 1962] G. von Hevesy, Adventures in radioisotope research: The collected papers of George Hevesy. Adventures in Radioisotope Research, Pergamon Press, 1962.

[Hill 1976] G.E. Hill. Secondary electron emission and compositional studies on channel plate glass surfaces. Adv. Electron. Electron Phys. A 40 (1976) 153.

[Hsieh 1997] Y.-L. Hsieh, G. L. Zeng, and G. T. Gullberg, "Estimation of geometric parameters for cone beam geometry," in Int. Meeting Fully Three-Dimensional Image Reconstruction Radiol. Nucl. Medicine, 1997, pp. 150–153.

[Hynecek 2001] J. Hynecek, Impactron–a new solid state image intensifier, IEEE Transactions on Electron Devices 48 (2001), no. 10, 2238–2241.

[INCOM] INCOM UAS, Inc. http://www.incomusa.com/

[Jaszczak 1994] R. J. Jaszczak, J. Li, H. Wang, M. R. Zulutsky, R. E. Coleman "Pinhole collimation for ultra-high-resolution small-field-of-view SPECT," Phys Med Biol, vol. 39, pp. 425-437, 1994.

[Jerram 2001] Jerram, P.; Pool, PJ.; Bell, R.; Burt, DJ.; Bowring, S.; Spencer, S.; Hazelwood, M.; Moody, I.; Catlett, N.; Heyes, PS. The LLCCD: low-light imaging without the need for an intensifier. Blouke, MM., et al., editors. SPIE; San Jose, CA, USA: 2001. p. 178-86.

[Kapusta 2007] Kapusta, M.; Lavoute, P.; Lherbet, F.; Rossignol, E.; Moussant, C.; Fouche, F. Breakthrough in quantum efficiency of bi-alkali photocathodes PMTs. Nuclear Science Symposium Conference Record, 2007. NSS '07. IEEE; 2007. p. 73-7.

[Kastis 1998] Kastis, G., H. Barber, H. Barrett, H. Gi_ord, I. Pang, D. Patton, J. Sain, G. Stevenson, and D. Wilson (1998). High resolution SPECT imager for three dimensional imaging of small animals. Journal of Nuclear Medicine, 39(5), pp. 9-9.

[Kastis 2002] G. K. Kastis, "Multi-modality imaging of small animals," Ph.D. dissertation, Opt. Sci. Center, University of Arizona, Tucson, AZ, 2002.

[Kawata 1992] J. Kawata, K. Ohya, I. Mori, Jpn. J. Appl. Phys. 31 (1992) 1453.

[Kawata 1997] J. Kawata, K. Ohya, Jpn. J. Appl. Phys. 36(1997) 2325.

[Keller 1968] E. L. Keller, "Optimum dimensions of parallel-hole multi-aperture collimators for gamma-ray cameras", J. Nucl. Med., vol. 9, no. 6, pp. 233-235, 1968.

[Khaw 1997] B.-A. Khaw, A. Nakazawa, S.M. O'Donnell, K.-Y. Pak, and J. Narula. "Avidity of Technetium-99m glucarate for the necrotic myocardium: in vivo and in vitro assessment," J. Nucl. Cardiol., vol. 4, pp. 283-290, 1997.

[Kim 2006] H. Kim, L. R. Furenlid, M. J. Crawford, D. W. Wilson, H. B. Barber, T. E. Peterson, W. C. Hunter, Z. Liu, J. M. Woolfenden, and H. H. Barrett, SemiSPECT: a small-animal single-photon emission computed tomography (SPECT) imager based on eight cadmium zinc telluride (CZT) detector arrays, Med. Phys., vol. 33, p. 465, 2006.

[Klein 1995] W.P. Klein, H.H. Barrett, I.W. Pang, D.D. Patton, M.M. Rogulski, J.D. Sain, and W.E. Smith, FastSPECT: Electrical and mechanical design of a high-resolution dynamic SPECT imager, Nuclear Science Symposium and Medical Imaging Conference Record 2 (1995), 931-933.

[Knoll 1999] Knoll G. F. 1999, Radiation detection and measurement, Wiley Text Books, 3rd edn (New York: Wiley)

[Knoll 2014] Knoll P, Mirzaei S, Schwenkenbecher K, Barthel T. Performance evaluation of a solid-state detector based handheld gamma camera system. Front Biomed Technol 2014; 231–234.

[Korevaar 2009] Korevaar MA, Heemskerk JW, Beekman FJ. A pinhole gamma camera with optical depth-ofinteraction elimination. Physics in medicine and biology. 2009; 54:N267–N72.

[Kume 1986] Kume H, Muramatsu S, Iida M. Position Sensitive Photomultiplier Tubes for Scintillation Imaging. Nuclear Science, IEEE Transactions on. 1986; 33:359–363.

[Kyushima 2000] Kyushima, H.; Shimoi, H.; Atsumi, A.; Ito, M.; Oba, K.; Yoshizawa, Y. The development of flat panel PMT. Nuclear Science Symposium Conference Record, 2000 IEEE; 2000. p. 7/3-7.

[Levi 1982] Levi A, Roth M, Schieber M, Lavy S, Cooper G. The Development of Mercuric Iodide Gamma- Radiation Detectors for Application in Nuclear Medicine. Nuclear Science, IEEE Transactions on.1982; 29:457–60.

[Li 1993] Li J, Jaszczak RJ, Wang H, Greer KL, Coleman RE. Determination of both mechanical and electronic shifts in cone beam SPECT. Phys Med Biol 1993;38:743–754.

[Liu 2002] Liu Z, Kastis GA, Stevenson GD, et al. Quantitative analysis of acute myocardial infarct in rat hearts with ischemia-reperfusion using a high-resolution stationary SPECT system. J Nucl Med. 2002;43:933–939.

[Liu 2007] Liu, Z., M. Zhao, X. Zhu, L. R. Furenlid, Y.-C. Chen, and H. H. Barrett (2007). In vivo dynamic imaging of myocardial cell death using 99mTc-labeled C2A domain of synaptotagmin I in a rat model of ischemia and reperfusion. Nuclear medicine and biology, 34(8), pp. 907-15. ISSN 0969-8051. doi:10. 1016/j.nucmedbio.2007.07.013.

[Llopart 2002] Llopart X, Campbell M, Dinapoli R, San Segundo D, Pernigotti E. Medipix2: A 64-k pixel readout chip with 55-μm square elements working in single photon counting mode. Nuclear Science, IEEE Transactions on. 2002; 49:2279–83.

[Luke 2000] Luke PN, Amman M, Phlips BF, Johnson WN, Kroeger RA. Germanium orthogonal strip detectors with amorphous-semiconductor contacts. Ieee T Nucl Sci. 2000; 47:1360–3.

[Marks 1996] Marks DG, Barber HB, Barrett HH, Dereniak EL, Eskin JD, Matherson KJ, Woolfenden JM, Young ET, Augustine FL, Hamilton WJ, Venzon JE, Apotovsky BA, Doty FP. A 48 × 48 CdZnTe array with multiplexer readout. Nuclear Science, IEEE Transactions on. 1996; 43:1253–9.

[Mather 1957] MATHER, R. L., Gamma-ray collimator penetration and scattering effects. I. App. Phys. 28: 1,200, 1957.

[McMaster 1969] W. H. McMaster, N. Kerr Del Granve, J. H. Mallett, J. H. Hubell, Compilation of X-Ray Cross Sections, National Technical Information Service, Springfield, Va., 1969.

[Mediso] http://www.mediso.com/uploaded/product_features56.pdf

[Meng 2006] L.J. Meng, An intensified EMCCD camera for low energy gamma ray imaging applications, Nuclear Science, IEEE Transactions on 53 (2006), no. 4, 2376-2384.

[Metzler 2001] Metzler SD, Bowsher JE, Smith MF, Jaszczak RJ. Analytic determination of pinhole collimator sensitivity with penetration. IEEE Trans Med Imaging. 2001; 20:730–741

[Metzler 2005] Metzler SD, Greer KL, Jaszczak RJ. Determination of mechanical and electronic shifts for pinhole SPECT using a single point source. IEEE Trans Med Imaging 2005;24:361–370.

[Miller 2006] B.W. Miller, H.B. Barber, H.H. Barrett, D.W. Wilson, L. Chen, A low-cost approach to high-resolution, single-photon imaging using columnar scintillators and image intensifiers, in: Conference Record of 2006 IEEE Nuclear Science Symposium, vol. 6, 2006.

[Miller 2006a] B.W. Miller, H.B. Barber, H.H. Barrett, I. Shestakova, B. Singh, and V.V. Nagarkar, Single-photon spatial and energy resolution enhancement of a columnar CsI(Tl)/EMCCD gamma camera using maximum-likelihood estimation, Proc. Of SPIE 6142 (2006), 61421T-1.

[Miller 2007] B.W. Miller, H.B. Barber, H.H. Barrett, L. Chen, and S.J. Taylor, Photon-counting gamma camera based on columnar CsI(Tl) optically coupled to a back-illuminated CCD, Proc. of SPIE 6510 (2007), no. 1, 65100N.

[Miller 2008] Miller B, Barrett H, Furenlid L, Bradford Barber H, Hunter R. Recent advances in BazookaSPECT: Real-time data processing and the development of a gamma-ray microscope. Nuclear Inst and Methods in Physics Research, A 2008;591(1):272–275.

[Miller 2009] B. W. Miller, H. B. Barber, L. R. Furenlid, S. K. Moore, H. H. Barrett, F. P. Doty, H. B. Barber, H. Roehrig, R. C. Schirato, "Progress of BazookaSPECT", SPIE, vol. 7450, no. 1, pp. 74500C, 2009.

[Miller 2009a] Brian W. Miller, Jared W. Moore, Michael E. Gehm, Lars R. Furenlid, Harrison H. Barrett, "Novel applications of rapid prototyping in gamma-ray and X-ray imaging", Nuclear Science Symposium Conference Record (NSS/MIC) 2009 IEEE, pp. 3322-3326, 2009, ISSN 1095-7863.

[Miller 2010] Brian Miller, Lars Furenlid, Stephen Moore, H. Barber, Vivek Nagarkar and Harrison Barrett, FastSPECT III: A third-generation high-resolution dynamic SPECT imager, J Nucl Med, vol.51, no. supplement 2 83, 2010

[Miller 2012a] Miller BW, Barber HB, Barrett HH, Liu Z, Nagarkar VV, Furenlid LR. Progress in BazookaSPECT: high-resolution dynamic scintigraphy with large-area imagers. Proc SPIE. 2012;8508 85080F.

[Miller 2012b] Miller, B. W. (2012). High-resolution gamma-ray imaging with columnar scintillators and CCD/CMOS sensors, and FastSPECT III: A third-generation stationary SPECT imager. Ph.D. thesis, University of Arizona.

[Miller 2012c] Miller BW, Van Holen R, Barrett H, Furenlid L. A system calibration and fast iterative reconstruction method for next-generation SPECT imagers. IEEE Trans Nucl Sci. 2012; 59:1990–6.

[Miller 2014] Brian W.Miller, Stephanie J. Gregory, Erin S. Fuller, Harrison H. Barrett, H. Bradford Barber, Lars R. Furenlid, The iQID camera: An ionizing-radiation quantum imaging detector. Nuclear Instruments and Methods in Physics Research A 767 (2014) 146–152

[Miller 2015] Brian W. Miller, Sofia H. L. Frost, Shani L. Frayo, Aimee L. Kenoyer, Erlinda Santos, Jon C. Jones, Damian J. Green, Donald K. Hamlin and D. Scott Wilbur, Darrell R. Fisher, Johnnie J. Orozco, Oliver W. Press, John M. Pagel, and Brenda M. Sandmaier, "Quantitative single-particle digital autoradiography with a-particle emitters for targeted radionuclide therapy using the iQID camera", Med.Phys. 42 (7), 2015.

[Milster 1984] Milster TD, Selberg LA, Barrett HH, Easton RL, Rossi GR, Arendt J, Simpson RG. A modular scintillation camera for use in nuclear medicine. IEEE Trans. Nucl. Sci. 1984 Feb.NS-31(1):578–580.

[Milster 1990] Milster TD, Aarsvold JN, Barrett HH, Landesman AL, Mar LS, Patton DD, Roney TJ, Rowe RK, Seacat RH., III A full-field modular gamma camera. J. NucI. Med. 1990;31:632–639.

[Moslehi 2015] Moslehi M, Shanei A, Hakimian SM, et al., 2015. (99m)Tc-Phytate Lymphoscintigraphy for detection of sentinel node: preliminary results of the first year's clinical experience in Isfahan, Iran. J Med Signals Sens 5:69-74.

[Muehllehner 1985] G. Muehllehner, "Effect of resolution improvement on required count density in ECT imaging: a computer simulation," Phys Med Biol, vol. 30, no. 2, pp. 163-173, 1985.

[Mueller 1986] Mueller SP, Pollak JF, Kijewski MF, Holman BL (1986) Collimator selection for SPECT brain imaging: the advantage of high resolution. J Nucl Med 27:1729–1738

[Munn 2014] Munn LL, Padera TP. Imaging the lymphatic system. Microvasc Res2014; 96:55-63.

[Murtaza 2014] G. Murtaza, K. Gao, T. Liu, I. Tariq, A. Sajjad, M. R. Akram, M. Niu, G. Liu, Z. Mehmood and G. Tian, BioMed Res. Int., 2014, 714674

[Myers 1979] Myers, W. G. (1979). "Georg Charles de Hevesy: The father of nuclear medicine". Journal of nuclear medicine : official publication, Society of Nuclear Medicine. 20 (6): 590–594. PMID 395289.

[Müller 1986] S. P. Müller, J. F. Polak, M. F. Kijewski, B. L. Holman, "Collimator Selection for SPECT Brain Imaging: The Advantage of High Resolution," J. Nucl Med, vol. 27, pp. 1729-1738, 1986.

[Müller 2013] C. Müller and R. Schibli, Single photon emission computed tomography tracer, in Molecular Imaging in Oncology, pp. 65_105, Springer, 2013.

[Nagarkar 1995] V.V. Nagarkar, J. Gordon, S. Vasile, M. Squillante, and G. Entine, "Improved X-ray converters for CCD crystallographic detectors," Proc. SPIE, vol. 2519, 1995

[Nagarkar 1997] V.V. Nagarkar, T.K. Gupta, S.R. Miller, Y. Klugerman, M.R. Squillante, Structured CsI(Tl) Scintillators for X-ray Imaging Applications. IEEE Trans. Nucl. Sci, 45, pp. 492-496, (1997)

[Nagarkar 1998] Nagarkar VV, Gupta TK, Miller SR, Klugerman Y, Squillante MR, Entine G. Structured CsI(Tl) scintillators for X-ray imaging applications. Nuclear Science, IEEE Transactions on. 1998; 45:492–6.

[Nagarkar 2005] Vivek V. Nagarkar, Sameer V. Tipnis, "PIXELLATED MICRO-COLUMNAR FILMS SCINTILLATOR", Patent No.: US 6,921,909 B2, 2005

[Nagarkar 2007] V.V. Nagarkar, I. Shestakova, V. Gaysinskiy, B. Singh, B.W. Miller, and H.B. Barber, Fast X-ray/γ-ray imaging using electron multiplying CCD-based detector, Nuclear Inst. and Methods in Physics Research, A 563 (2007), no. 1F, 45-48.

[Niikura 2005] Niikura H, Okamura C, Utsunomiya H, et al. Sentinel lymph node detection in patients with endometrial cancer. Gynecol Oncol 2005; 92:669–674.

[Olcott 2014] Olcott P, Pratx G, Johnson D, Mittra E, Niederkohr R, Levin CS. Clinical evaluation of a novel intraoperative handheld gamma camera for sentinel lymph node biopsy. Physica Med 2014;30:340–5.

[Ozmen 2006] Ozmen MM, Zulfikaroglu B, Kucuk NO, Ozalp N, Aras G, Koseoglu T, et al. Lymphoscintigraphy in detection of the regional lymph node involvement in gastric cancer. Ann R Coll Surg Engl 2006;88:632–638.

[Park 2012] Ryeojin Park, et al. "A Prototype Detector for a Novel High-Resolution PET System: BazookaPET", IEEE/NSSMIC, 2012

[Park 2014] Ryeojin Park, "Novel applications using maximum-likelihood estimation in optical metrology and nuclear medical imaging: Point-diffraction interferometry and BazookaPET", PhD dissertation, University of Arizona, 2014

[Peli 1990] PELI, E. 1990. Contrast in complex images. J. Opt. Soc. Am. A 7, 10 (October), 2032-2040.

[Peterson 2003] Peterson TE, Wilson DW, Barrett HH. Application of silicon strip detectors to small-animal imaging. Nucl Instrum Meth A. 2003; 505:608–11.

[Peterson 2011] T. Peterson and L. Furenlid, SPECT detectors: the Anger camera and beyond, Phys. Med. Biol., vol. 56, p. R145, 2011.

[Petrovna 1988] I.R. Petrovna, Yu.A. Flegontov, Sov. J. Opt. Tech. 55 (1988) 210.

[Pettersen 2005] Pettersen DM, Mikkelsen S, Talebi J, Meier D. A readout ASIC for SPECT. Nuclear Science, IEEE Transactions on. 2005; 52:764–71.

[Photron] Photron, Inc., http://www.photron.com/.

[Price 2001] G. J. Price and G. W. Fraser, Calculation of the output charge cloud from a microchannel plate. Nucl. Instrum. Methods Phys. Res. A 474, 188 (2001).

[ProxiVision] http://www.proxivision.de/datasheets/image-intensifier-general information.pdf

[RMD] Radiation Monitoring Devices, Inc. http://rmdinc.com/

[Rizo 1994] Ph. Rizo, P. Grangeat, and R. Guillemaud, "Geometric calibration method for multiple-head cone-beam SPECT system," IEEE Trans. Nucl. Sci., vol. 41, pp. 2748–2757, July 1994.

[Robbins 2003] M.S. Robbins and B.J. Hadwen, The noise performance of electron multiplying charge-coupled devices, IEEE Transactions on Electron Devices 50 (2003), no. 5, 1227–1232.

[Rogulski 1993] M.M. Rogulski, H.B. Barber, H.H. Barrett, R.L. Shoemaker, and J.M. Woolfenden, Ultra-high-resolution brain SPECT imaging: simulation results, Nuclear Science, IEEE Transactions on 40 (1993), no. 4, 1123-1129.

[Rolland 1990] J. P. Rolland, Factors influencing lesion detection in medical imaging, Ph.D. Dissertation, University of Arizona, Tucson, Arizona, 1990.

[Rolland 1992]J. P. Rolland, H. H. Barrett, "Effect of random background inhomogeneity on observer detection performance," J. Opt Soc Am A, vol. 9, no. 5, pp. 649-658, 1992

[Rowe 1993] R.K. Rowe, J.N. Aarsvold, H.H. Barrett, J. Chen, W.P. Klein, B.A. Moore, I.W. Pang, D.D. Patton, and T.A. White, A stationary hemispherical SPECT imager for three-dimensional brain imaging, J Nucl Med 34 (1993), no. 3, 474-480.

[RTM] The Rapid Tool Maker System (RTM), http://www.a3dm.com

[Röntgen 1895] Wilhelm Röntgen, "Ueber eine neue Art von Strahlen. Vorläufige Mitteilung", in: Aus den Sitzungsberichten der Würzburger Physik.-medic. Gesellschaft Würzburg, pp. 137–147, 1895

[Röntgen 1896] Wilhelm Röntgen, "Eine neue Art von Strahlen. 2. Mitteilung", in: Aus den Sitzungsberichten der Würzburger Physik.-medic. Gesellschaft Würzburg, pp. 11–17, 1896;

[Röntgen 1897] Wilhelm Röntgen, "Weitere Beobachtungen über die Eigenschaften der X-Strahlen", in: Mathematische und Naturwissenschaftliche Mitteilungen aus den Sitzungsberichten der Königlich Preußischen Akademie der Wissenschaften zu Berlin, pp. 392–406, 1897

[Salow 1940] Salow, H., 2. Tech. Physik 21, 8 (1940).

[Sánchez 2004] Sanchez F, Benlloch J, Escat B, Pavón N, Porras E, Kadi-Hanifi D, et al. Design and tests of a portable mini gamma camera. Med Phys 2004;31:1384–97.

[Schmidt 1966] K. C. Schmidt and C. F. Hendee, IEEE Trans. Nuc!. Sci. NS-13, No.3, 100 (1966).

[Scholtz 1996] J. J. Scholtz, D. Dijkkamp, and R. W. A. Schmitz, Philips J. Res. 50, 375 (1996).

[Schramm 2003] N. U. Schramm, G. Ebel, U. Engeland, T. Schurrat, M. Behr, and T. M. Behr, "High-resolution SPECT using multipinhole collimation," IEEE Trans. Nucl. Sci., vol. 50, no. 3, pp. 315–320, 2003.

[PMT] SENSE, https://www.sense-pro.org/lll-sensors/pmt

[Seo 2011] Seo Y, et al. Mapping of lymphatic drainage from the prostate using filtered 99mTc-sulfur nanocolloid and SPECT/CT. J Nucl Med. 2011;52:1068–1072.

[Sevick-Muraca 2014] Sevick-Muraca EM, et al. Emerging lymphatic imaging technologies for mouse and man. J. Clin. Invest. 2014;124:905–914.

[Shah 2001] Shah KS, Farrell R, Grazioso R, Myers R, Cirignano L. Large-area APDs and monolithic APD arrays. Nuclear Science, IEEE Transactions on. 2001; 48:2352–6.

[Shah 2002] Shah KS, Farrell R, Grazioso R, Harmon ES, Karplus E. Position-sensitive avalanche photodiodes for gamma-ray imaging. Nuclear Science, IEEE Transactions on. 2002; 49:1687–92.

[Shepp 1982] L. A. Shepp and Y. Vardi, Maximum likelihood reconstruction for emission tomography, IEEE Trans. Med. Imag., vol. 1, no. 2, pp. 113122, 1982.

[Simmons 1988] Simmons GH: On-line correction for factors that affect uniformity and linearity, in Simmons GH: The scintillation camera. New York, NY, Society of Nuclear Medicine, 1988, pp 46-59

[Smith 2003] M. F. Smith, S. Majewski, A. G. Weisenberger, "Optimizing pinhole and parallel hole collimation for scintimammography with compact pixellated detectors", IEEE Trans. Nucl. Sci., vol. 50, pp. 321-326, June 2003.

[Sorenson 1987] Sorenson, J. A., Phelps, M. E. Physics in Nuclear Medicine; Grune & Stratton: Orlando, 1987.

[Stratasys] Stratasys, http://www.stratasys.com/3d-printers/objet-350-500-connex3

[Subramanian 1975] Subramanian G, McAfee JG, Blair RJ, Kallfelz FA, Thomas FD. Tc-99m methylene diphosphonate: a superior agent for skeletal imaging: comparison with other technetium corn- plexes. J Nucl Med 1975; 1

[Suzuki 2000] K. Suzuki, I. Horiba, and N. Sugie, Fast connected-component labeling based on sequential local operations in the course of forward raster scan followed by backward raster scan, Pattern Recognition, 2000. Proceedings. 15th International Conference on 2 (2000), 434-437.

[Taylor 2004] S.J. Taylor, Dual modality imaging with a lens-coupled CCD camera, Master's thesis, University of Arizona, Department of Optical Sciences, Tucson, Arizona, 2004.

[Tecomet] Tecomet, Inc. https://www.tecomet.com/chemical-etching.html

[Teo 2005] B.K. Teo, I. Shestakova, M. Sun, W.C. Barber, B.H. Hasegawa, and V.V. Nagarkar, Evaluation of an EMCCD detector for emission-transmission computed tomography, Nuclear Science Symposium Conference Record, 2005 IEEE 5 (2005), 3050-3054.

[Tornai 2001] Tornai MP, Archer CN, Weisenberger AG, Wojcik R, Popov V, Majewski S, Keppel CE, Levin CS, Tipnis SV, Nagarkar VV. Investigation of microcolumnar scintillators on an optical fiber coupled compact imaging system. Nuclear Science, IEEE Transactions on. 2001; 48:637–44.

[Trotta 2007] Trotta C, Massari R, Palermo N, Scopinaro F, Soluri A. New high spatial resolution portable camera in medical imaging. Nucl Instrum Methods Phys Res Sect A 2007;577:604–10

[Truman 1994] Truman A, Bird AJ, Ramsden D, He Z. Pixellated CsI(T1) arrays with position-sensitive PMT readout. Nuclear Instruments and Methods in Physics Research Section A: Accelerators, Spectrometers, Detectors and Associated Equipment. 1994; 353:375–8.

[Valentine 1998] J. D. Valentine, B. D. Rooney, J. Li, "The light yield nonproportionality component of the scintillator energy resolution", IEEE Trans. Nucl. Sci., vol. 45, pp. 512-517, June 1998.

[van der Have 2008] van der Have F, Vastenhouw B, Rentmeester M, Beekman FJ. System calibration and statistical image reconstruction for ultra-high resolution stationary pinhole SPECT. IEEE Trans Med Imaging. 2008;27:960–71.

[Van der Have 2009] Van der Have, F., B. Vastenhouw, R. M. Ramakers, W. Branderhorst, J. O. Krah, C. Ji, S. G. Staelens, and F. J. Beekman (2009). U-SPECT-II: An Ultra-High-Resolution Device for Molecular Small-Animal Imaging. Journal of nuclear medicine : o_cial publication, Society of Nuclear Medicine, 50, pp. 599-605. ISSN 0161-5505. doi:10.2967/jnumed.108.056606.

[VANDERWILT] VANDERWILT techniques, Boxtel, The Netherlands, “VANDERWILT Techniques” [Online]. Available: http://www.for-med.nl

[Wang 2011] Wang, Y., S. Luo, J. Lin, L. Qiu, W. Cheng, H. Zhai, B. Nan, W. Ye, and Y. Xia (2011). Animal studies of 99mTc-i-PIDP: A new bone imaging agent. Applied Radiation and Isotopes, 69(9), pp. 1169-1175. ISSN 09698043. doi: 10.1016/j.apradiso.2011.03.045.

[Wei 2015] Wei, L. et al. 99mTc-dextran lymphoscintigraphy can detect sentinel lymph node in breast cancer patients. Exp Ther Med 9, 112–116 (2015).

[Weinmann 2009] Amanda L. Weinmann, Carrie B. Hruska,a and Michael K. O'Connor, Design of optimal collimation for dedicated molecular breast imaging systems.

[Weisenberger 1998] Weisenberger AG, Kross B, Majewski S, Wojlck R, Bradley EL, Saha MS. Design features and performance of a CsI(Na) array based gamma camera for small animal gene research. Nuclear Science, IEEE Transactions on. 1998; 45:3053–8.

[Weisenberger 2001] Weisenberger, AG.; Majewski, S.; Popov, V.; Wojcik, R. High resolution detector modules based on NaI(Tl) arrays for small animal imaging. Nuclear Science Symposium Conference Record, 2001 IEEE; 2001. p. 1540-4.

[Wernick 2004] Wernick, M. N. and J. N. Aarsvold (2004). Emission tomography: the funda- mentals of PET and SPECT. Academic Press.

[Widen 2008] Marketing Widen. http://www.widen.com/premediablog/call-me-mr-biv-v1. 2008

[WIKIPEDIA Rutherford] https://en.wikipedia.org/wiki/Ernest_Rutherford

[WIKIPEDIA Image Intensifier] https://en.wikipedia.org/wiki/Image_intensifier

[Wiza 1979] Joseph Ladislas Wiza, Microchannel Plate Detectors, Nucl. Inst. Meth, Vol. 162, 1979, pages 587-601.

[Wu 2008] Ming Wu, Craig A. Kruschwitz, Dane V. Morgan, and Jiaming Morgan, Monte Carlo simulations of microchannel plate detectors. I. Steady-state voltage bias results. Rev. Sci. Instrum. 79, 073104 (2008).

[Young 1986] B. F. K. Young, R. E. Stewart, J. G. Woodworth, and J. Bailey, Rev. Sci. Instrum. 57, 2729 (1986).

[Yuan 2006] Yuan Z, Chen L, Zhu J, Lu H, Zhu R (2006) The role of radionuclide lymphoscintigraphy in extremity lymphedema. Ann Nucl Med 20(5):341–344

[Zhao 2009] ZHAO Xiaochuan, LUO Qingsheng, HAN Baoling, LI Xiyu, Image Distortion Correction Algorithm Based on Quadrilateral Fractal Approach Controlling Points; Opto-Electronic Engineering; 2009-05

[Zinn 2002] K.R. Zinn and T.R. Chaudhuri. "The type 2 human somatostatin receptor as a platform for reporter gene imaging," Eur. J. Nucl. Med., vol. 29, pp. 388-399, 2002.